UNIVERSITY OF CALIFORNIA

Santa Barbara

Heterogeneous Silicon/III-V Photonic Integration for Ultralow Noise Semiconductor Lasers

A dissertation submitted in partial satisfaction of the
requirements for the degree Doctor of Philosophy
in Electrical and Computer Engineering

by

Minh Anh Tran

Committee in charge:

Professor John E. Bowers, Chair

Professor Larry A. Coldren

Professor Daniel J. Blumenthal

Professor Jon A. Schuller

March 2019

The dissertation of Minh Anh Tran is approved.

_____

Professor Larry A. Coldren

_____

Professor Daniel J. Blumenthal

_____

Professor Jon A. Schuller

_____

Professor John E. Bowers, Committee Chair

March 2019

Heterogeneous Silicon/III-V Photonic Integration for

Ultralow Noise Semiconductor Lasers

by

Minh Anh Tran

To my beloved family

ACKNOWLEDGEMENTS

My PhD was a great journey.
To everyone who was a part of it, thank you very much.

CURRICULUM VITAE

Minh Anh Tran
March 2019

EDUCATION

3/2019	Ph.D. in Electrical Engineering and Computer Engineering, University of California, Santa Barbara
6/2015	M.S. in Electrical Engineering and Computer Engineering, University of California, Santa Barbara
3/2013	B.S., Department of Electrical Engineering and Information Systems, the University of Tokyo, Japan

PROFESSIONAL EMPLOYMENT

1/2019 –	Senior Engineer, Nexus Photonics LLC, Santa Barbara, CA
4/2014 – 12/2018	Graduate Student Researcher, Department of Electrical Engineering and Computer Engineering, University of California, Santa Barbara, CA
9/2013 – 3/2014	Teaching Assistant, Department of Electrical Engineering and Computer Engineering, University of California, Santa Barbara, CA

HONORS AND AWARDS

10/2015	Best Student Paper Award Finalist, IEEE Photonics Conference (IPC)
2013 – 2014	Holbrook Foundation Fellowship, Institute of Energy Efficiency
2013 – 2015	Vietnam Education Foundation (VEF) Fellowship
7/2013	Excellent Student Research Award, Asia Pacific Near-Field Optics Conference, Singapore
3/2013	Best Thesis Award, the University of Tokyo
2008 – 2013	Japanese Government MEXT Scholarship for International Students

PUBLICATIONS

Book Chapters

1. M. L. Davenport, **M. A. Tran**, T. Komljenovic, and J. E. Bowers, "Heterogeneous Integration of III–V Lasers on Si by Bonding," *Semiconductors and Semimetals*, vol. 99, pp. 139–188, Jan. 2018.

Journal Articles

1. **M. Tran**, D. Huang, T. Komljenovic, J. Peters, A. Malik, and J. Bowers, "Ultra-Low-Loss Silicon Waveguides for Heterogeneously Integrated Silicon/III-V Photonics," *Applied Science*., vol. 8, no. 7, p. 1139, 2018 **(Invited).**

2. **M. A. Tran**, T. Komljenovic, J. C. Hulme, M. Kennedy, D. J. Blumenthal, and J. E. Bowers, "Integrated optical driver for interferometric optical gyroscopes," *Optics Express*, vol. 4, no. 4, pp. 3826–3840, 2017.

3. **M. Tran**, T. Komljenovic, J. Hulme, M. Davenport, and J. Bowers, "A Robust Method for Characterization of Optical Waveguides and Couplers," *IEEE Photonics Technology Letters*., vol. PP, no. 99, pp. 1–1, 2016.

4. **M. A. Tran**, T. Kawazoe, and M. Ohtsu, "Fabrication of a bulk silicon p-n homojunction-structured light-emitting diode showing visible electroluminescence at room temperature," *Applied Physics A: Material Science and Processing*, 2014.

5. W. Xie, T. Komljenovic, J. Huang, **M. Tran**, M. Davenport, A. Torres, P. Pintus, and J. Bowers, "Heterogeneous silicon photonics sensing for autonomous cars," *Optics Express,* 2019.

6. Q. Yang, B. Shen, H. Wang, **M. Tran**, Z. Zhang, K. Y. Yang, L. Wu, C. Bao, J. Bowers, A. Yariv, and K. Vahala, "Vernier spectrometer using counterpropagating soliton microcombs.," *Science*, vol. 363, no. 6430, pp. 965–968, Mar. 2019.

7. T. Komljenovic, D. Huang, P. Pintus, **M. A. Tran**, M. L. Davenport, and J. E. Bowers, "Photonic Integrated Circuits Using Heterogeneous Integration on Silicon," *Proceedings of the IEEE*. 2018.

8. S. Gundavarapu, M. Belt, T. Huffman, **M. A. Tran**, T. Komljenovic, J. E. Bowers, and D. J. Blumenthal, "Interferometric Optical Gyroscope Based on an Integrated Si3N4 Low-Loss Waveguide Coil," *Journal of Lightwave Technology*, 2018.

9. C. Xiang, **M. A. Tran**, T. Komljenovic, J.C. Hulme, M.L. Davenport, D.M. Baney, B. Szafraniec, and J. E. Bowers, "Integrated chip-scale Si_3N_4 wavemeter with narrow free spectral range and high stability," *Optics Letters*., 2016.

10. T. Komljenovic, **M. A. Tran**, M. Belt, S. Gundavarapu, D. J. Blumenthal, and J. E. Bowers, "Frequency modulated lasers for interferometric optical gyroscopes," *Optics Letters*., vol. 41, no. 8, p. 1773, 2016.

11. N. Wada, **M. A. Tran**, T. Kawazoe, and M. Ohtsu, "Measurement of multimode coherent phonons in nanometric spaces in a homojunction-structured silicon light emitting diode," *Applied Physics A: Material Science and Processing*, 2014.

Conference Papers

1. **M. A. Tran**, D. Huang, J. Guo, J. Peters, T. Komljenovic, P. A Morton, J. B. Khurgin, C. C. Morton, J. E. Bowers, "Ultra-low Noise Widely-Tunable Semiconductor Lasers Fully Integrated on Silicon", Compound Semiconductor Week, Nara, Japan 2019 **(Invited)**.

2. **M. A. Tran**, D. Huang, T. Komljenovic, S. Liu, L. Liang, M. Kennedy, J. E. Bowers "Multi-Ring Mirror-Based Narrow-Linewidth Widely-Tunable Lasers in Heterogeneous Silicon Photonics," in 2018 *European Conference on Optical Communication (ECOC)*, 2018, pp. 1–3 **(Invited)**.

3. **M. A. Tran**, D. Huang, T. Komljenovic, J. Peters, and J.E. Bowers, "A 2.5 kHz Linewidth Widely Tunable Laser with Booster SOA Integrated on Silicon," in 2018 *IEEE International Semiconductor Laser Conference (ISLC),* 2018, pp. 1–2.

4. **M. A. Tran**, T. Komljenovic, D. Huang, L. Liang, M. Kennedy, and J. E. Bowers, "A Widely-Tunable High-SMSR Narrow-Linewidth Laser Heterogeneously Integrated on Silicon," in *Conference on Lasers and Electro-Optics*, 2018, p. AF1Q.2.

5. **M. A. Tran**, J. C. Hulme, T. Komljenovic, M. J. Kennedy, D. J. Blumenthal, and J. E. Bowers, "The first integrated optical driver chip for fiber optic gyroscopes," in 4th *IEEE International Symposium on Inertial Sensors and Systems*, INERTIAL 2017 - Proceedings, 2017.

6. **M. A. Tran,** C. Zhang, and J.E. Bowers, "A broadband optical switch based on adiabatic couplers," in *2016 IEEE Photonics Conference (IPC),* 2016, pp. 755–756.

7. **M. Tran**, J. Hulme, S. Srinivasan, J. Peters, and J. Bowers, "Demonstration of a tunable broadband coupler," in *2015 IEEE Photonics Conference (IPC),* 2015, pp. 488–489, 2015.

8. S. Liu, X. Wu, **M. Tran**, D. Huang, J. Norman, D. Jung, A. Gossard, J. Bowers, "High performance lasers on Si", OECC/PSC, Japan 2019 **(Invited)**

9. D. Huang, **M. A. Tran**, J. Guo, J. Peters, T. Komljenovic, A. Malik, P.A. Morton, and J. E. Bowers, "Sub-kHz linewidth Extended-DBR lasers heterogeneously integrated on silicon," in *Optical Fiber Communication Conference (OFC*) 2019, 2019, p. W4E.4.

10. J. E. Bowers, D. Huang, D. Jung, J. Norman, **M.A. Tran**, Y. Wan, W. Xie, Z. Zhang, "Realities and challenges of III-V/Si integration technologies," in *Optical Fiber Communication Conference (OFC)* 2019, 2019, p. Tu3E.1.

11. J. Ohania, A.A. Yakusheva, S.T. Kreger, D. Kominsky, B.J. Soller, **M. A. Tran**, T. Komljenovic, and J. E. Bowers., "OFDR on Photonic Circuits: Fiber Optic Sensing Infrastructure and Applications," in 26th *International Conference on Optical Fiber Sensors*, 2018, p. WB1.

12. M. Krainak, M. Stephen, E. Troupaki, S. Tedder, B. Reyna, J. Klamkin, H. Zhao, B. Song, J. Fridlander, **M. Tran**, J. E. Bowers, K Bergman, M. Lipson, A. Rizzo, I. Datta, N. Abrams, S. Mookherjea, S-T. Ho, Q. Bei, Y. Huang, Y. Tu, B. Moslehi, J. Harris, A. Matsko, A. Savchenkov, G. Liu, R. Proietti, SJB Yoo, L. Johansson, C. Dorrer, F.R Arteaga-Sierra, J. Qiao, S. Gong, T. Gu, O. J. Ohanian, X. Ni, Y. Ding, Y. Duan, H. Dalir, R. T Chen, V. J Sorger, T. Komljenovic, "Integrated photonics for NASA applications," Proceedings Volume 10899, Components and Packaging for Laser Systems V; 108990F, 2019.

13. S. Gundavarapu, T. Komljenovic, **M. A. Tran**, M. Belt, J. E. Bowers, and D. J. Blumenthal, "Effect of direct PRBS modulation on laser driven fiber optic gyroscope," in 4th *IEEE International Symposium on Inertial Sensors and Systems*, INERTIAL 2017 - Proceedings, 2017.

14. S. Gundavarapu, M. Belt, T. Huffman, **M. A. Tran**, T. Komljenovic, J. E. Bowers, and D. J. Blumenthal., "Integrated Sagnac optical gyroscope sensor using ultra-low loss high aspect ratio silicon nitride waveguide coil," 25th *International Conference on Optical Fiber Sensors* 2017, p. 103231A.

15. C. Xiang, **M. A. Tran**, T. Komljenovic, J.C. Hulme, M.L. Davenport, D.M. Baney, B. Szafraniec, and J. E. Bowers, "Integrated Chip-scale Wavemeter with 300 MHz Free Spectral Range," in *Conference on Lasers and Electro-Optics*, 2016, p. SM3G.3.

16. Y. Shen, **M. Tran**, S. Srinivasan, J. Hulme, J. Peters, M. Belt, S. Gundavarapu, Y. Li, D. Blumenthal, and J. Bowers., "Frequency modulated laser optical gyroscope," in *2015 IEEE Photonics Conference (IPC)*, 2015, pp. 431–432

ABSTRACT

Heterogeneous Silicon/III-V Photonic Integration for Ultralow Noise Semiconductor Lasers

by

Minh Anh Tran

Low noise lasers, with spectral linewidth of kHz level and below, are in demand by an increasing number of applications, such as coherent communications, LIDAR, and optical sensing. Such low noise is currently available only in solid-state lasers, fiber-based lasers, and external cavity lasers. These lasers are typically bulky, expensive and not scalable for mass production. Semiconductor diode lasers, although attractive for their low form factor, mass producibility and compatibility to integrated circuits, are notorious for their low coherence with typical linewidths over several MHz.

Heterogeneous silicon/III-V photonics integration opens a path to understand and develop low noise semiconductor lasers. By incorporating low loss high-Q silicon waveguide resonators as integral/extended parts of the Si/III-V laser cavity, we have demonstrated that it is possible to reduce the quantum noise in semiconductor lasers.

In this thesis, we discuss our attempt and success in pushing the noise level of the heterogeneously integrated Si/III-V lasers to record low levels using ring resonator coupled cavity lasers. The first generation of our lasers achieved Lorentzian linewidth in the kHz level. The second-generation lasers, with a new waveguide architecture for ultralow loss and novel cavity designs on silicon, have reached down to ultralow spectral linewidth of 100s-Hz level. Some of the fabricated lasers also possess an ultrawide wavelength tuning range of 120 nm across three optical communication bands (S+C+L). This unprecedented performance shows the potential for heterogeneous silicon photonics to reshape the future of semiconductor lasers.

TABLE OF CONTENTS

LIST OF FIGURES

LIST OF TABLES

Chapter 1. Introduction

1.1 Ultralow noise semiconductor lasers

Ultralow noise (ULN) semiconductor lasers are required for a wide range of applications, including high performance coherent communications systems [1], ultra-precise timing [2], frequency synthesis [3], spectroscopy [4], and distributed sensing systems [5]. Furthermore, there is significant demand for ULN lasers in RF photonic analog links and processing [6]–[8], as well as optically processed phase array antennas. ULN is a key requirement to any system involving optical mixing, as the noise of the laser will directly affect the fidelity of the generated RF signals. For example, two ULN lasers can be beat together in a high-speed photodetector to generate a stable microwave signal [9], [10]. Another major use of ULN lasers requiring extremely low phase noise is in the fiber optic sensing field, such as interferometric acoustic sensing systems for exploration or sonar sensing systems or distributed sensing systems. Finally, yet another fast-growing sensing application is LiDAR, where the low frequency phase noise again directly impacts system performance. The common requirements for all these applications are very low relative intensity noise (RIN) as well as very low frequency noise and Lorentzian linewidth. Current commercial solid state lasers [11], [12] and fiber lasers [13], [14] have high performance, but cannot compete with semiconductor lasers in terms of size, weight, and power (SWaP), or cost.

Recently, there has been significant interest in assembling semiconductor gain chips with long external cavities to reduce the laser linewidth. This hybrid approach is attractive because it allows for the gain chip and external cavity to be separately optimized. This starts with the material selection, and external cavities based on planar lightwave circuits (PLC) [15], low-loss silicon nitride [16], [17], and silicon [18], [19] have been demonstrated. The drawback

regarding these assembled hybrid semiconductor lasers is their limited scalability, as each laser must be individually assembled. Alignment between the chips is critical, which slows down the process and increases cost. Furthermore, many of the aforementioned sensing applications require that the devices are resistant to variations in pressure, shock, and vibration. This is another reason why a fully integrated solution is preferred over hybrid solutions, as the coupling between the gain chip and external cavity is sensitive to these environmental factors.

The heterogeneous silicon/III-V integration platform provides an excellent solution to this problem [20], [21]. Heterogeneous integration involves the wafer bonding of unprocessed materials on a wafer level scale, providing a clear path towards scaling and high-volume production. It benefits from mature CMOS-based silicon processing technologies and foundries. Heterogeneous integration also has the benefit of selecting the best material to perform each function (i.e. lasers, low-loss waveguides, detectors) to form highly complex photonic integrated circuits (PIC) [22]. Thus, it provides much more flexibility compared to a purely monolithic approach, while retaining the much-needed scalability that hybrid solutions lack.

Figure 1.1, replotted from [23], reflects the trend in semiconductor laser noise in the past decades. Although being only focused on widely tunable lasers, it does provide readers with the research process on semiconductor laser noise in general. Here, the authors compared the spectral linewidth of widely-tunable lasers on the three main categories: *III/V based monolithic lasers, hybrid lasers* where III/V gain chips are butt coupled to passive chips, and *heterogeneous integrated lasers* where the III/V gain material is bonded to silicon. It can be clearly observed that the III-V conventional monolithic lasers, mostly SGDBR types, have the

linewidth reduced with time but the best results are still around ~70s of kHz. The hybrid lasers with multiple chips assembled show far more superior linewidth performances, down to ~300 Hz level, thanks to the low loss external cavity on a separated chip. The heterogeneous Si/III-V lasers have made good progress in the past 5 years, and the lowest reported linewidth was ~50 kHz, prior to this thesis.

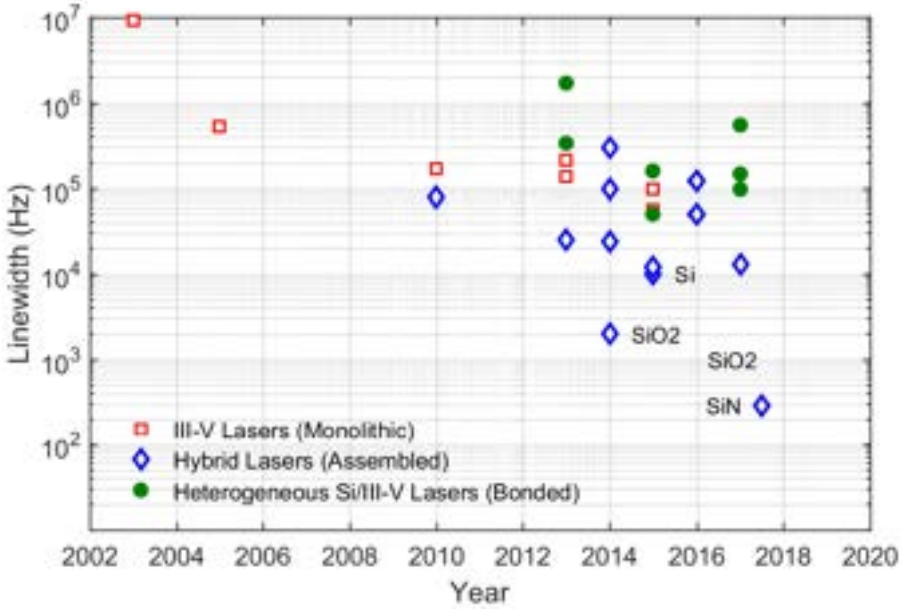

Figure 1.1 Widely-tunable integrated lasers linewidth progress in time. The authors make a distinction between III/V based monolithic lasers, hybrid lasers where III/V gain chips are butt coupled to passive chips, and heterogeneous integrated lasers where the III/V gain material is bonded to silicon. Reproduced from [23]. © MDPI 2017

1.2 Thesis objectives

The goal of this work is to lower the linewidth in heterogeneous Si/III-V lasers to 100s Hz linewidth level. To accomplish this immense improvement, we first revisit and optimize the architectural design of the heterogeneous Si/III-V integration platform based upon the work developed at UCSB over years [24]–[26]. This step would be crucial in high performances of

photonic components on device level, as well as photonic integrated circuits on system level. We then implement new waveguide structures to achieve ultralow propagation loss on silicon waveguides. High performing silicon passive components are then be seamlessly adopted as an integral part of the Si/III-V laser cavity to deliver ultralow noise lasers fully integrated on silicon.

1.3 Thesis outline

This thesis presents the development of an advanced class of fully integrated laser diodes with ultralow frequency noise for use in photonic integrated circuits. The optimization includes redesigning or newly designing numerous photonic components.

Chapter 2 focuses on optimizing heterogeneous Si/III-V photonic architecture for high performing photonic circuits in general. It begins with selection of the waveguide architecture for maximum freedom in active component design space. Basic passive and active components' designs and characteristics will be described. This is the photonic platform upon which all the lasers and photonic circuits in this thesis are built.

Next, in Chapter 3, we describe the details of the designs, theoretical modeling, and complete characterization of dual-ring mirror based tunable lasers using the standard waveguides on the heterogeneous Si/III-V photonic platform developed in Chapter 2.

Chapter 4 contains details of the development of ultralow loss silicon waveguides. Design considerations, theoretical analysis and characterization results of the ultralow loss waveguide and its derived high Q resonant photonic passive devices is presented.

Chapter 5 shows the designs and characteristics of the first class of ultralow noise lasers based on multiring mirror as the extended cavity. The laser diodes simultaneously accomplish an ultrawide wavelength tuning range and an ultralow frequency noise.

Chapter 6 presents the second class of the ultralow noise lasers based on a physically long and weak Bragg gratings. The characteristics of mode hopping, as well as frequency and RIN noise will be discussed.

Chapter 7 showcases a successful photonic integrated circuit which is comprised of all device components on the heterogeneous Si/III-V photonic platform. The design, characterization of gyroscope sensitivity and potential of frequency modulated lasers in lowering gyroscope's noise will be discussed.

Chapter 8 concludes with a summary of achievements and comparison with other material system regarding waveguide loss and laser linewidth. It will end with a proposal for future work for further improvements of the laser performances

There are three appendices at the end of the thesis. Appendix 1 presents a rigorous and thorough analysis of the spectral responses of generic multiring mirrors, which were the key structures for the widely tunable low noise lasers. Appendix 2 describes a robust method for characterizing waveguides and couplers using UMZI test structures. Finally, Appendix 3 shows a brief fabrication process flow of the devices in this work.

References

[1] S. L. I. Olsson, J. Cho, S. Chandrasekhar, X. Chen, P. J. Winzer, and S. Makovejs, "Probabilistically shaped PDM 4096-QAM transmission over up to 200 km of fiber using standard intradyne detection," *Opt. Express*, vol. 26, no. 4, p. 4522, 2018.

[2] Z. L. Newman *et al.*, "Photonic integration of an optical atomic clock," *arXiv*, 2018.

[3] D. T. Spencer *et al.*, "An optical-frequency synthesizer using integrated photonics," *Nature*, vol. 557, pp. 81–85, 2018.

[4] M. G. Suh, Q. F. Yang, K. Y. Yang, X. Yi, and K. J. Vahala, "Microresonator soliton dual-comb spectroscopy," *Science (80-.).*, vol. 354, no. 6312, pp. 1–9, 2016.

[5] J. Geng, C. Spiegelberg, S. Jiang, and A. Abstract, "Narrow Linewidth Fiber Laser for 100-km Optical Frequency Domain Reflectometry," *IEEE Photonics Technol. Lett.*, vol. 17, no. 9, pp. 1827–1829, 2005.

[6] C. Middleton, S. Meredith, R. Peach, and R. Desalvo, "Photonic frequency conversion for wideband RF-to-IF down-conversion and digitization," *2011 IEEE Avion. Fiber-Opt. Photonics Technol. Conf.*, pp. 115–116, 2011.

[7] D. Marpaung, C. Roeloffzen, Heideman, Rene G., Leinse, Arne, S. Sales, and J. Campany, "Integrated microwave photonics," *Laser Photon. Rev.*, vol. 7, no. 4, pp. 506–538, 2013.

[8] P. A. Morton and Z. Mizrahi, "Low-cost, low-noise hybrid lasers for high SFDR RF photonic links," *2012 IEEE Avion. Fiber- Opt. Photonics Technol. Conf.*, pp. 64–65, 2012.

[9] J. Hulme *et al.*, "Fully integrated microwave frequency synthesizer on heterogeneous silicon-III/V," *Opt. Express*, vol. 25, no. 3, p. 2422, 2017.

[10] J. Yao, “Microwave Photonics : Photonic Generation of Microwave and Millimeter-wave Microwave Photonics : Photonic Generation of Microwave and Millimeter-wave Signals,” *Int. J. Microw. Opt. Technol.*, vol. 5, no. 1, pp. 16–21, 2010.

[11] T. J. Kane and R. L. Byer, “Monolithic, unidirectional single-mode Nd:YAG ring laser,” *Opt. Lett.*, vol. 10, no. 2, p. 65, 1985.

[12] “Continuous Wave Single Frequency IR Laser NPRO 125/126 Series.” .

[13] “NP Photonics.” .

[14] “Koheras AdjustiK E15.” .

[15] A. Verdier, G. De Valicourt, R. Brenot, H. Debregeas, H. Carr, and Y. Chen, “Ultrawideband Wavelength-Tunable Hybrid External-Cavity Lasers,” *J. Light. Technol.*, vol. 36, no. 1, pp. 37–43, 2018.

[16] B. Stern, X. Ji, A. Dutt, and M. Lipson, “Compact narrow-linewidth integrated laser based on a low-loss silicon nitride ring resonator,” *Opt. Lett.*, vol. 42, no. 21, p. 4541, 2017.

[17] Y. Fan *et al.*, “290 Hz Intrinsic Linewidth from an Integrated Optical Chip-based Widely Tunable InP-Si3N4 Hybrid Laser,” *Conf. Lasers Electro-Optics*, vol. 161, no. 2011, p. 2013, 2017.

[18] H. Guan *et al.*, “Widely-tunable, narrow-linewidth III-V/silicon hybrid external-cavity laser for coherent communication,” *Opt. Express*, vol. 26, no. 7, p. 7920, 2018.

[19] N. Kobayashi *et al.*, “Silicon photonic hybrid ring-filter external cavity wavelength tunable lasers,” *J. Light. Technol.*, vol. 33, no. 6, pp. 1241–1246, 2015.

[20] A. W. Fang, H. Park, O. Cohen, R. Jones, M. J. Paniccia, and J. E. Bowers, “Electrically pumped hybrid AlGaInAs-silicon evanescent laser,” *Opt. Express*, vol. 14, no. 20, p.

9203, 2006.

[21] T. Komljenovic *et al.*, "Heterogeneous Silicon Photonic Integrated Circuits," *J. Light. Technol.*, vol. 34, no. 1, pp. 1–1, 2015.

[22] T. Komljenovic, D. Huang, P. Pintus, M. A. Tran, M. L. Davenport, and J. E. Bowers, "Photonic Integrated Circuits Using Heterogeneous Integration on Silicon," *Proceedings of the IEEE*. 2018.

[23] T. Komljenovic *et al.*, "Widely-Tunable Ring-Resonator Semiconductor Lasers," *Appl. Sci.*, vol. 7, no. 7, p. 732, 2017.

[24] A. W. Fang, "Silicon evanescent lasers," *ProQuest Diss. Theses*, no. March, p. 155, 2008.

[25] M. L. Davenport, "Heterogeneous Silicon III-V Mode-Locked Lasers," UCSB, 2017.

[26] T. Komljenovic, D. Huang, P. Pintus, M. A. Tran, M. L. Davenport, and J. E. Bowers, "Photonic Integrated Circuits Using Heterogeneous Integration on Silicon," *Proc. IEEE*, pp. 1–12, 2018.

Chapter 2. Heterogeneous Silicon/III-V Photonic Platform

This chapter present the designs and characteristics of key building block components in the heterogeneous Si/III-V photonic platform. We begin with selection of the optimal waveguide architecture, including the silicon device thickness and waveguide geometry. Then, we discuss several essential building blocks for integrated circuits, from passive to active components. The component designs and characteristics are explained.

2.1 Silicon photonic waveguides

2.1.1 *Thickness selection*

To enable a full design space for photonic devices in Si/III-V heterogeneous platform, maximum control of the optical mode confinement in the gain (III-V) layer and passive (silicon) layer should be obtained by engineering the waveguide widths of the III-V and silicon waveguides. In principle, as described in [1], [2], the ratio between effective indices of the individual III-V guide and that of the silicon guide should be tailorable from above unity (regime a.1 in *Figure 2.1a*) to below unity (regime a.3 in *Figure 2.1a*). When this condition is satisfied, an efficient and low loss optical mode transfer between the active region (III-V guides) and passive region (Si guides) can be made. For that requirement, the thickness of the SOI waveguides needs to be optimized in accordance to the III-V stacks. For vertical injection devices - the typical choice for most lasers and amplifiers, the III-V stack total thickness is roughly about 2 μm to separate the contact metal sufficiently far from the optical mode to avoid carrier absorption loss in the optical mode. As shown in *Figure 2.1b*, a thickness of 500 nm for the silicon layer results in a good index match with the III-V layer, allowing for a great flexibility in designing the mode hybridization. Other considered thicknesses, such as the

widely utilized 220 nm SOI waveguides [3] or multi-micron thick SOI waveguides [4], do not suit well because their indices are fairly far off from that of the III-V. The thickness of the silicon layer in devices developed through out all the work done in this dissertation, therefore, was chosen to be 500 nm.

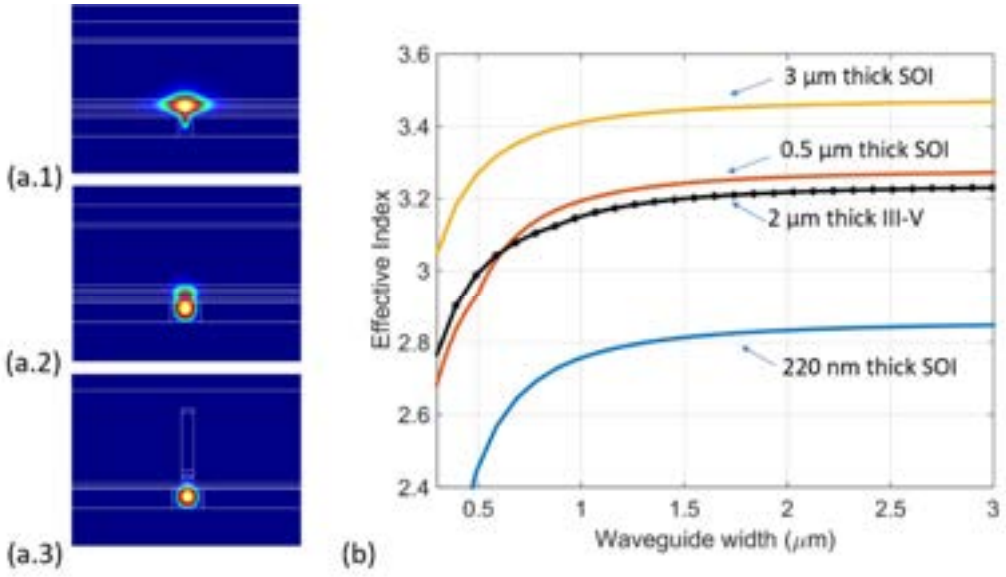

Figure 2.1 (a) Optical mode profiles of the heterogeneous (Si/III-V) waveguide with 500 nm thick silicon in 3 different operating regimes: (a.1) with a slab III-V on 0.7 µm wide silicon waveguide, which results in higher confinement in the active III-V layer. (a.2) with a slab III-V on 1.3 µm wide silicon waveguide, which results in equal confinement in the III-V and silicon. (a.3) with 0.5 µm wide III-V on 1.3 µm wide silicon waveguide, which results in higher confinement in silicon. (b) Effective indices of strip silicon waveguides of three thicknesses (220 nm, 500 nm and 3 µm) with varying width is plotted together with the effective index of a typical 2 µm thick III-V waveguide (used in [5]). Noted that all simulations were carried out at 1550 nm wavelength. © MDPI 2018

This section describes the details of the passive optical devices developed on the 500 nm thick SOI platform. We first start with the fundamental designs of the silicon rib waveguides and

discussion of the waveguide bends and waveguide terminations that are necessary elements in photonic circuits.

2.1.2 *Waveguide designs*

The waveguide geometry should be designed to meet the requirement of single mode operation. As integrated waveguides are typically confined vertically and laterally, the thickness of the core layer and the width of the waveguide play major roles in number of modes that are guided. Due to the characteristics of lithographic fabrication, one has great flexibility in varying the waveguide width (normally defined by etching) for lateral confinement while very little in the waveguide thickness (determined by material growth, bonding or deposition) for vertical confinement. We first inspect the vertical confinement by looking at modes guided in a slab waveguide structure shown in *Figure 2.2*a, where silicon is the core and silicon dioxide is used for bottom and top cladding. *Figure 2.2*b shows the effective indices of the guided modes with increasing silicon thickness. The cut-off thickness for single mode regime is roughly about 250 nm for TE polarization. With silicon thickness in this single-mode regime, one guarantees the single-mode operation in the vertical direction, and therefore can easily achieve single-mode waveguide with strip geometry as long as the width of the waveguide is chosen to not be too wide to support only single mode laterally. This is also the very reason that 220 nm was chosen and became the most commonly used in silicon photonics.

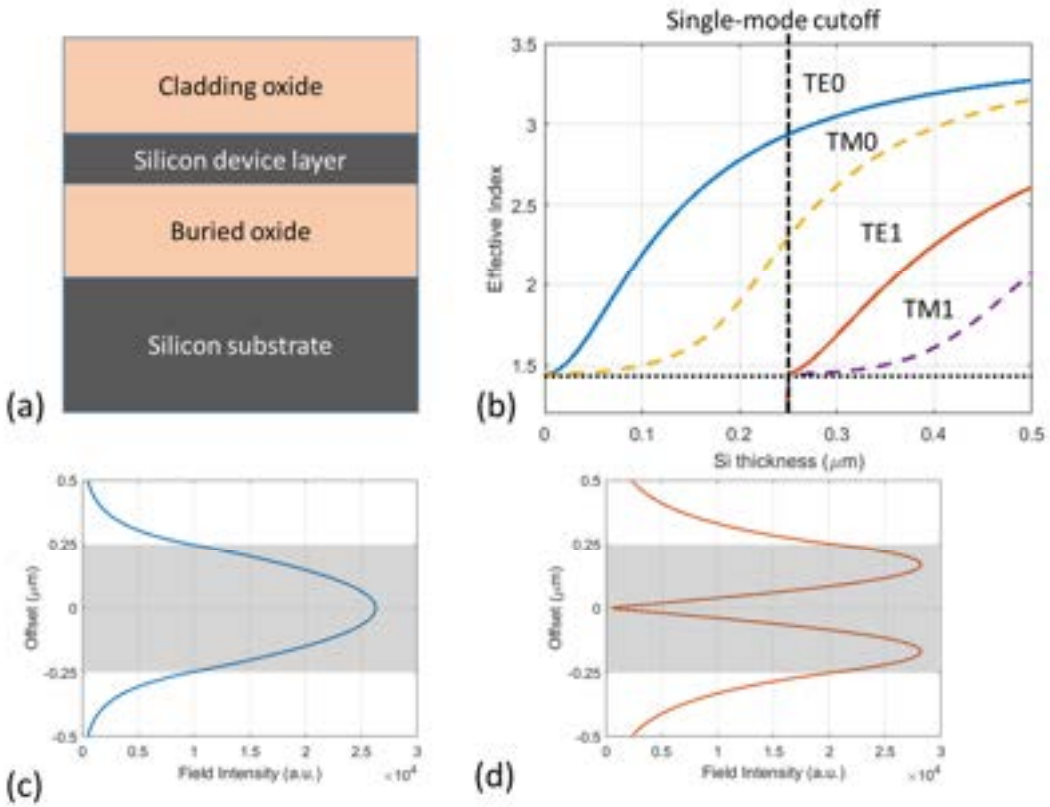

Figure 2.2 (a) Schematic of a slab (1D) waveguide where the mode is confined vertically (b) Guided slab mode indices calculation at varying silicon thickness. c) Mode profiles of the TE0 mode and d) TE1 mode in a 500 nm thick silicon slab waveguide.

As opposed to the widely used 220 nm thick waveguides, the 500 nm thickness that we use for the Si/III-V integration is far outside of the single mode regime. Other than the fundamental TE mode (*Figure 2.2*c), there also exists a high order TE mode guided vertically which is the TE1 mode plotted in Figure 2.2d. Strip waveguide geometry (silicon fully etched) with 500 nm thick silicon, therefore, supports multi-modes. Fortunately, quasi-single mode operation can be achieved with slightly modified geometry: a rib waveguide. For the rib waveguides, the silicon core would be only partially etched, forming a "rib" on the silicon slabs. Since the high order modes in the vertical direction of the waveguide have multi-peaked intensity distribution ("lobes") along the vertical axis, one of the lobes could couple into the

fundamental mode of the slab. The coupling to the slab modes works as a lateral leak-out mechanism to filter out high order modes in rib waveguides. The first essential design rule for filtering out the first vertical high-order mode is that the slab height must be larger than half of the waveguide's total height. With that being satisfied, the index of the slab's fundamental mode becomes larger than that of the first-order mode of the rib and effectively forces the high order modes to leak out.

A more rigorous and thorough analysis of the use of rib waveguide to achieve quasi-single mode operation for generic large rib waveguides is first provided by R. Soref et al. [6] and later refined and strengthened by S. Pogossian et al. [7]. The most important results from their work are the following Equations *(2.1)* and *(2.2)* which show the single-mode condition for a general rib-waveguide geometry. The geometry parameters *h, W* and *H* are respectively slab height, waveguide width and the total height of the waveguides as illustrated in Figure 2.3*b*. The constant *c* in the equation *(2.1)* *(2.1)* is determined by the material indices. In the case of a silicon waveguide with air as the top-cladding and silicon dioxide as the bottom cladding, *c*=0 should be used [8].

$$\frac{h}{H} > 0.5 \qquad (2.1)$$

$$\frac{W}{H} \le c + \frac{h/H}{\sqrt{1-(h/H)^2}} \qquad (2.2)$$

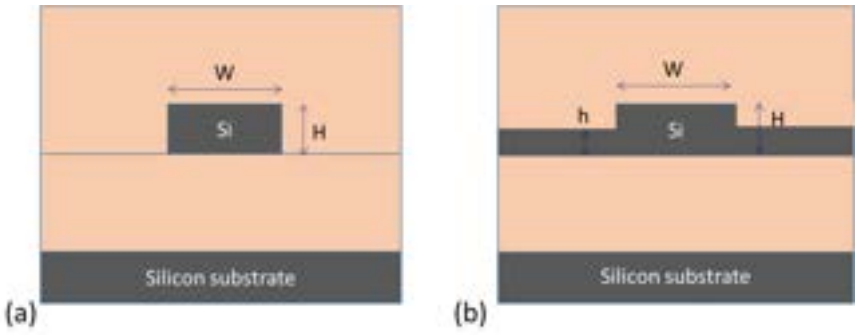

Figure 2.3 Schematic cross section of (a) Strip waveguide (fully etched) and (b) Rib waveguide (partially etched). W: waveguide width, H: Total waveguide height (or thickness), h: slab height (thickness).

As the total height of our Si waveguide is pre-determined to be 500 nm, the next parameter to determine in our waveguide design is the height of the rib. According to the analysis above, the single mode condition can be achieved as long as the slab height is larger than 250 nm, *i.e.* the etch depth for the rib formation is less than 250 nm. For the best control of the etch depth in the fabrication of the waveguides, we use an *in-situ* etch depth monitor system (Intellemetrics LEP500 Etch Depth Monitor [9]) available in the UCSB Nanofab cleanroom. It is a laser reflectometry system in which a laser beam (of 670 nm wavelength) is irradiated to the samples and the reflected signal is detected by a photodetector. For the stack of 500 nm silicon on 1000 nm buried oxide, the reflected signal versus the silicon etch is modelled as shown in *Figure 2.4*. There are a few favorable etch depths marked in red corresponding to the notches of the trace. We chose 231 nm etch depth since it is the favorable point closest to half of the total thickness.

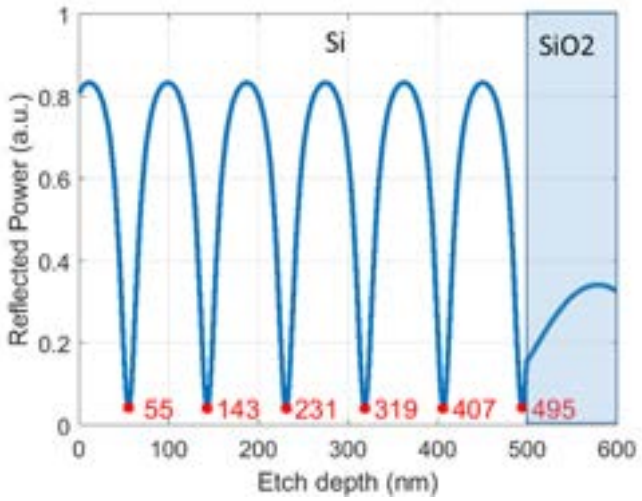

Figure 2.4 Reflected power vs etch depth trace of the stack of 500 nm Si on 1000 nm SiO_2 using Intellemetrics LEP500 etch monitor system. The etch depths at the notches are labeled in red.

The last design parameter to determine is the width of the waveguide. A commercial simulation software was used to calculate the guiding modes with high accuracy. As an example, the 2D power distribution profiles of TE0, TM0 and TE1 guided in 1000 nm wide waveguide are shown in *Figure 2.5(a, b* and *c)*, respectively. The waveguide width is swept from 1000 nm down to 150 nm and the effective indices of the supported modes are plotted in *Figure 2.5(d)*. The most important information extracted from the plot is the cut-off waveguide width for single mode operation for TE polarization, which is about 870 nm. In practice, we prefer to keep the waveguide width below 800 nm to have a safe margin for fabrication variations in the waveguide width and especially the etch depth.

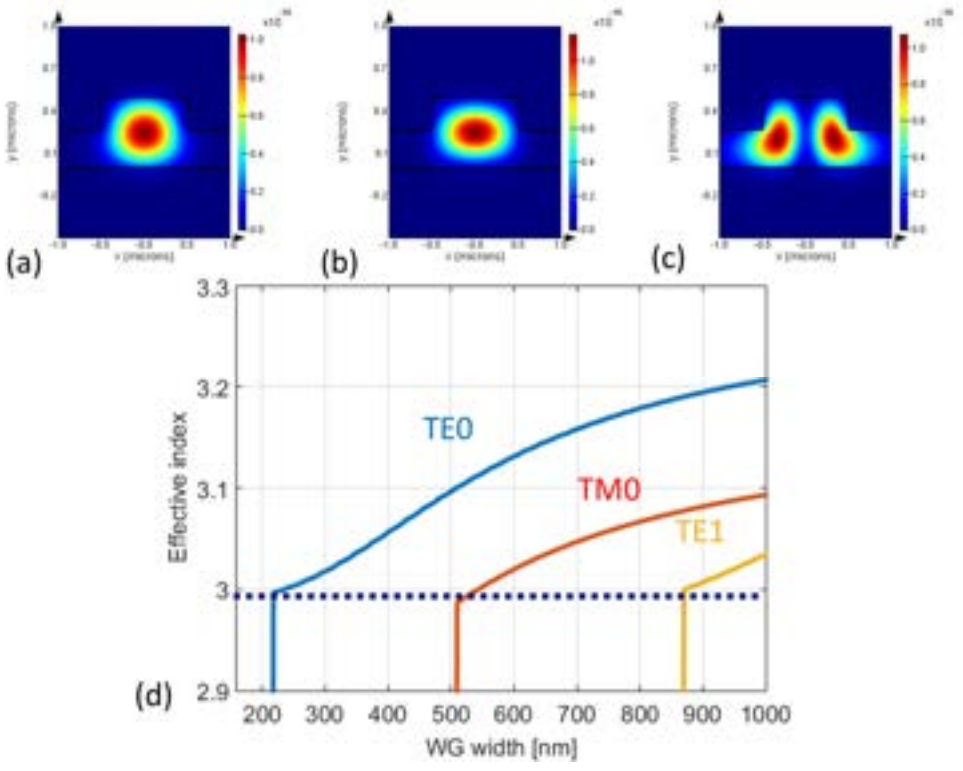

Figure 2.5 The simulated optical mode profiles a silicon rib waveguide with waveguide width of 1000 nm, etch depth of 231 nm and Si thickness of 500 nm, (a) Fundamental TE (TE0) (b) Fundamental TM mode (TM0) (c) First order TE mode (TE1). (d) Effective indices of the guided modes TE0, TM0 and TE1 at varying waveguide width.

From the plot in *Figure 2.5(d)* we also see that the cut-off index of the guiding modes for the 231 nm rib waveguide is about 2.98. This cut-off index is exactly equal to the index of the TE fundamental mode of the 269 nm high slab found in the index plot shown in *Figure 2.2*b (for the 1D waveguide). Any optical modes that have index smaller than the cut-off index would get coupled to the slab mode and leak out, as explained earlier in this section. Therefore, this cut-off index is also called slab cut-off.

2.1.3 *Waveguide routing: bends and terminations*

Waveguide routing is inevitable in PICs. The waveguides have to be bent in order to route the light around the chip and to the optical IO ports. The most commonly used types of bends for PICs include S shaped bend, 90-degree bend and 180-degree bend. Examples of these bends are shown in *Figure 2.6*.

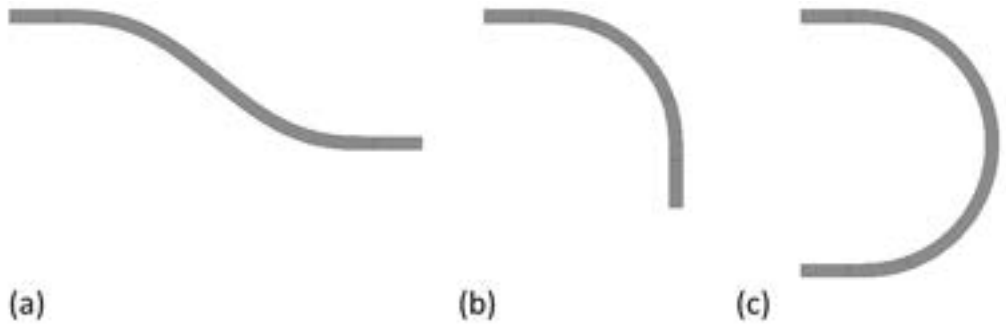

Figure 2.6 Common types of routing bends in photonic integrated circuits (a) S-shaped bend (b) 90-degree bend and (c) 180-degree bend.

It is desirable to have small bend radius to save chip real-estate. Thanks to a high contrast index between the core (Si) and cladding (oxide or air), fully etched silicon waveguides have extremely small bend radius, lower than 10 μm [10]. In rib waveguides, since the optical modes can "leak out" more easily by coupling to the slab modes when bent, the critical bent radius needs to be larger. For our standard rib waveguides with the 231 nm etch depth, the bend losses of the fundamental TE mode were simulated with a commercial mode solver software (shown in *Figure 2.1*). Considering that the typical waveguide propagation losses of these waveguide width are about a few dB/cm, we would want to have bend loss lower than 0.1 dB/cm – one order of magnitude lower than the dominant scattering loss. Near the single mode regime borderline, where waveguide width is about 800 nm, the bend radius should be larger than 40 μm to have negligible bend loss. Note that the bend loss quickly increases as the waveguide width decreases, so it is important to check bend loss wherever smaller waveguides are used.

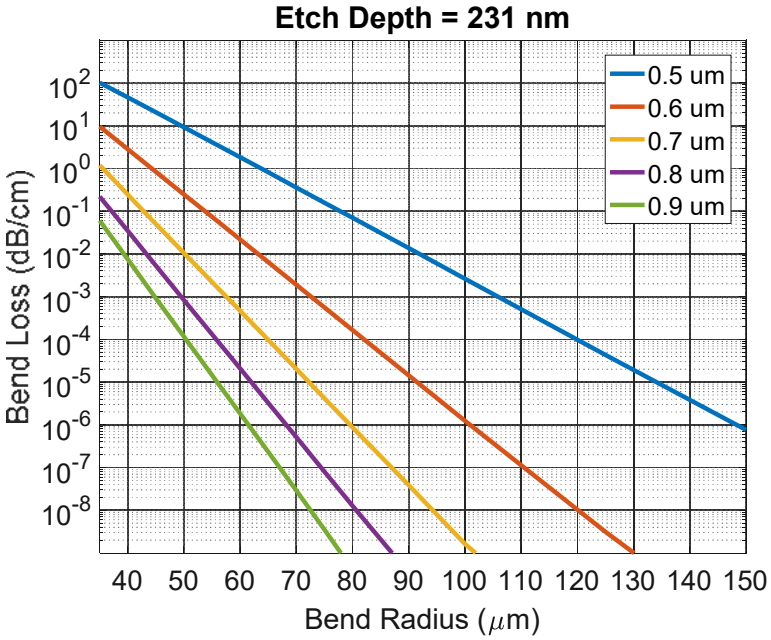

Figure 2.7 Simulated bend loss of the fundamental TE mode of the 231 nm etched rib waveguides for varying waveguide widths.

2.1.3.1 Adiabatic bends

Transitions between two curves that have different curvature could cause power losses due to the mode mismatch between the modes in the two. As an example, the mode profiles of TE0 modes in straight waveguide and 40 μm radius circular bend of an 800 nm wide rib waveguide are shown in *Figure 2.8(a)* and *(b)*, respectively. The difference in the curvatures of the circular bend (1/40 μm^{-1} curvature in this case) and a straight waveguide (zero curvature) resulted in the mode shape and positional mismatch. If the transition between the two is made continuous (zero waveguide offset) then the TE0 mode from the circular bend would lose 1.14% power in the transmission to the TE0 mode (or 0.057 dB loss) of the straight waveguide. 0.1% (-21.5 dB) power of the circular bend TE0 mode actually excites the fundamental TM0 mode in the straight waveguide. One common mitigation method is to implement a waveguide offset between straight and circular bend. This intentional offset corrects for the mode positional mismatch. In the example here, an optimal offset of +37.5 nm reduces the transition TE0 →TE0 loss down to 0.37%. However, the mismatch is still not fully eliminated, resulting in a transition loss every time a joint from straight to curved waveguide is needed.

A more ideal solution for this problem is to use an adiabatic bend to connect the two waveguides. The curvature of the adiabatic bend gradually changes from the curvature of the departure waveguide to that of the destination waveguide. When the curvature change is gradual and smooth, power loss due to mode mismatch is theoretically eliminated. In this work, we exploit so-called sine bends to form adiabatic bends.

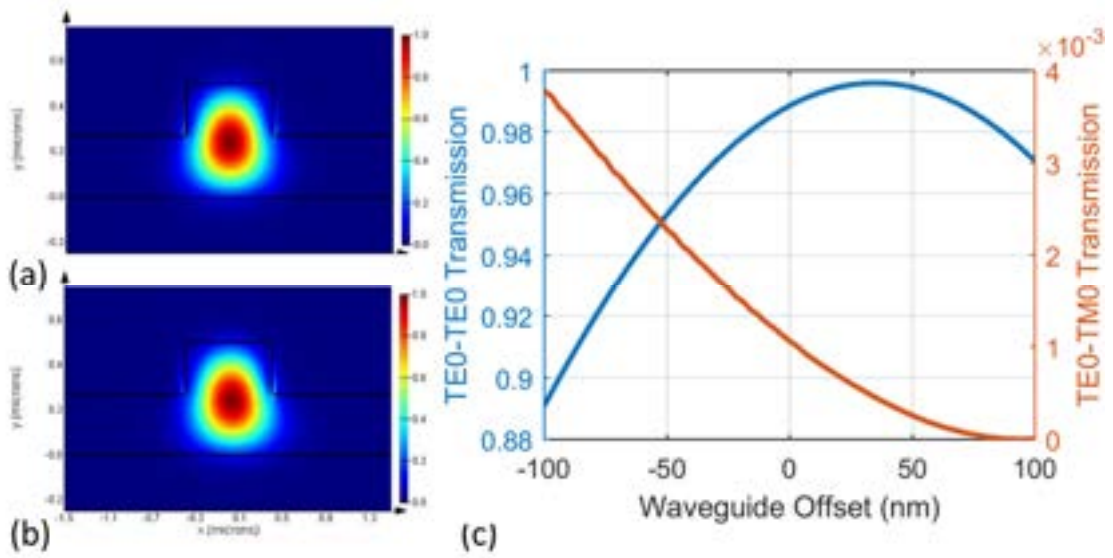

Figure 2.8 (a) Electric field distribution of TE0 mode in straight waveguide (b) Electric field distribution of TE0 mode in the circular bend (c) Waveguide offset versus power transmission from circular bend to straight waveguide for TE0→TE0 and TE0→TM0.

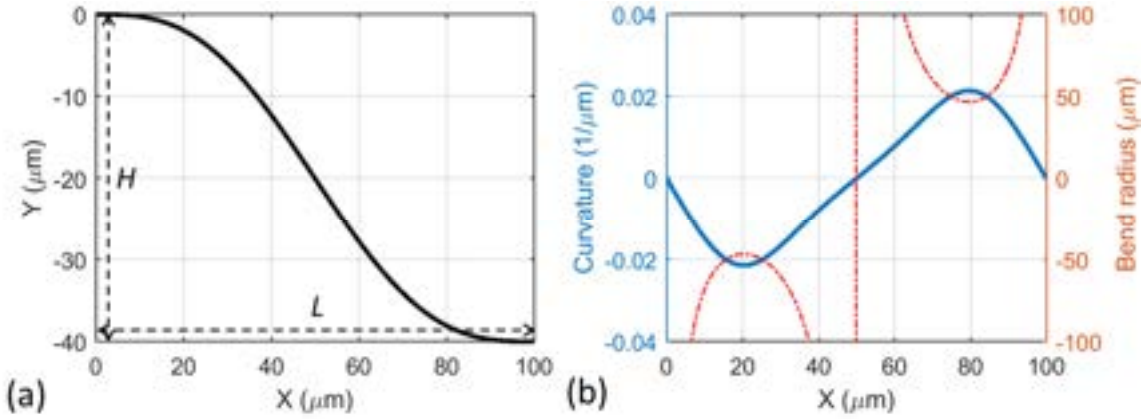

Figure 2.9 (a) Graph of a sine bend connecting two straight waveguides with L = 100 μm offset in X and H=40 μm offset in Y direction. (b) The curvature and corresponding bend radius along the sine bend.

An S-shaped full sine bend is mathematically described by the Equation *(2.3)* below.

$$y = -\frac{x}{L}H + \frac{H}{2\pi}\sin\left(2\pi\frac{x}{L}\right) \quad (2.3)$$

Here, L and H are respectively the offset in the X and Y directions. *Figure 2.9(a)* plots this sine bend for the case of L = 100 μm and H=40 μm. The curvature and equivalent bend radius along the bend is plotted in *Figure 2.9(b)*. The curvature change is continuous at every point on the bend, allowing for an adiabatic mode transfer between bends that have different curvatures.

Using parts of the sine bend with an arc of circular bend, we can form 90-degree and 180-degree bends to connect two straight waveguides pointing in different directions, as illustrated in *Figure 2.10(a-b)*. The first straight waveguide is connected to a part of a sine bend. The sine bend gradually changes curvature from zero at one end (contact point to the straight waveguide) to a non-zero curvature on the other end. A circular bend of the same curvature would follow and complete the angle rotation. Another part of a sine bend is used at the end to gradually lower the curvature to zero at the bend's end point to match with the targeted straight waveguide.

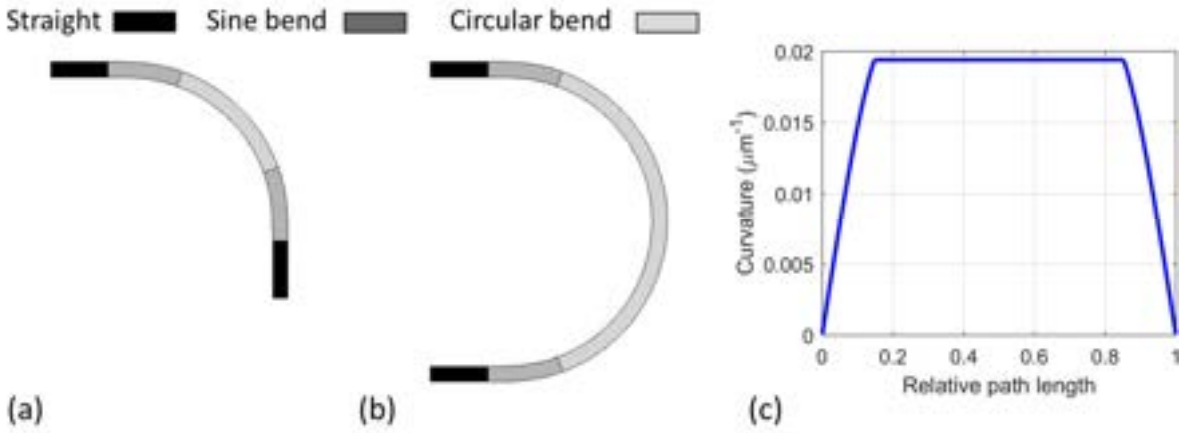

Figure 2.10 (a) Construction of a 90-degree adiabatic bend from sine bend and circular bend (b) Construction of 180-degree adiabatic bend from sine bend and circular bend (c) Curvature along the path length of an adiabatic bend constructed with sine and circular bend.

2.1.3.2 Waveguide Terminations

Waveguide terminations are necessary so that unused photons in the circuits should escape the photonic circuits with negligible effects such as reflection or cross coupling. The simple way we implement the terminations in this work is to make the waveguide very lossy with small bend radii. Multiple 180-degree adiabatic bends with decreasing waveguide widths and bend radii are connected to form multi-turn spiral. To be even safer, the end of the waveguide termination is angled, as illustrated in *Figure 2.11*.

Although it is tempting to do as many turns to make the termination extremely lossy, one should not overuse the number of turns when the termination spirals are under the III-V/Si bonding area. The small fill factor within the spiral areas (can be seen in *Figure 2.11*) could severely hurt the III-V/Si bonding success rates there. In fact, with only several turns at bend radius of tens of microns, the bending loss should be well below -70 dB, which is already sufficient for most applications.

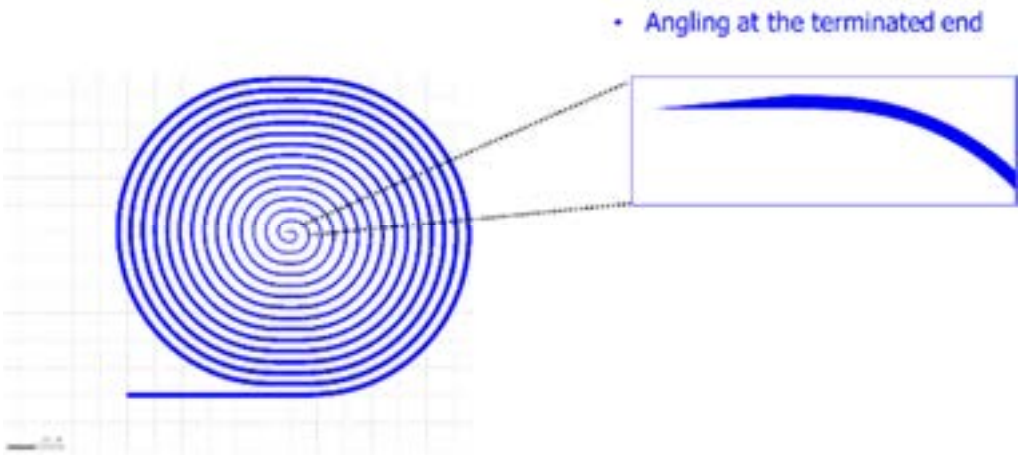

Figure 2.11 An example of waveguide termination using multi-turn spiral.

2.1.4 *Waveguide loss*

We fabricated the passive silicon waveguides using deep-UV lithography followed by a fluorine based pseudo-Bosch dry etching process detailed elsewhere [11]. The etch depth was achieved within 5 nm deviation thanks to the use of an *in-situ* etch depth monitor system [9]. Thermal oxide serves as the bottom buried oxide (BOX) while the top cladding is deposited oxide, either by PECVD or sputtering. Each cladding layer is 1 μm thick to minimize substrate leakage or loss due to the metal heaters, which are commonly put on the top of the waveguide for phase tuning. To characterize the waveguide propagation loss, we use the coherent optical frequency domain reflectometry (OFDR) technique with a commercially available system (Luna Inc. OBR 4400) [12]. Spirals of waveguides with varying waveguide widths (650 nm, 800 nm, 1 μm and 3 μm) are made with a minimum bend radius of 150 μm, as shown in the inset of *Figure 2.12(a)*. Since the bend radius used in the spirals is much larger than critical bend radius even for smallest waveguide width of 650 nm, the propagation loss is not limited by bend loss. The background doping level of the SOI wafers used here is about $3 \cdot 10^{13}$ cm^{-3}, corresponding to a carrier absorption loss of about 0.001 dB/cm, which is basically negligible. The loss is, therefore, expected to be dominated by scattering loss, originated from the waveguide line-edge roughness and sidewall roughness.

The measured OBR trace for the 800 nm wide waveguide is plotted in red color in *Figure 2.12(a)* A linear fit (black line) is used to calculate the loss, which is half of the fitted slope. The extracted loss versus wavelength is extracted for all of the waveguides and plotted in *Figure 2.12(b).* Loss for typical channel single-mode waveguide – 800 nm width – is lower than 1 dB/cm. Smaller waveguide of 650 nm width, which is typically used in directional couplers for strong coupling ratio, has an average loss of 1.2 dB/cm across the C and L bands.

Multimode waveguides with larger widths have much lower loss – 0.8 dB/cm for 1 μm width and 0.65 dB/cm for 3 μm width. This width dependency confirms that the propagation loss is mainly caused by scattering. As waveguide width increases, the guided fundamental mode is confined better in the rib and interacts less with the edges of the ribs, effectively leading to lower scattering loss.

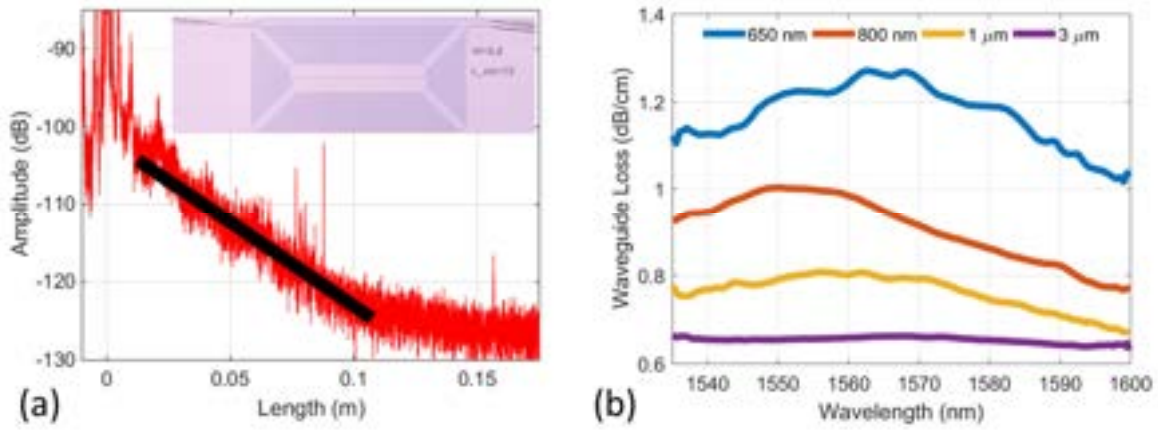

Figure 2.12 (a) Optical Backscatter Reflectometry (OBR) data from the spiral with 800 nm waveguide width. A linear fit of the waveguide backscatter is shown with the black line. The propagation loss of the waveguide can be approximated as 1/2 of the slope of the fitted line. Inset: Microscopic image of a 15 cm long spiral of 800 nm wide waveguide. (b) Extracted wavelength dependence of the propagation loss of 650 nm, 800 nm, 1 μm and 3 μm wide waveguides.

2.2 Passive photonic components

2.2.1 *IO mode size converters*

Due to the large mismatch in the mode field size between Si waveguide and optical fiber, it is necessary to have a mode size converter at the interface. The two main approaches that are widely used include vertical grating couplers [13] and edge inverse couplers [14]. While grating couplers in general have a limited optical bandwidth and an inherent back reflection,

edge coupling is preferred because it has broader bandwidth and reduces reflection by angling or anti-reflection coating. The schematic design of the mode size converter transitioning from 500 nm thick Si waveguide to optical fiber is shown in *Figure 2.13(a)*. The converter comprises two parts: a bi-level taper and an inverse taper. Through the bi-level taper, the optical mode from 500 nm x 600 nm rib Si waveguide is squished to the mode in thinner 269 nm x 600 nm Si waveguide. The waveguide is then tapered to 269 nm x 150 nm waveguide. Since the Si core is now too small, the optical mode is no longer well confined in Si but expands to the oxide cladding, which largely increases the mode field area and matches better with optical fibers. The waveguide is also angled to 7° respective to the polished facet to decrease back reflection.

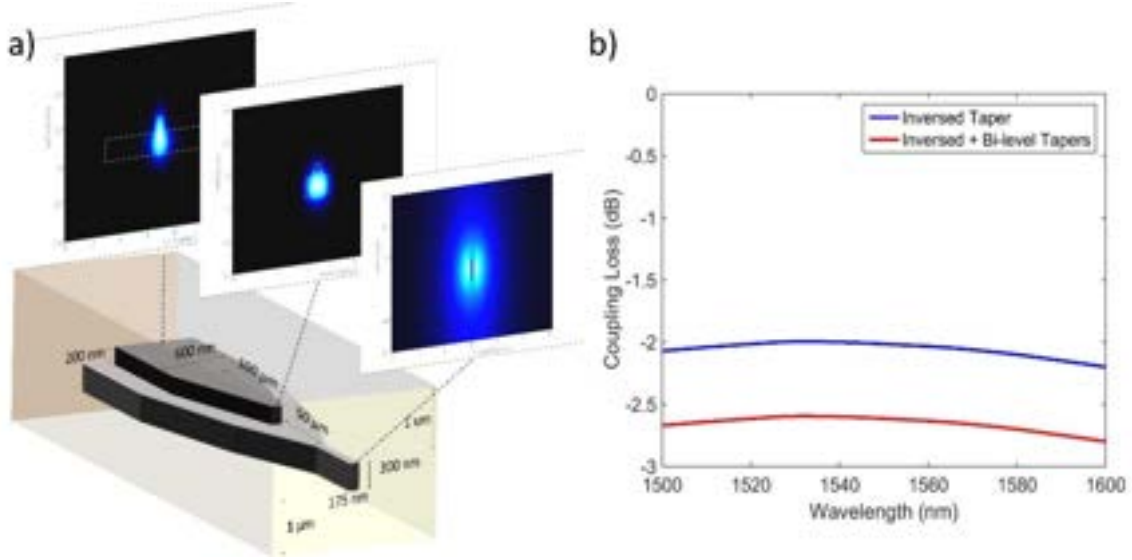

Figure 2.13 (a) Schematic of the bi-level taper and the inverse taper for waveguide-fiber. The mode evolution along the coupler is shown to illustrate the working principle. (b) Blue line: FDTD simulated coupling loss from 269 nm x 150 nm Si waveguide to 2.5 μm spot-size lensed fiber. Red line: Total coupling loss including the bi-level taper. The waveguide was angled to 7° and the lensed fiber approach angle was 8° respective to the chip facet. © OSA 2017

The bi-level taper was simulated with the eigenmode expansion method and the averaged transmission loss over C-band was estimated to be -0.6 dB. In addition, the coupling efficiency from the Si inversed taper to a 2.5 μm spot-size fiber was done with FDTD simulation and the average coupling loss over C-band is about - 2.05 dB, as shown in *Figure 2.13(b*). In total, the mode converter is expected to have -2.7 dB coupling loss over the C-band. All simulations only considered TE mode.

Polarization maintaining (PM) lensed fibers with the mode diameter of ~ 2.5 μm were used to couple the Si waveguide with mode size converters. Transmission power through a Si straight waveguide with two mode converters at two ends was recorded while laser wavelength was swept over 1525 - 1575 nm. The same measurement was also taken for transmission from fiber to fiber as a reference. The coupling efficiency was then extracted, taking into account the extra 0.2 dB propagation loss of the 0.2 mm Si straight waveguide, as shown in *Figure 2.14*. The averaged coupling loss is determined to be -3 dB. The 0.3 dB discrepancy between measurement and simulation can be attributed to the propagation loss along the mode converter structure.

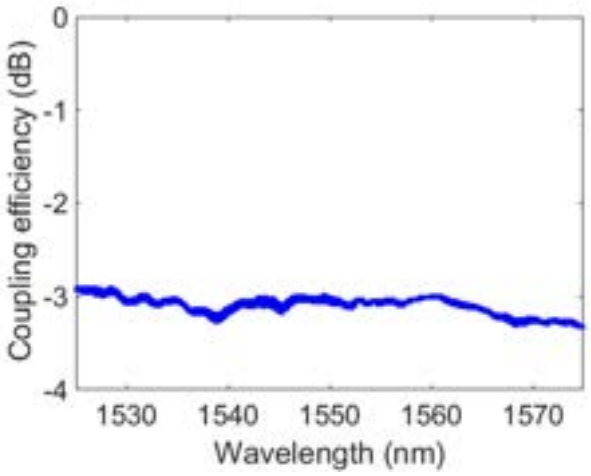

Figure 2.14 Coupling efficiency between TE mode of the Si waveguide and 2.5 μm mode diameter lensed polarization maintaining fiber. © OSA 2017

2.2.2 *Optical adiabatic couplers*

The design of an adiabatic 3-dB 2×2 coupler is illustrated in *Figure 2.15(a)*. The coupler comprises three sections: the first section (300 μm long) where the two ridge waveguides with different widths (600 nm and 800 nm wide) slowly come close to each other using S-bends, the coupling section (400 μm long) where the two asymmetric waveguides are linearly tapered to 700 nm wide waveguides, and the third section (300 μm long) where each 700 nm wide waveguide is guided to one of the output waveguides by two other S-bends. We used the eigenmode expansion method to simulate the propagation of modes through the structure. *Figure 2.15(a)* also shows, as an example, how the mode propagates and splits through the coupler when light is input to the 800 nm wide waveguide. The input mode first excites the fundamental (even) mode of the coupler modes, then this even mode transmits adiabatically to the even mode of the symmetric 700 nm wide waveguides at the end of the coupling section; after that, the power then splits equally to the two output waveguides. The simulation result in *Figure 2.15(b)* shows 50±3% splitting ratio of the adiabatic coupler over C+L bands.

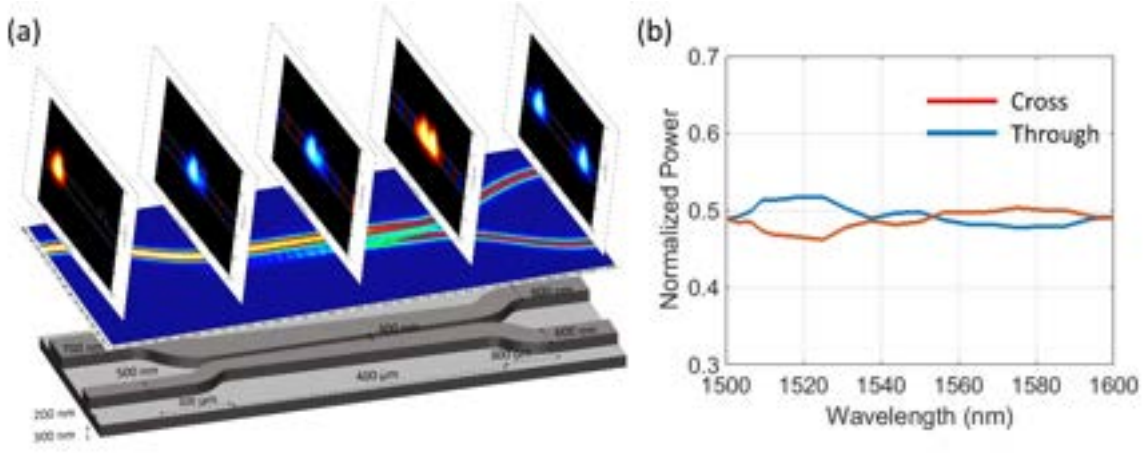

Figure 2.15 (a) Schematic of the 3-dB adiabatic coupler. The simulated mode evolution along the coupler is shown to illustrate the working principle. (b) Simulated wavelength dependence of the coupler. © OSA 2016

Cascading two adiabatic 3-dB couplers back to back with a phase tuner on one of the arms could form a 2×2 MZI broadband switch. It is worth noting that the two adiabatic couplers are arranged in such a way that both input and output sides are asymmetric (waveguides are 700 nm and 500 nm wide) while the two waveguide arms connecting the two couplers are both 600 nm wide as shown in *Figure 2.16*. Theoretically, such configuration results in the switch being "normally off", *i.e.* no light goes through the cross-port when no extra phase difference is introduced to the MZI arms (see the mode propagation simulation at the bottom of *Figure 2.16*). The phase is thermo-optically tuned with a heater on the top of one MZI arm.

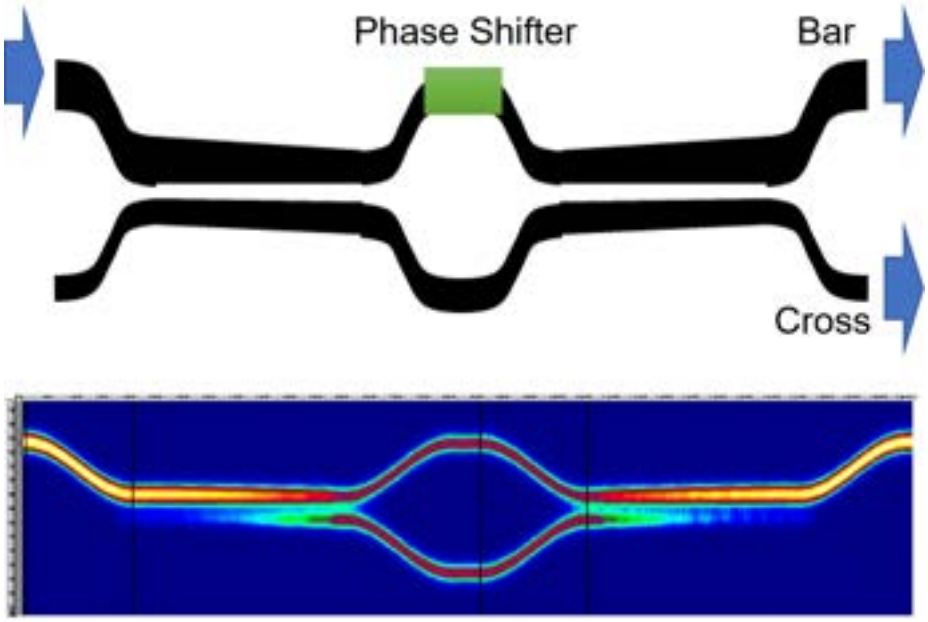

Figure 2.16 Schematic of the MZI switch based on 3-dB adiabatic couplers. The simulated mode evolution along the coupler is shown to illustrate the working principle. © IEEE 2016

Both adiabatic coupler and optical switch were then fabricated and tested.

The 2×2 adiabatic 3-dB coupler was characterized by using a rigorous method reported in [15]. The measurement setup is shown in *Figure 2.17(a)* with a high-precision tunable laser source, high precision power sensor, a polarization controller, a polarizer and polarization maintaining (PM) fibers. The lensed fiber holder rotator was adjusted to launch TE mode

(polarization extinction ratio TE/TM > 25 dB) prior to testing. The splitting ratios versus wavelength plot of the coupler are shown in *Figure 2.17(b)* The splitter exhibited a flat wavelength response over the C-band. The normalized power splitting ratio over 75 nm wavelength range (1520 - 1595) was within 50±4.2%.

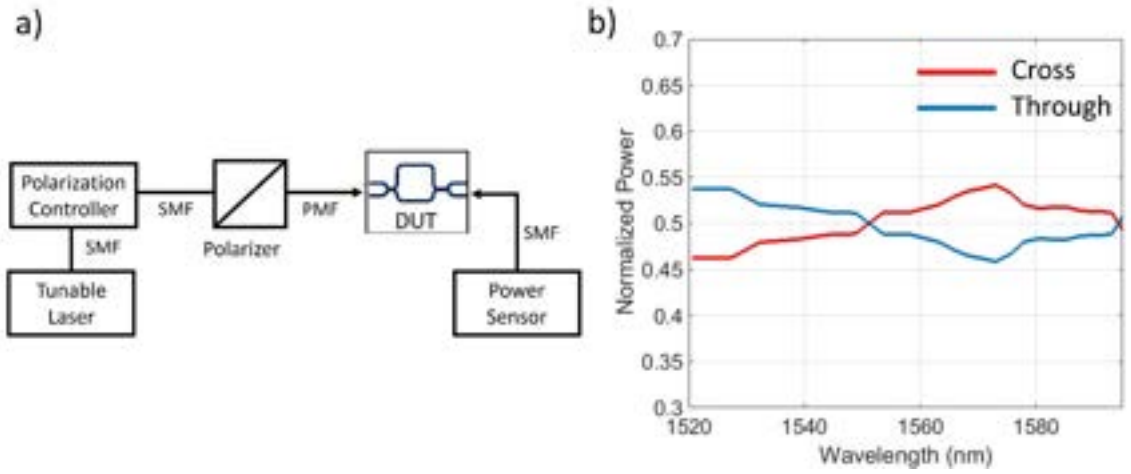

Figure 2.17 (a) Measurement setup for testing passive components. (b) Normalized splitting ratios of the fabricated adiabatic 3-dB splitter, extracted using the UMZI spectra analysis. © OSA 2016

Characterization of the adiabatic optical switch was also carried out in the same test setup. *Figure 2.18* shows the transmissions through the switch at "off" and "on" states. It clearly shows that the fabricated MZI switch achieves an extinction ratio between on and off states is > 15 dB over 120 nm wavelength range (1460 -1580 nm) in both output ports

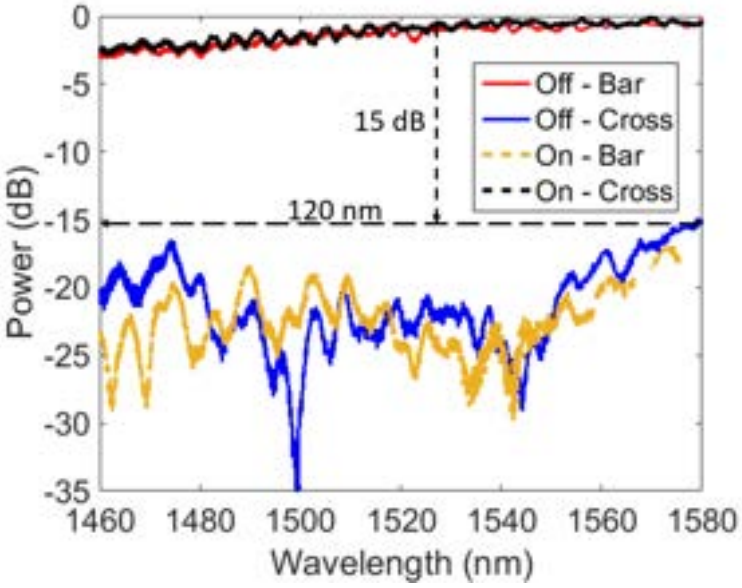

Figure 2.18 Normalized transmission spectra to the cross and bar ports at on and off states.

2.3 Active components

In this section, we discuss the designs and characteristics of several key active components for the PICs, including light sources, photodiodes and modulators. The schematic of the device cross section is illustrated in *Figure 2.19*. The silicon waveguide underneath the III-V layer is 231 nm etched rib waveguides (identical to the passive ones), and is therefore co-fabricated prior to III-V bonding. The details of the bonding process has been extensively discussed and detailed elsewhere [11], [16], [17].

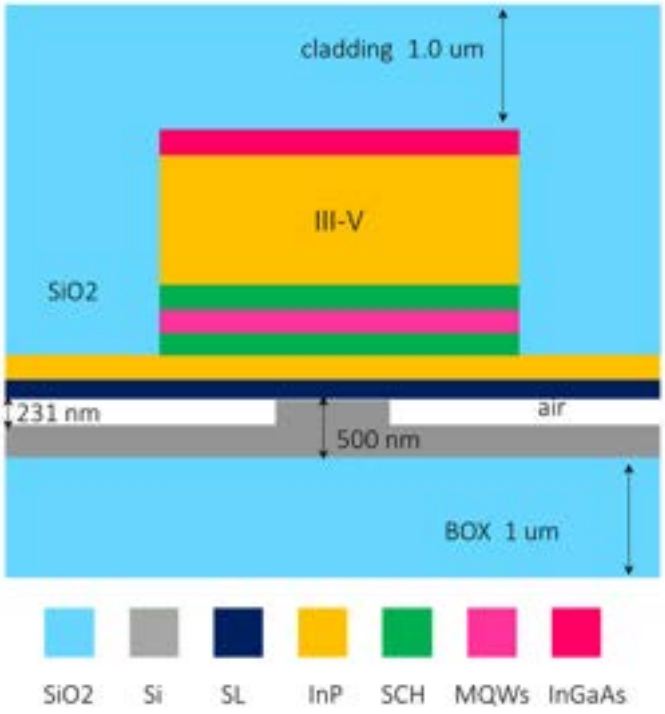

Figure 2.19 Schematic of cross section of Si/III-V heterogeneous active components (laser, photodiodes and modulators). © Elsevier 2018

2.3.1 *Light sources*

2.3.1.1 Multimode Fabry-Perot lasers

The schematic of a Fabry-Perot laser design on heterogeneous III-V/Si platform is shown in *Figure 2.20*. The III-V layer stack used as gain element for the laser has three strained InAlGaAs quantum wells (QWs) sandwiched between two separate confinement hetero-structure (SCH) layers, as shown in *Table 2.1*.

Table 2.1 Epitaxial III- V Layer Structure Used for the Lasers and Photodiodes

Layer Name	Layer Composition	Thickness (µm)	Doping level
P-contact	P-In0.53Ga0.47As	0.1	1.50E+19
Smoothing	P-1.5Q $In_{0.586}Ga_{0.414}As_{0.888}P_{0.112}$	0.025	3.00E+18
Smoothing	P-1.3Q $In_{0.729}Ga_{0.271}As_{0.587}P_{0.413}$	0.025	3.00E+18

P-cladding	P-InP	1	1.50E+18
P-cladding	P-InP	0.2	8.00E+17
P-cladding	P-InP	0.25	5.00E+17
SCH	N-$In_{0.53}Al_{0.183}Ga_{0.287}As$	0.125	1.00E+17
MQW	U-3 x $In_{0.6758}Al_{0.06}Ga_{0.2642}As$ Well (+1% CS)	3 x 0.006	
	U-4 x $In_{0.4411}Al_{0.085}Ga_{0.4739}As$ Barrier (-0.6% TS)	4 x 0.009	
SCH	N-$In_{0.53}Al_{0.183}Ga_{0.287}As$	0.125	1.00E+17
N-Contact	N-InP	0.11	2.00E+18
Superlattice	2 x N - $In_{0.85}Ga_{0.15}As_{0.327}P_{0.673}$	0.0075	1.00E+18
	2 x N-InP	0.0075	
Bonding layer	N-InP	0.01	1.00E+18

The laser cavity mirrors are formed by two loop mirrors that are realized in silicon, similar to [18]. We chose loop mirrors as they can be formed anywhere on chip (no need for facets) and the reflectivity can be chosen arbitrarily based on the coupling ratio of the coupler used. When the insertion loss of the coupler is negligible, the relationship between the reflectivity ($\mathcal{R}$) of the loop mirror and the power coupling ratio (s) of the 2×2 coupler is given by equation $\mathcal{R} = 4s(1-s)$. The back-mirror is designed to be nearly total reflective while the front-mirror has lower reflection. The high reflective mirror on the left-hand side makes use of a 3-dB adiabatic coupler (as described in the passive component section) to allow close to 100% reflectivity over a broad optical bandwidth. The lower reflective mirror on the right-hand side uses a directional coupler with variable coupling ratio.

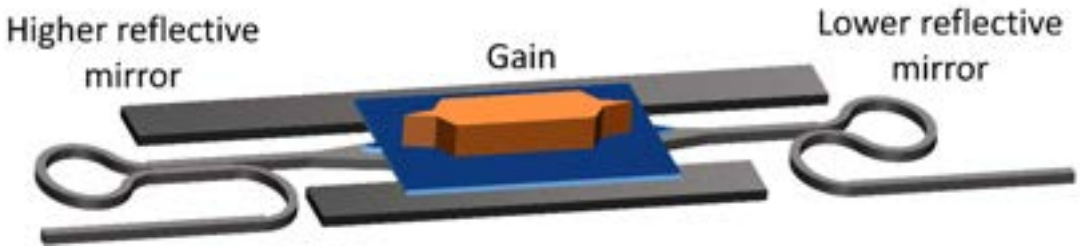

Figure 2.20 Schematic of the Fabry-Perot laser with the gain region on III-V layer and the integrated loop mirrors on silicon. © OSA 2017

A Fabry-Perot laser with 2 mm long gain section was fabricated. *Figure 2.1*(*a)* shows the LIV curves of the Fabry-Perot laser at room temperature. The threshold current is about 40 mA. The laser's optical spectrum when operating at well above threshold (150 mA) is shown in *Figure 2.1(b)*. A multi-mode lasing across the 1578 nm – 1595 nm wavelength range was observed with mode spacing of 0.07 nm corresponding to a cavity length of 4.5 mm formed by the two integrated loop mirrors.

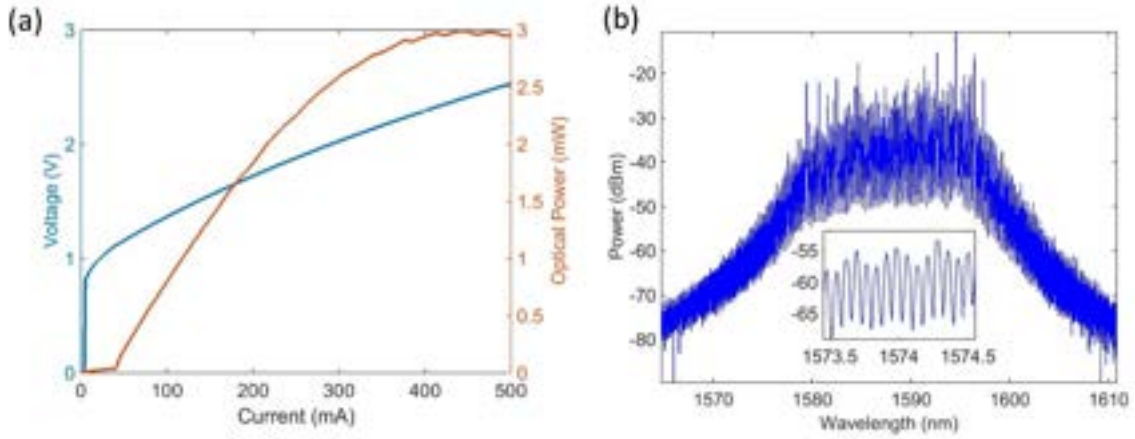

Figure 2.21 (a) LIV curves of the laser. (b) Optical spectrum of the fabricated FP laser. The inset shows the mode spacing that corresponds to the laser cavity length. © OSA 2017

2.3.1.2 Single-mode distributed feedback (DFB) laser

When the laser cavity length is increased, the longitudinal modes get closer to each other in frequency domain and the laser would have multiple lasing modes as we could see in the previous section of 2.3.1.1 Multimode Fabry-Perot lasers. For single mode operation, it is necessary to include a filter capable of filtering a single longitudinal mode across the bandwidth of the gain medium which is in the order of 10 THz (80 nm at 1550 nm). One

common way is to utilize Bragg gratings in the gain medium to realize distributed feedback (DFB) lasers. Combining filter elements into the gain section is an effective solution to shrink the size of the laser, allowing for low threshold current and high-speed direct modulation [19], [20]. Since the optical mode in heterogeneous waveguide hybridizes in both III-V and Si, the Bragg gratings can be defined solely on silicon waveguides in the silicon process prior to bonding. This is in fact a valuable advantage of the heterogeneous silicon platform over the conventional III-V monolithic platform where the formation of Bragg gratings often involves epitaxial regrowth or other complex processes. As lithography and etching on silicon can be done at large scale with perfected processes inherited from the mature silicon electronics industry, the fabrication of the Bragg gratings can be obtained with high precision; therefore, heterogeneous Si DFB lasers offer high precision control of the lasing wavelength, which is of critical importance in many applications.

The heterogeneous Si/III-V photonic platform also enables a new degree of freedom to control the coherence (or equivalently, the spectra linewidth) in the DFB lasers. By lowering the mode confinement in III-V and having the optical mode localize more in Si passive waveguide, one effectively reduces the spontaneous emission (which happens in the III-V active region) coupling rate to the lasing mode. In addition, the internal loss of the mode can be reduced and hence gives room for designers to achieve a cavity with quality (Q) factor that is orders of magnitude higher than achievable in conventional III-V monolithic lasers. A heterogeneous Si DFB laser with record low sub-kHz spectral linewidth has been successfully demonstrated with this approach [21].

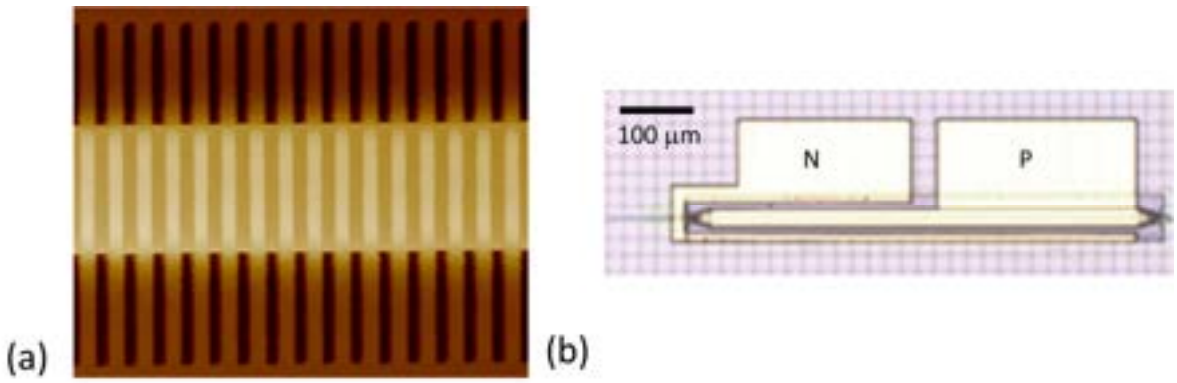

Figure 2.22 (a) AFM image of the surface grating on silicon waveguide (b) A microscopic photograph of a fabricated DFB laser on heterogeneous silicon photonics. © Elsevier 2018

Since the first DFB laser on heterogeneous silicon photonics platform was demonstrated [22], various DFB lasers have been designed for different targeted performances, *e.g.* [20], [21], [23]. In this section, we describe a simple design, compact (650 μm long) phase-shifted DFB laser that has 20 mW maximum output power and down to 400 kHz integrated linewidth. The silicon rib-waveguide under the gain section is 1.2 μm. With that width, the confinement factor in the QW region is estimated about 5%. More than 50% of the optical mode is confined in the silicon waveguide. First-order uniform gratings with a quarter-wave phase shift at the center of the cavity were defined on the silicon waveguide surface using an electron beam lithography system and then etched with an ICP etcher. The grating etch depth was only 3 nm and an AFM image is shown in *Figure 2.22(a)*. The fabrication is completed with III-V bonding and subsequent heterogeneous processes shown in the previous sections. Heterogeneous transitions and tapers were formed on two ends of the laser, transferring the modes to single mode passive silicon waveguides. A microscopic photograph of a completed laser structure is shown in *Figure 2.22(b)*.

The LI curve in *Figure 2.23(a)* shows 25 mA threshold current and maximum 22mW single-sided output power. The lasing spectrum at 150 mA is shown in *Figure 2.23(b)*. The laser

spectral linewidth is measured with the delayed self-heterodyne method [24]. A measured spectrum is plotted with a Lorentzian fit in *Figure 2.23(c)* of a 400 kHz spectral linewidth. Finally, the linewidth versus inverse output power was measured, showing expected linear relationship above threshold as shown in *Figure 2.23(d)*. The linewidth saturates and re-broadens at high injection current level possibly due to a combination of gain nonlinearity, thermal and spatial hole burning effects.

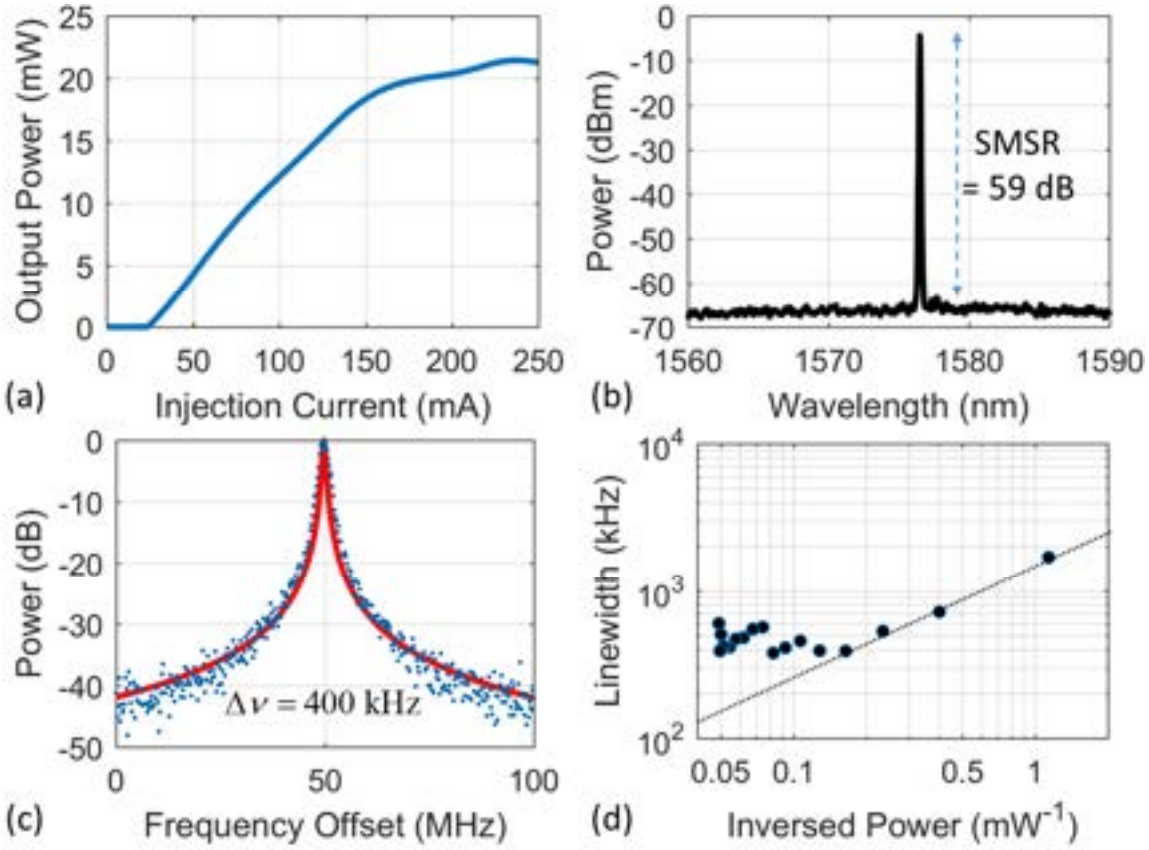

Figure 2.23 (a) Single-sided output power versus injection current. (b) A lasing spectrum shows near 60 dB side mode suppression ratio (c) Measured RF spectrum of the laser in a delayed self-heterodyne measurement with a Lorentzian fitted curve (d) Laser spectral linewidth versus inversed output power. © Elsevier 2018

2.3.2 *Photodiodes*

The photodiode used the identical three quantum well III-V stack as the gain described in Section 2.3.1.1 .The device design was similar to the one demonstrated by Park et al. [25] in which the III-V region was tilted to reduce the reflection at the waveguide transition, as shown in *Figure 2.24*. Along the hybrid region, the Si waveguide width was gradually tapered from 3 μm to 600 nm to push the mode vertically and increase the confinement factor in the quantum well region, thus achieving higher absorption and responsivity.

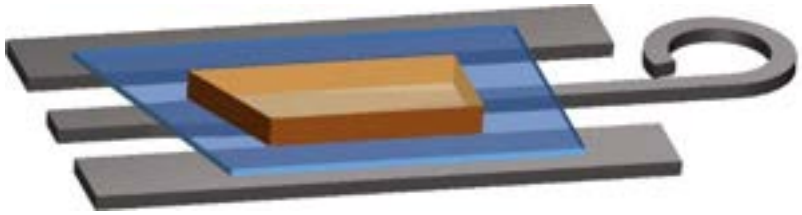

Figure 2.24 Schematic of the photodiode. The III-V layers are drawn transparent to show the change in the width of the underneath Si waveguide. © OSA 2017

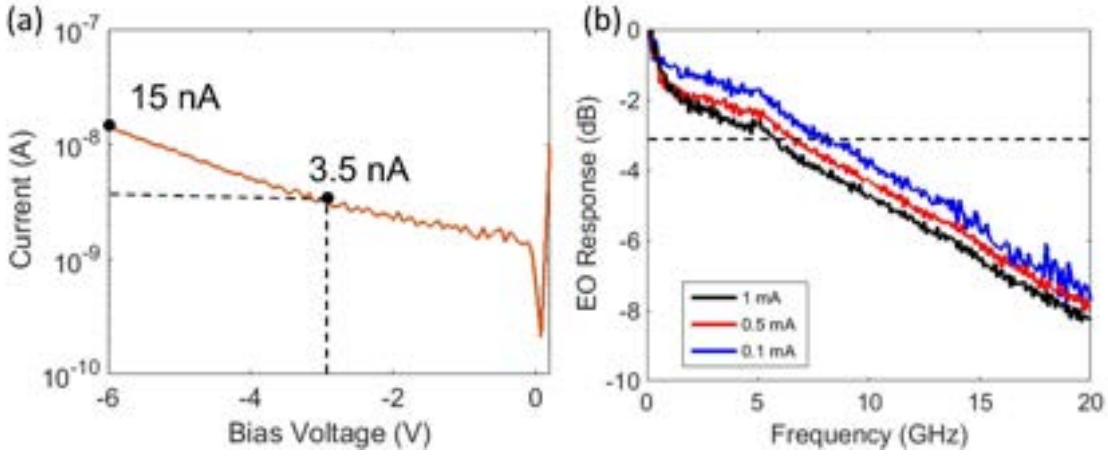

Figure 2.25 (a) Photodiode voltage-current curve at reversed bias. (b) Frequency response at different levels of photocurrent for -6 V bias. © OSA 2017

The dark-current is 4 nA at -3 V and goes up to 15 nA at -6 V bias, as shown in *Figure 2.25(a)*. The frequency response at wavelength of 1550 nm and -6 V reverse bias was measured using

the Agilent N4373A Lightwave Component Analyzer (LCA) measurement setup and is shown in *Figure 2.25 (b)*. The 3-dB bandwidth is larger than 6 GHz up to 1 mA photocurrent, with a responsivity of about 0.7 A/W.

2.3.3 *Phase Modulators*

For phase modulation, we utilized the carrier depletion effect in multiple quantum wells of AlGaInAs to realize phase modulators with broad optical bandwidth, low insertion loss and low power consumption [26] . The III-V stack for the phase modulator was modified from the design reported by Hui-wen et al. [27] and is shown in *Table 2.2*. The modification was necessary to match the thicknesses of the III-V layers for lasers and photodiodes so that a single dry etching process could be done simultaneously for forming P-mesas in all III-V stacks. In addition, the phase modulators could be laid out in a push-pull with simple layout of metal-probe on the top as illustrated in *Figure 2.26(a)*. The circuit for driving the push-pull operation is shown in *Figure 2.26(b)*.

Table 2.2 Epitaxial III-V Layer Structure Used for the Phase Modulators

Layer Name	***Layer Composition***	***Thickness (μm)***	***Doping level (cm^{-3})***
P-contact	P-$In_{0.53}Ga_{0.47}As$	0.1	1.50E+19
Smoothing	P-1.5Q $In_{0.586}Ga_{0.414}As_{0.888}P_{0.112}$	0.025	3.00E+18
Smoothing	P-1.3Q $In_{0.729}Ga_{0.271}As_{0.587}P_{0.413}$	0.025	3.00E+18
P-cladding	P-InP	1	1.50E+18
P-cladding	P-InP	0.25	8.00E+17
P-cladding	P-InP	0.25	5.00E+17
SCH	N-$In_{0.5284}Al_{0.193}Ga_{0.2786}As$	0.1	1.00E+17
MQW	U-15 x $In_{0.574}Al_{0.111}Ga_{0.315}As$	15 x 0.008	1.00E+17
	U-16 x $In_{0.468}Al_{0.217}Ga_{0.315}As$	16 x 0.005	1.00E+17

SCH	N-$In_{0.5284}Al_{0.193}Ga_{0.2786}As$	0.05	3.00E+18
N-Contact	N-InP	0.11	3.00E+18
Superlattice	2 x N - $In_{0.85}Ga_{0.15}As_{0.327}P_{0.673}$	0.0075	1.00E+18
	2 x N-InP	0.0075	
Bonding layer	N-InP	0.01	1.00E+18

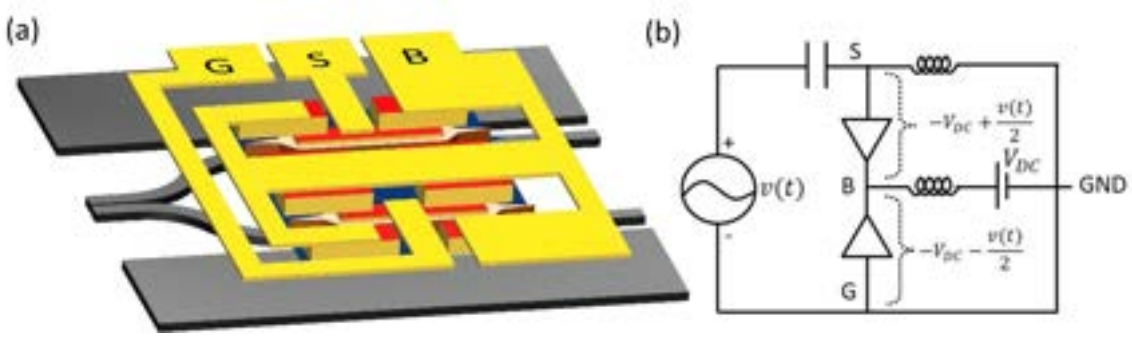

Figure 2.26 (a) Schematic of push-pull modulators. (b) The circuit diagram for the push-pull modulation operation. © OSA 2017

To measure the insertion loss of the modulators, the transmission spectrum through a stand-alone phase modulator was measured and compared with that of a reference single straight waveguide. At a reverse bias smaller than 3 V, the insertion loss is less than 1 dB over the C-band. The phase modulator was also placed in a Mach-Zehnder Interferometer (MZI) test structure to form an MZI modulator for half-wave voltage and frequency response characterization. The optical power (at a wavelength of 1550 nm) from the output waveguide of the MZI modulator was measured while DC reverse bias voltage was swept from 0 to 6 V as shown in *Figure 2.27(a)*. The half-wave voltage for 500 μm long structure is 4.2 V. The device speed was measured at varying reverse bias voltages using an HP 8703A LCA setup. The modulator exhibited a 3-dB bandwidth of about 2 GHz at -2 V bias as shown in *Figure 2.27 (b).*

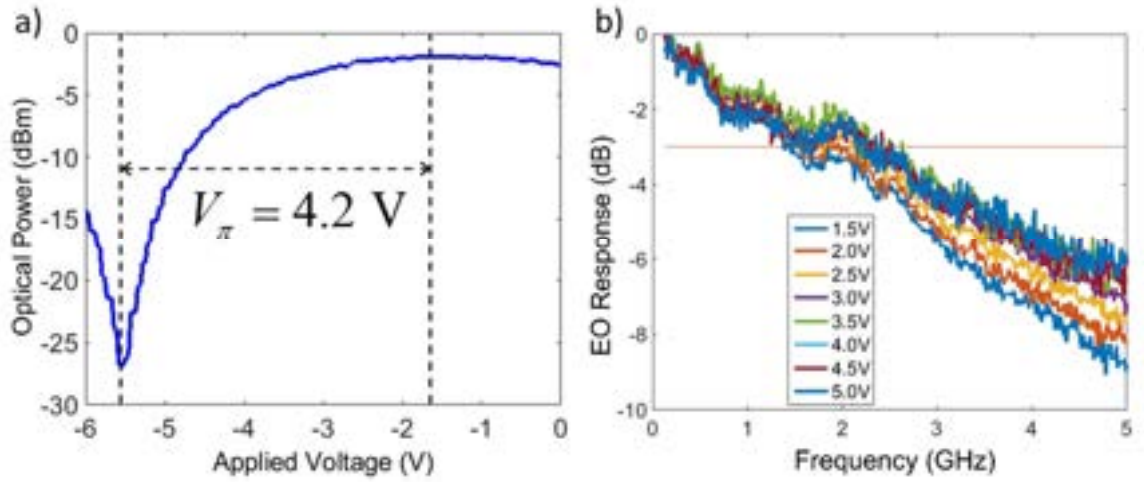

Figure 2.27 (a) MZI modulator's half-wave voltage measurement at DC bias. (b) Its frequency response at varying reversed-biases showing 3-dB bandwidth of 2 GHz. © OSA 2017

2.4 Summary

This chapter first starts with the mode analysis of the heterogeneous Si/III-V waveguide structures to point out that 500 nm thick silicon is enabling the maximal design space for device performance. We down-select the rib waveguide geometry with 231 nm etch depth to be the standard photonic waveguides in the platform. Analysis and characteristics of waveguides (bend loss, propagation loss, adiabatic bends, terminations) are presented. We then describe details of the designs and characterization of several essential building block components for photonic integrated circuits, from passives (waveguide couplers, mode size converters) to actives (FP lasers, DFB lasers, photodiodes and phase modulators). All the work in the next chapters throughout this thesis are developed based on this platform.

References

[1] A. Yariv and X. Sun, "Supermode Si/III-V hybrid lasers, optical amplifiers and modulators: A proposal and analysis," *Opt. Express*, vol. 15, no. 5, pp. 9147–9151, 2007.

[2] X. Sun and A. Yariv, "Engineering supermode silicon/III–V hybrid waveguides for laser oscillation," vol. 31403120, no. 140, 2790.

[3] K. Okamoto, "Progress and technical challenge for planar waveguide devices: silica and silicon waveguides," *Laser Photon. Rev.*, vol. 6, no. 1, pp. 14–23, Jan. 2012.

[4] T. Aalto, M. Harjanne, and M. Cherchi, "VTT's micron-scale silicon rib+strip waveguide platform," 2016, vol. 9891, p. 98911G.

[5] M. L. Davenport, S. Skendzic, N. Volet, J. C. Hulme, M. J. R. Heck, and J. E. Bowers, "Heterogeneous Silicon/III–V Semiconductor Optical Amplifiers," *IEEE J. Sel. Top. Quantum Electron.*, vol. 22, no. 6, pp. 78–88, Nov. 2016.

[6] R. A. Soref, J. Schmidtchen, and K. Petermann, "Large Single-Mode Rib Waveguides in GeSi-Si and Si-on-SO2," vol. 27, no. 8, pp. 1971–1974, 1991.

[7] S. P. Pogossian, L. Vescan, and A. Vonsovici, "The single-mode condition for semiconductor rib waveguides with large cross section," *J. Light. Technol.*, vol. 16, no. 10, pp. 1851–1853, 1998.

[8] G. T. Reed and A. P. Knights, *Silicon photonics : an introduction*. John Wiley, 2004.

[9] "LEP500 Etch Depth Monitor Real-time, in-situ plasma etch depth monitoring and end point control plus co-linear wafer vision system."

[10] W. Bogaerts *et al.*, "Silicon microring resonators," *Laser Photonics Rev.*, vol. 6, no. 1, pp. 47–73, 2012.

[11] M. L. Davenport, “Heterogeneous Silicon III-V Mode-Locked Lasers,” UCSB, 2017.

[12] B. J. Soller, D. K. Gifford, M. S. Wolfe, and M. E. Froggatt, “High resolution optical frequency domain reflectometry for characterization of components and assemblies.”

[13] D. Taillaert *et al.*, “An out-of-plane grating coupler for efficient butt-coupling between compact planar waveguides and single-mode fibers,” *IEEE J. Quantum Electron.*, 2002.

[14] T. Shoji, T. Tsuchizawa, and T. Watanabe, “Spot-size converter for low-loss coupling between 0.3-μm-square Si wire waveguides and single-mode fibers,” *Proc. LEOS 2002*, pp. 289–290, 2002.

[15] M. Tran, T. Komljenovic, J. Hulme, M. Davenport, and J. Bowers, “A Robust Method for Characterization of Optical Waveguides and Couplers,” *IEEE Photonics Technol. Lett.*, vol. PP, no. 99, pp. 1–1, 2016.

[16] M. L. Davenport, M. A. Tran, T. Komljenovic, and J. E. Bowers, “Heterogeneous Integration of III–V Lasers on Si by Bonding,” *Semicond. Semimetals*, vol. 99, pp. 139–188, Jan. 2018.

[17] T. Komljenovic, D. Huang, P. Pintus, M. A. Tran, M. L. Davenport, and J. E. Bowers, “Photonic Integrated Circuits Using Heterogeneous Integration on Silicon,” *Proc. IEEE*, pp. 1–12, 2018.

[18] Y. Zheng *et al.*, “Electrically pumped heterogeneously integrated Si/III-V evanescent lasers with micro-loop mirror reflector,” *Appl. Phys. Lett.*, 2011.

[19] M. Nakamura, A. Yariv, H. W. Yen, S. Somekh, and H. L. Garvin, “Optically pumped GaAs surface laser with corrugation feedback,” *Appl. Phys. Lett.*, vol. 22, no. 10, pp. 515–516, 1973.

[20] C. Zhang, S. Srinivasan, Y. Tang, M. J. R. Heck, M. L. Davenport, and J. E. Bowers, "Low threshold and high speed short cavity distributed feedback hybrid silicon lasers," *Opt. Express*, vol. 22, no. 9, p. 10202, 2014.

[21] C. T. Santis, Y. Vilenchik, N. Satyan, G. Rakuljic, and A. Yariv, "Quantum control of phase fluctuations in semiconductor lasers," *Proc. Natl. Acad. Sci.*, vol. 115, no. 34, pp. E7896–E7904, 2018.

[22] A. W. Fang, E. Lively, Y.-H. Kuo, D. Liang, and J. E. Bowers, "A distributed feedback silicon evanescent laser.," *Opt. Express*, vol. 16, no. 7, pp. 4413–4419, 2008.

[23] S. Srinivasan, A. W. Fang, D. Liang, J. Peters, B. Kaye, and J. E. Bowers, "Design of phase-shifted hybrid silicon distributed feedback lasers," *Opt. Express*, vol. 19, no. 10, p. 9255, 2011.

[24] L. Coldren, S. Corzine, and M. Mashanovitch, *Diode Lasers and Photonic Integrated Circuits*, 2nd ed. John Wiley and Sons, 2012.

[25] H. Park *et al.*, "A hybrid AlGaInAs-silicon evanescent waveguide photodetector," *Opt. Express*, vol. 15, no. 10, pp. 6044–6052, 2007.

[26] H. Ohe, H. Shimizu, and Y. Nakano, "InGaAlAs multiple-quantum-well optical phase modulators based on carrier depletion," *IEEE Photonics Technol. Lett.*, vol. 19, no. 22, pp. 1816–1818, 2007.

[27] H. Chen, S. Member, Y. Kuo, and J. E. Bowers, "A Hybrid Silicon – AlGaInAs Phase Modulator," vol. 20, no. 23, pp. 1920–1922, 2008.

Chapter 3. Kilohertz Linewidth Widely Tunable Lasers

Early generations of Si/III-V heterogeneously-integrated lasers featured linewidths typically in the range of 50-300 kHz, *e.g.* [1] and [2]. With the optimizations of silicon waveguides and III-V gain layer designs described in chapter 2 of this dissertation, and with new design using multiring mirrors, we have been able to further improve the linewidth by an order of magnitude, reaching down to several kHz Lorentzian linewidth level. This chapter presents the details of the laser designs, modeling and a complete characterization of dual-ring mirror based tunable lasers using the standard heterogeneous Si/III-V photonic platform.

3.1 Laser designs

A Si/III-V heterogeneous tunable laser can be considered as a photonic circuit, constructed with elements in the designed configuration. The circuit level design of the laser is shown in *Figure 3.1*. Main components to form the laser are listed below:

(a) *Front mirror (low reflective mirror)*: The front-side loop mirror formed by looping the two ports of a bent-straight coupler has a designed ~40-50% power reflectivity in the C+L optical bandwidth.

(b) *A single-sectioned optical amplifier Si/III-V waveguide (gain section)*: The rib waveguide is 231 nm etched from the 500 nm thick Si layer. The Si width in the amplifier is chosen to be 850 nm which balances out the low internal loss and high gain requirements for the laser. The length of this active element is set to be 1 mm.

(c) *Phase tuner*: A long metal (Ti/Pt) strip is deposited vertically on the top of the oxide cladding of the Si waveguide to form the microheater for phase tuning using thermo-refractive effect.

(d) *Dual-ring mirror*: The back-side mirror of the laser is a dual-ring mirror structure formed by a waveguide coupler and two ring resonators. This mirror is subjected to design variation and will be discussed more details in the sub-section.

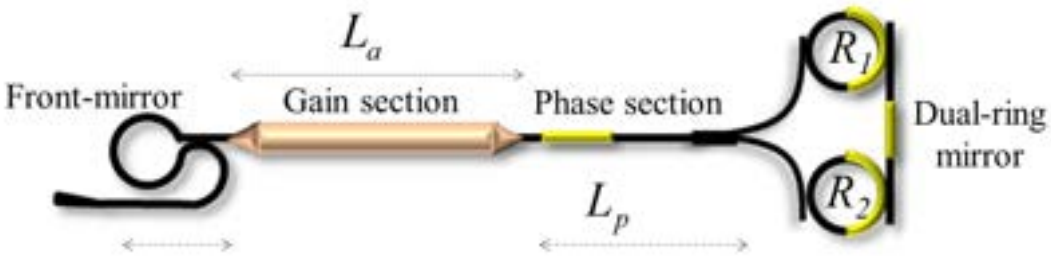

Figure 3.1 Schematic structure of a basic widely tunable Si/III-V laser based on multiring mirrors. The front-mirror is a loop mirror formed with a bent-straight coupler. Gain section is an optical amplifier heterogeneous Si/III-V waveguide, bridged to the Si passive waveguides via two Si/III-V tapers. The phase tuner is a microheater on the top cladding of the Si waveguide. The back-mirror is a multiring mirror with two ring resonators of radii R1 and R2 and 3-dB multimode interferometer (MMI) coupler. There are also microheaters on the ring resonators for tuning the resonances.

As component-level designs for most of the elements in the laser structure are already presented with details in Chapter 2 of this dissertation, the only key component design in this chapter is the dual-ring mirror.

3.1.1 *Dual-ring mirror*

Dual-ring mirror refers to a structure where two rings are cascaded in add-drop configuration within a loop mirror, as a generic schematic shown in *Figure* 3.2. The loop of the structures can be formed by a 2x2 or 1x2 waveguide couplers, whose coupling amplitude coefficient is represented by κ_c. In this work, we actually utilized a broadband 50% 1x2 multimode interference (MMI) coupler (*i.e.* $\kappa_c = 0.5$) to realize a highly reflective back mirror for the laser cavity. Within this loop, there are two ring resonators with slightly different radii to

shape the Vernier spectrum needed for wavelength tuning. The Vernier free spectral range (FSR) is determined by equation *(3.4)*, where FSR_m is FSR of the m^{th} ring.

$$FSR_{Vernier} = \frac{FSR_1 \cdot FSR_2}{|FSR_1 - FSR_2|} \qquad (3.4)$$

$$FSR_m = \frac{\lambda^2}{2\pi R_m n_g} \qquad (3.5)$$

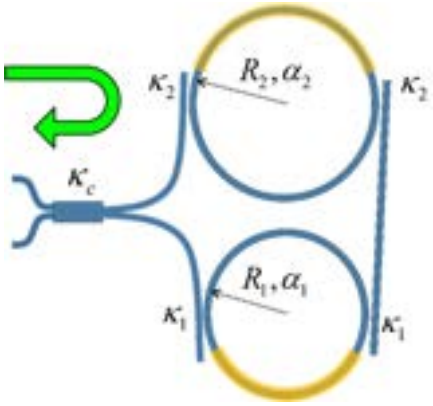

Figure 3.2 Generic configuration of a dual-ring mirror.

The bus-ring coupling ratios for each ring, ring radius and amplitude propagation loss constant are denoted by κ_m, R_m, α_m (m =1, 2). The spectral analysis is carried out using the equations for a generic multiring mirrors rigorously derived in Appendix 1. For a dual-ring mirror structure as shown in *Figure* 3.2 where the coupling ratios for add and drop are the same on each ring, the complex amplitude reflectivity of the mirror is given by the following equations:

$$r_{mirror} = -2j\sqrt{\left(1-\kappa_c^2\right)\kappa_c^2} \cdot t_{drop}\left(\kappa_1, \kappa_1, R_1, \alpha_p\right) \cdot t_{drop}\left(\kappa_2, \kappa_2, R_2, \alpha_p\right) \qquad (3.6)$$

$$t_{drop}\left(\kappa_m, \kappa_m, R_m, \alpha_p\right) = \frac{-\kappa_m^2 \left(2\pi R_m \alpha_p\right)^{1/2} e^{j2\pi R_m \beta_p/2}}{1-\left(1-\kappa_m^2\right) 2\pi R_m \alpha_p e^{j2\pi R_m \beta_p}} \qquad (3.7)$$

where α_p and β_p are respectively the waveguide electric field propagation loss and the effective propagation constant in the silicon waveguide, and the subscript *m* takes value 1 and 2 for the two rings.

In this work, the add-drop ring resonators are implemented in the simplest possible layout: a circular ring placed in vicinity of two straight bus waveguides. The coupling between the ring and bus waveguide is dependent on the ring radius (R), the width of the ring (w_R) and the bus (w_B), and the gap (G) between them, as illustrated in *Figure 3.3*. Once other parameters are chosen, only a single parameter the gap (G) needs to be changed to control the coupling coefficient.

The first requirement for the design of the waveguide resonator to achieve stable lasing is the single (transversal) mode guiding. This requirement sets an upper bound for the waveguide width to be about 800 nm from the mode analysis in Chapter 2. Larger waveguides have lower propagation loss but would also require smaller gap to achieve the same coupling coefficient. Therefore, we have chosen 650 nm for the ring resonators in this work for relatively strong coupling with reasonably large gap. At this width, the waveguide loss is approximately 1 dB/cm (see Chapter 2).

For the ring radii, the bending loss of the waveguides in the ring resonators automatically determine the lower-bound value. To guarantee a safe margin (10 μm) from the simulated minimum radius mentioned in Chapter 2, we choose the ring radii to be larger than 60 μm. This safe margin is also to prevent any catastrophic increase of the bending loss due to fabrication variations, *e.g.* variation in the refractive index of the oxide film, and deviation from a 90° verticality of the etched waveguide sidewall.

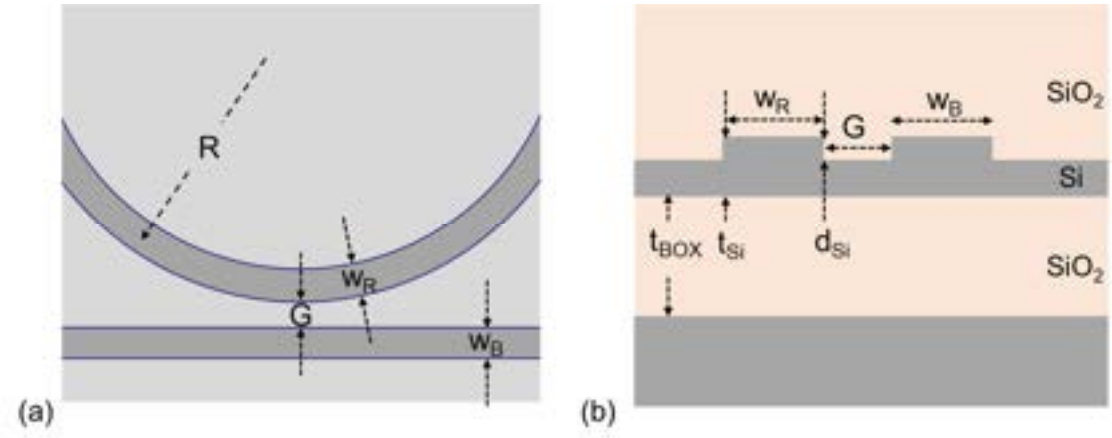

Figure 3.3 Ring resonator coupler structure and the cross-section at the coupling region.

The power coupling coefficient of the ring-bus coupler with sweeping parameters is computed using a coupled-mode-theory (CMT) commercial simulation tool. Some key results are then verified to reasonably agree with finite-difference-time-domain (FDTD) simulation results obtained with a commercial FDTD software. The simulated power coupling coefficient versus the gap for 650 nm wide waveguide width (w_R=w_B=650 nm) with different ring radii (ranging from 40 to 150 μm) is plotted in *Figure 3.4*. At the same gap, larger radius results in larger power coupling as the modes in the ring and the bus waveguide have a longer interaction length.

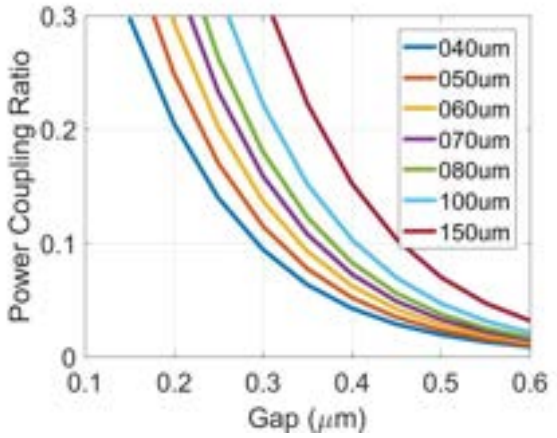

Figure 3.4 Dependence of the power coupling coefficient on the gap between the ring and the bus waveguide with varying ring radii. The ring and bus waveguides are both 650 nm wide.

Considering all the aforementioned factors, the ring radii of the two rings were chosen 60.0 μm and 62.5 μm for a ~40 nm wide Vernier free spectral range (FSR) in C+L band. The spectral responses of the dual-ring mirror reflection with ring-bus power coupling ratios $\kappa_1 = \kappa_2 = 0.125$ are calculated using *(3.6)* and *(3.7)*, and plotted in *Figure 3.5*. *Figure 3.5(a)* shows the individual spectra of the rings with several-nm FSR, and *Figure 3.5(b)* of the synthesized spectral response by the dual-ring mirror shows a much broader FSR. This Vernier FSR sets the range for the wavelength tuning of our lasers.

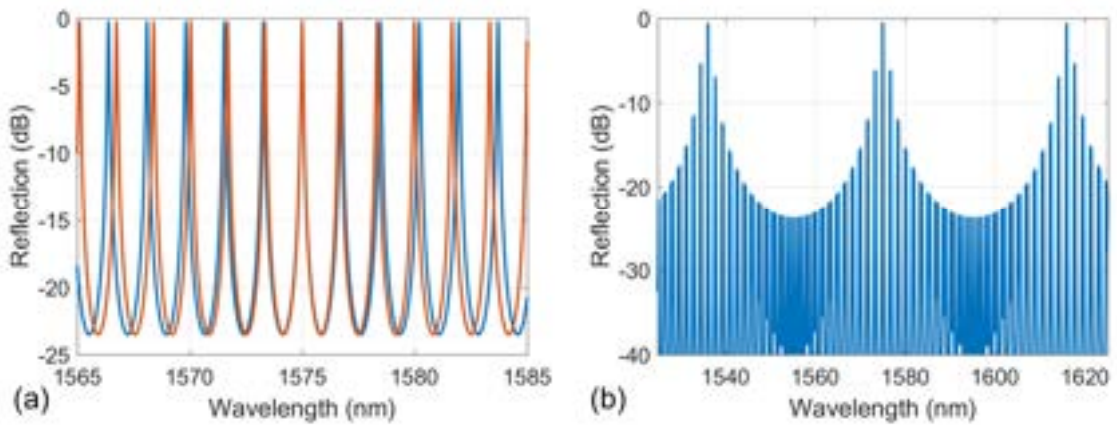

Figure 3.5 (a) Reflection spectra of individual rings (b) Combined spectrum of the dual-ring mirror. Dispersion is neglected for simplicity.

A key advantage in the rings-based mirror is the effective cavity length enhancement effect. Near ring resonances, the photon circulates multiple times inside the rings and retain longer lifetime compared to that when it is off-resonance. Once normalized by the waveguide group index, the laser effective cavity length appears to be enhanced near resonances as illustrated in *Figure 3.6(a)* where the calculation was done in the case of $\kappa_1 = \kappa_2 = 0.125$, passive routing waveguide length L_p = 1 mm and active length L_a = 1 mm. Two small ring of 60s μm occupies

a small fraction of the laser footprint but provides more than 60% the length of the total cavity length.

However, the corresponding longitudinal modes also has a non-uniform spacing (shown in *Figure 3.6(b)*). Near the resonance, the mode spacing is reduced proportionally to the cavity length enhancement. One should keep this in mind when designing stable single frequency lasers.

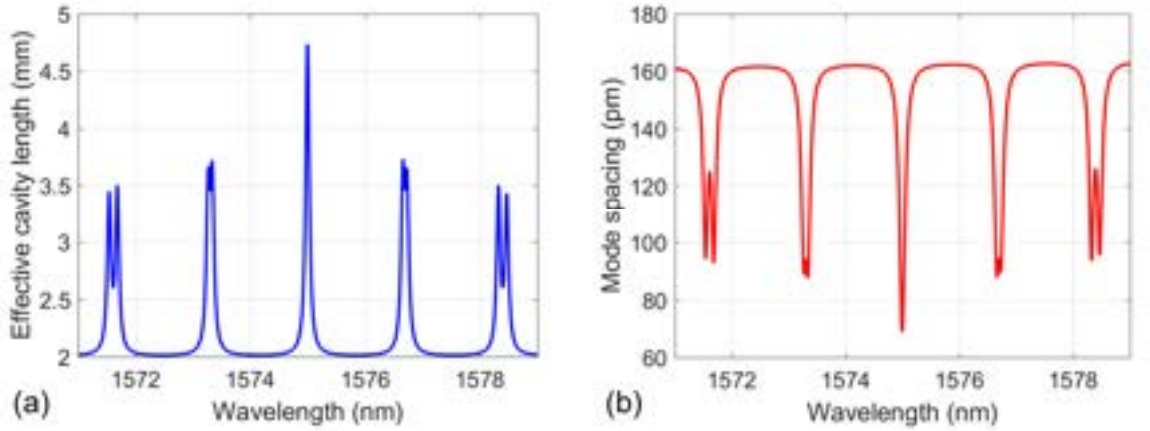

Figure 3.6 Calculation results for (a) effective cavity length versus wavelength showing 2.5x enhancement at the resonance (b) mode spacing from its nearest neighbor mode, reduced by 2.5x at the resonance. The calculation is with ring-bus power coupling ratio of 12.5%.

3.1.2 *Laser modeling*

We approximate our lasers as two-section lasers. As shown in *Figure 3.7(b),* the gain section (formed by heterogeneous Si/III-V waveguide) and the front (low reflection) mirror can be lumped into a single active section on the left-hand-side with the reflection coefficient r_1. The phase section and all the silicon waveguides used for routing are lumped into the passive section, connecting to the ring mirror on the right-hand-side. Due to the low reflection on the heterogeneous taper from III-V to silicon [3], we neglect reflection on the active-passive transition in our analysis.

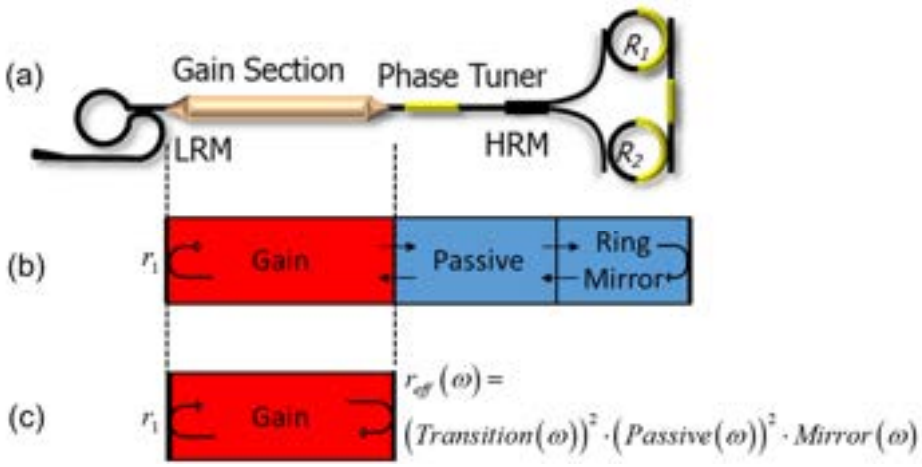

Figure 3.7 Modeling of the dual-ring mirror laser for steady-state analysis (a) Schematic of the laser (b) Block diagram representation of the laser sections (c) Equivalent cavity with effective mirror to model the extended passive sections.

Next, we replace all the passive sections on the *Figure 3.7(b)* by an effective mirror with complex wavelength dependence represented by $r_{eff}(\omega)$. This substitution is valid since we are looking for steady-state solutions in this analysis [4]. The effective reflectivity is the product of transfer functions of all passive parts and the active-passive transition, given by equation *(3.8)*.

$$r_{eff}(\omega) = t^2_{transition}(\omega) \cdot t^2_{passive}(\omega) \cdot r_{mirror}(\omega) \qquad (3.8)$$

Here, $t_{transition}(\omega)$ is simply an attenuation constant representing the transmission loss at the active-passive transition, which is equivalent to -1 dB (or ~80%) on average over the C+L bands accounting for two tapers on both ends of the Si/III-V amplifier waveguide. For a total length L_p of about 1 mm accounted for all passive waveguide routing and phase section, the transfer function for the passive waveguides is given by equation *(3.9)*, where α_p and β_p are respectively the waveguide electric field propagation loss and the effective propagation constant in the silicon waveguide:

$$t_{passive}(\omega) = \exp\left(-\alpha_p L_p - j\beta_p L_p\right) \qquad (3.9)$$

The last term for the dual-ring mirror reflection $r_{mirror}(\omega)$ has been expressed in *(3.6)* previously. In the next sections, we use these formulations to explore the design space of laser parameters.

3.1.3 *Laser spectral linewidth*

To study the laser linewidth, we use the formalism carried out by Patzak et al. in [5] and Kazarinov and Henry in [6]. Due to the frequency dependence of the phase and reflectivity of the extended passive section, as we saw in equation *(3.8)* and *(3.6)* and *Figure 3.5(c)*, the linewidth of the otherwise solitary Fabry-Perot laser is reduced by a factor F^2 where $F = 1+A+B$. Analytical calculation of the Lorentzian linewidth of our laser is carried out following the equations below:

$$\Delta\nu = \frac{\Delta\nu_0}{F^2} = \frac{\Delta\nu_0}{(1+A+B)^2} \qquad (3.10)$$

$$A = \frac{1}{\tau_0}\mathrm{Re}\left\{ j\frac{d\ln r_{eff}(\omega)}{d\omega}\right\} = \frac{1}{\tau_0}\frac{d\varphi_{eff}}{d\omega} \qquad (3.11)$$

$$B = -\frac{\alpha_H}{\tau_0}\mathrm{Im}\left\{ j\frac{d\ln r_{eff}(\omega)}{d\omega}\right\} = \frac{\alpha_H}{\tau_0}\frac{d\ln\left|r_{eff}(\omega)\right|}{d\omega} \qquad (3.12)$$

$$\Delta\nu_0 = \frac{1}{4\pi}\frac{v_g h\nu n_{sp}\alpha_{tot}\alpha_m}{P_0\left[1+\dfrac{r_1}{\left|r_{eff}(\omega)\right|}\dfrac{1-\left|r_{eff}(\omega)\right|^2}{1-r_1^2}\right]}\left(1+\alpha_H^2\right) \qquad (3.13)$$

In equations *(3.11)* and *(3.12)*, the effective mirror term $r_{eff}(\omega)$ is separated into effective amplitude and phase parts as $r_{eff}(\omega) = \left|r_{eff}(\omega)\right|\exp\left(-j\varphi(\omega)\right)$. The real part, amplitude factor

$r_0(\omega)$, represents the field feedback from the extended passive section to the gain section. $\tau_0 = \frac{2n_g L_a}{c}$ is the photon round-trip time in the active section. In equation *(3.10)*, $\Delta\nu_0$ represents the Schawlow-Townes linewidth of a solitary Fabry-Perot diode laser with mirror reflectivities r_1 and $\left|r_{eff}(\omega)\right|$. As output power P_0 from the laser is collected on the low reflective side (r_1), the equation for $\Delta\nu_0$ is given by *(3.13)* where v_g is the group effective index, h is the Planck constant, ν is the lasing frequency, n_{sp} is the spontaneous emission factor, $\alpha_{tot} = \alpha_i + \alpha_m$ is the total loss, $\alpha_m = -\frac{1}{L_a}\ln\left(r_1\left|r_{eff}(\omega)\right|\right)$ is the mirror loss and α_i is the internal loss of the active section.

Now, let us discuss the physical meanings of these factors and equations, to help the readers grasp a good intuitive understanding of the mechanisms for linewidth narrowing phenomena involved.

First, the factor *A* reflects the increase in roundtrip accumulated phase – equivalent to the effective cavity length enhancement (mentioned in the previous section), mainly provided by the ring resonances in our case. An increase in the factor *A* means the passive length of the laser cavity becomes longer, hence the volume occupied by photon in the laser cavity is effectively enlarged. In contrast, the carrier occupied volume *i.e.* volume of active layer typically quantum wells or quantum dots, is constant. The ratio between the total carrier volume to the total photon volume is defined as *confinement factor* parameter. By enlarging the total photon volume via an increase in *A* using extended cavity, we basically lower the net confinement factor by reducing the confinement factor in the longitudinal direction (length along the cavity), as illustrated in *Figure* 3.8 *(a1)*. Since spontaneous emission events only

happen within the carrier occupied volume, lower confinement factor results in lower rate of a spontaneous emission coupling into the lasing mode, hence, lower noise. That is the so-call *noise dilution* mechanism for lowering the linewidth, here achieved by leveraging the magnitude of the factor *A*.

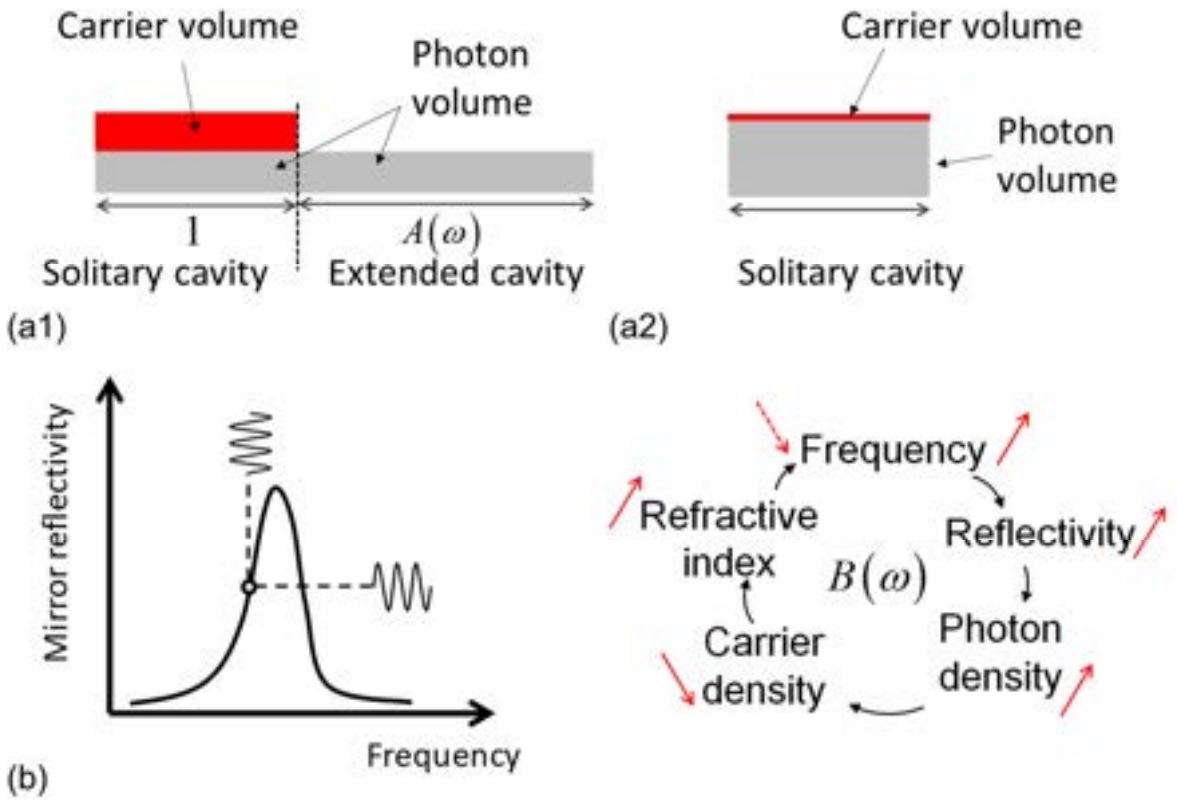

Figure 3.8 (a1) Illustration of the role of factor A in lowering laser confinement factor in longitudinal orientation (a2) Lowering the confinement factor on transversal orientation (b) Illustrative explanation of the detuned loading (or optical negative feedback) effect provided by a dispersive mirror.

It is worth noting that another effective design strategy is to lower net confinement factor in transversal orientation, as illustrated in *Figure* 3.8 *(a2)*. By lowering the physical volume of active layer (*e.g.* number of quantum-well layers) and/or lowering the optical mode confinement of the active layer to the transversal mode, ones can effectively reduce the net

confinement factor. In Si/III-V heterogeneous waveguide system, lowering the confinement factor also comes with the benefit of lower internal loss, as loss in silicon is typically much lower than III-V claddings. This allows ones to realize high Q resonator in a seemingly solitary cavity. Great results on this high coherent laser concept have been demonstrated by Santis et al [7], [8].

The factor B represents the magnitude of the optical negative feedback effect [6] (also known as detuned loading [9]), that helps stabilize the laser frequency via the phase-amplitude coupling of the lasing field – a unique phenomenon in semiconductor lasers characterized by the linewidth enhancement factor α_H . As illustrated in *Figure 3.8(b)* where the mirror reflectivity is a curve function of the optical frequency. When the lasing frequency is at the marked point (*i.e.* the positive slope side), an increase in laser frequency increases reflectivity (increasing photon density in the cavity), and hence decreases carrier density, which in turn causes the frequency to decrease, due to the carrier plasma effect. This negative feedback loop help stabilize the laser frequency, hence lower the laser frequency noise and linewidth. In contrast, if the lasing occurs on the other side of the mirror resonant peak (*i.e.* negative slope side), a positive feedback loop is formed with which frequency noise is amplified, therefore linewidth would be broadened.

Since the strength of the negative feedback effect is dependent on the strength of the coupling between carrier density and optical frequency via carrier plasma effect, factor B is proportional to the linewidth enhancement factor- α_H [10], the very factor that actually broadens the linewidth of the solitary laser. In other words, the detuned loading effect basically diminishes the role of factor α_H in the frequency noise of an extended cavity laser. This phenomenon makes integrated extended cavity lasers almost reliance-free on α_H ; that is a huge advantage

compared with solitary lasers in which the linewidth scales with $\left(1+\alpha_H^2\right)$. We could see this analytically by combine all equations from *(3.10)* to *(3.13)* to have Equation *(3.14)* below:

$$\Delta\nu = \frac{1}{4\pi}\frac{v_g h\nu n_{sp}\alpha_{tot}\alpha_m}{P_0\left[1+\frac{r_1}{\left|r_{eff}(\omega)\right|}\frac{1-\left|r_{eff}(\omega)\right|^2}{1-r_1^2}\right]}\frac{\left(1+\alpha_H^2\right)}{\left(1+\frac{\alpha_H}{\tau_0}\frac{d\ln\left|r_{eff}(\omega)\right|}{d\omega}+\frac{1}{\tau_0}\frac{d\varphi_{eff}}{d\omega}\right)^2} \qquad (3.14)$$

Table 3.1 List of parameters used for the laser design

Parameter	Symbol	Value	Unit
Wavelength	λ	1.575	μm
Planck constant	h	$6.62607004 \times 10^{-34}$	m^2kg / s
Light velocity	c	299792458	m/s
Optical frequency	ν	c / λ	Hz
Mode's group index	n_g	3.8	
Mode's group velocity	v_g	c / n_g	cm/s
Spontaneous emission factor	n_{sp}	1.5	
Linewidth enhancement factor	α_H	4	
Gain section internal loss	α_i	6	cm^{-1}
Si waveguide loss	α_p	1	dB/cm
III-V/Si taper loss	δ_{taper}^{dB}	0.5	dB
Gain length	L_a	1	mm
Routing waveguide total length	L_p	1	mm
Ring 1 radius	R_1	60	μm
Ring 2 radius	R_2	62.5	μm
Ring power coupling coefficient	$\kappa_1^2 = \kappa_2^2$	0.125	
Output Power	P_0	10	mW

All the values necessary for our calculations in all the equations from equation *(3.6)* to *(3.13)* are listed in *Table 3.1*. The estimated values of the three parameters A, B, F as functions of frequency detune from lasing wavelength (1575 nm) are shown in *Figure 3.9(a)*. Based on that, the Lorentzian linewidth is then estimated. The calculation result plotted in *Figure 3.9(b)* shows that at ring resonance, the linewidth is about 5 kHz. A slight detuning of the frequency to the lower side reduces the linewidth down to the minimum level of about 2 kHz.

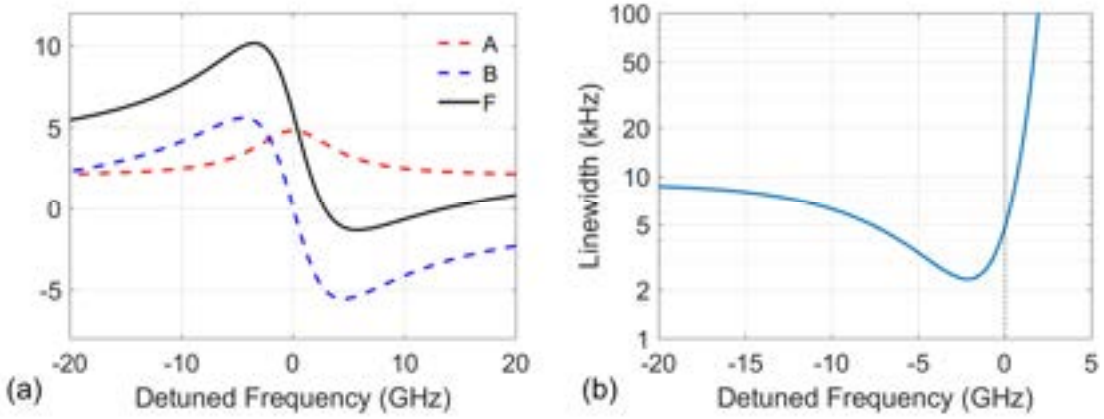

Figure 3.9 (a) Calculated values for coefficients A, B and F (a) estimated Lorentzian linewidth as functions of frequency detuned from the dual-ring mirror's resonance frequency assuming an output power of 10 mW. Values of parameters used for these calculations are listed in Table 2.2.

3.2 Laser fabrication

The designed laser is then fabricated in a standard Si/III-V heterogeneous process that is detailed in Appendix 3. Scanning electron microscopic images of the dual-ring mirror after silicon etching, a photo of the bonded wafer after InP substrate removal, and another SEM image of the Si/III-V taper after InP mesa etching are shown in *Figure 3.10(a-c).* To facilitate the testing and laser tuning, we deliberately tapped out a fraction of output power to a monitor photodiode with a broadband MMI coupler. A completed laser has a foot print of about

2.7×0.3 mm^2 as shown in *Figure 3.10(d)*. The facets of the lasers were mechanically polished to couple to a lensed fiber.

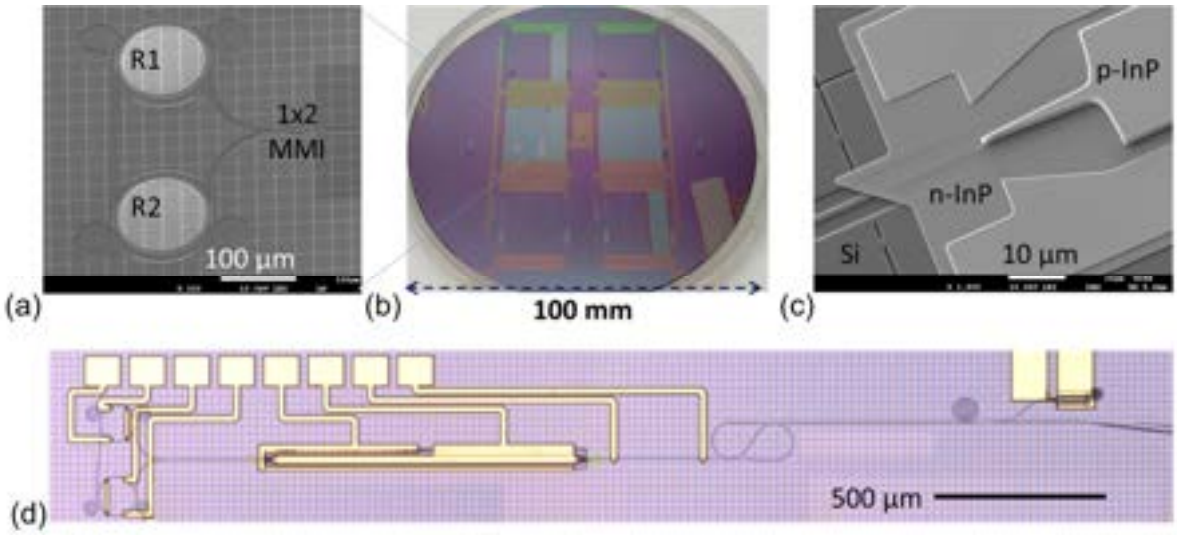

Figure 3.10 (a) An SEM image of the dual-ring mirror on silicon (b) The patterned SOI wafers with bonded InP materials after substrate removal (c) An SEM image of the Si/III-V taper for the active-passive transition (d) Microscopic image of the fabricated laser. A photodiode at the end of a tap-out coupler is used to monitor the output power from the laser and to assist the wavelength tuning.

3.3 Laser characterization

The laser was measured on a temperature-controlled stage set at 20°C. The output light is coupled into a 2.5 µm spot-size lensed fiber for characterization of spectral properties such as wavelength tuning, spectral linewidth and frequency noise. A Faraday based in-line optical isolator with larger than 50 dB extinction ratio was connected to the lenses fiber to eliminate any unintentional reflections towards the laser.

The light-current-voltage (L-I-V) curve of the laser was measured by ramping up the injection current while both phase tuners on both rings are off. For each current point, the phase section of the laser was tuned to maximize the output power based on the tap signal received at the

monitor photodiode. The responsivity of the photodiode on the tap coupler was calibrated using a large area external photodiode for accurate reading of the laser output. The plots shown in *Figure 3.11* shows a threshold current of about 33 mA. The lasing wavelength was stable at 1565 nm throughout this test.

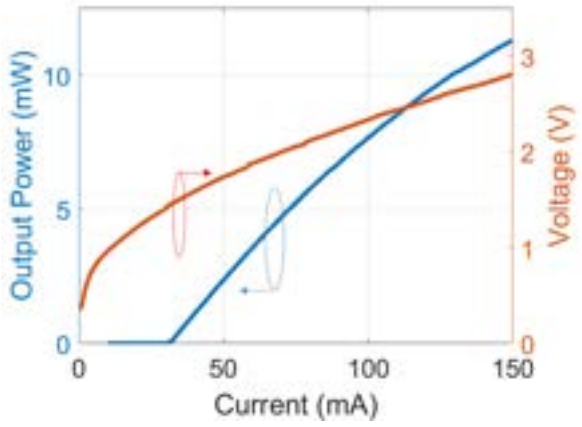

Figure 3.11 LIV curve of the dual-ring laser with lasing wavelength of 1565 nm.

3.3.1 *Wavelength tuning*

We characterized the laser wavelength tuning characteristics at a fixed injection current of 120 mA (~4x threshold current) to the gain section of the laser. The lasing spectra are acquired by a grating-based optical spectrum analyzer. An initial coarse tuning was done to acquire the lasing spectra across the tuning range, as shown in *Figure 3.12(a).* The spectra show stable single mode lasing across a ~40 nm tuning range. It can be seen that the side-mode suppression ratio (SMSR) over the full span is larger than 50 dB.

Next, a two-dimensional sweep of ring fine tunings is carried out to achieve the full tuning map for the laser. In our test procedure, the electrical powers applied to the heaters on top of two ring resonators are stepped by an even amount. For each operation point, the power applied to the heater on top of the 200 μm long phase section is optimized to achieve the

maximum output power indicated by the photocurrent read-out on the on-chip monitor photodiode (shown on the right-hand-side of *Figure 3.10(d)*). The measurement was automated with a computer program. The lasing wavelength at different pair values of heater powers on two rings are measured. A linear and smooth tuning map was obtained as shown in *Figure 3.12(b)*.

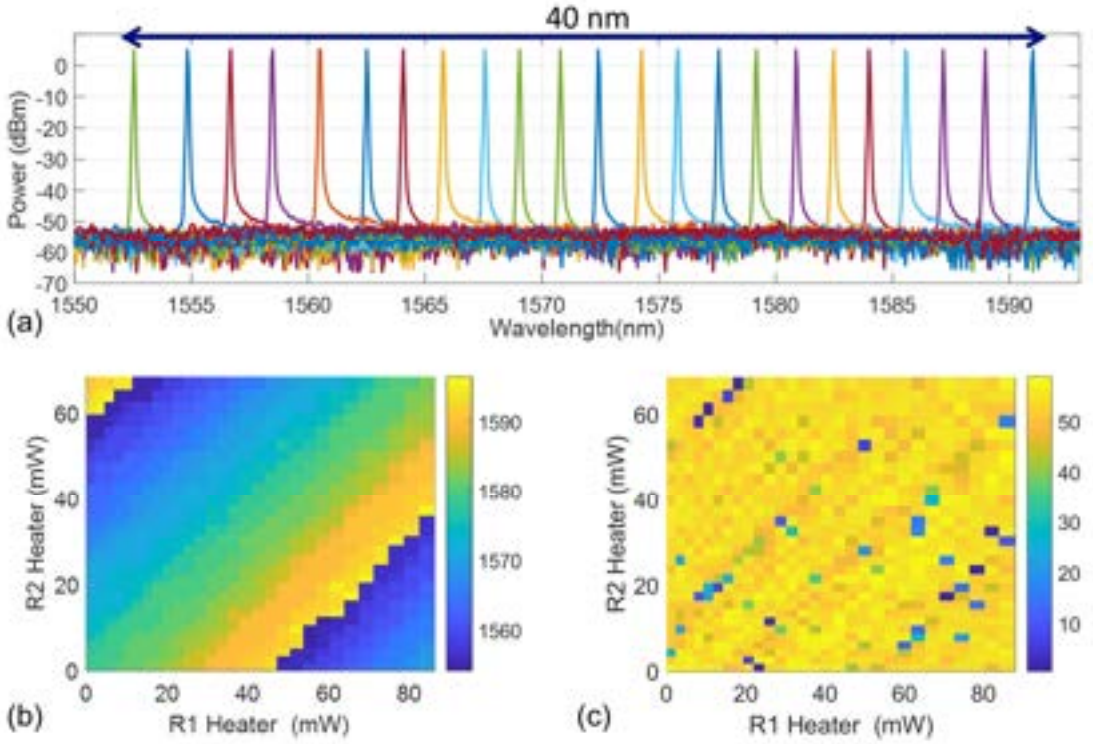

Figure 3.12 (a) Course tuning spectra showing the tuning range (b) Two-dimensional wavelength tuning map of the dual-ring mirror laser. The color indicates the lasing wavelength in unit of nm. (c) Side-mode suppression ratio (SMSR) of the corresponding wavelength tuning map. The color indicates the SMSR values in unit of dB.

The corresponding side-mode suppression ratio (SMSR) map is plotted in *Figure 3.12(c)*. SMSRs on almost all of lasing points are within the range 45 ~55 dB. The variation on the SMSR originates from how well the two ring spectra are aligned to each other at the pre-determined heater setpoints in the test. Some outlier operation points with very low SMSRs

correspond to multimode lasing that happens when the two ring spectra are far off from aligning, and two modes are able to rise equally. This is not a problem in the real operation where the two rings would be tuned in accordance to each other to achieve maximum lasing power at the any desired wavelength.

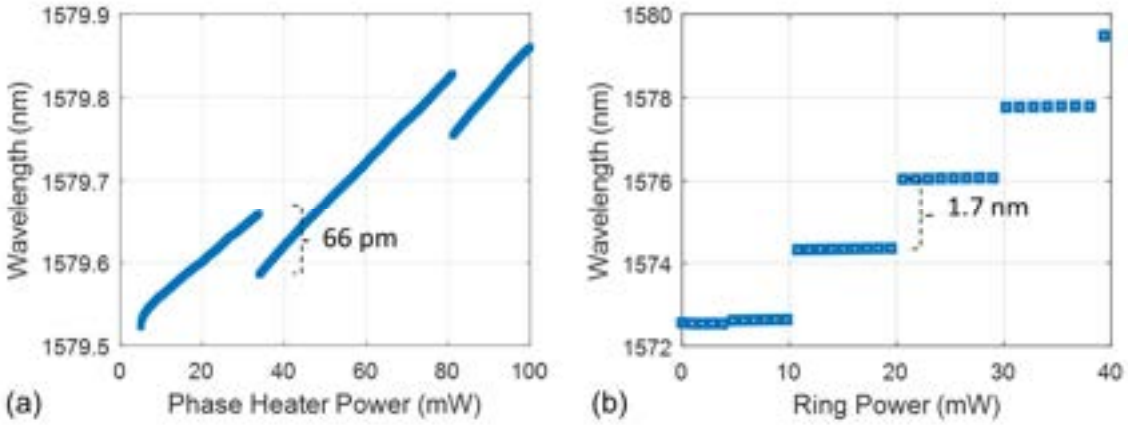

Figure 3.13 Mode hopping behavior in the tunable laser (a) Mode-hops between two adjacent longitudinal modes by tuning the phase section (b) Mode-hops between two ring's modes by tuning one of the ring resonators.

We took a closer look into the wavelength tuning characteristics of our laser in two tuning schemes: Fine tuning scheme is done using the heater on the phase section, and the coarse tuning scheme is done using the heaters on ring resonators. In *Figure 3.13(a)*, the lasing wavelength is continuously red-shifted when we ramped up the heater power to the phase section while keeping heaters on rings fixed. The continuous tune ranges about 0.25 nm before the lasing mode hops to the adjacent longitudinal mode on the blue side. The jump step is measured to be 66 pm, which well matches with the theoretical value shown earlier in *Figure 3.6(b)*. Furthermore, we can tune the ring resonators to achieve coarse tunability by stepping over the ring's individual resonances. The jump step of 1.7 nm measured here is exactly equal to the FSR of ring resonator of 60 μm radius shown in *Figure 3.6(a)*. The matching between

these two key parameters means the specifications (on the group index and the power coupling ratio of the ring-bus couplers) of fabricated devices are very close to the designed values.

3.3.2 *Frequency noise and Lorentzian linewidth*

All modeling and analysis on the laser linewidth regarded in the scope of this dissertation solely focus on the quantum noise limited Lorentzian linewidth (also known as *instantaneous linewidth*, or *fundamental linewidth*). Therefore, an accurate measurement of the laser's true Lorentzian linewidth is of paramount importance if we want to have relevant measured data to validate our theoretical analysis above. Unfortunately, the measurement with the commonly used delayed self-heterodyne method [11] suffers from the existence of colored noises, *e.g.* flicker noise (1/f) inherent to semiconductor devices, which effectively renders the shape of the beat note spectrum [12]. Furthermore, it is difficult to isolate the test setup from picking up the noises via electromagnetic interference, especially for unpackaged laser being tested in the lab environment. For these reasons, we characterized the Lorentzian linewidth of our laser by measuring its frequency noise spectrum, using commercial noise measurement systems provided by OEWaves [13]. The intrinsic linewidth, or Lorentzian linewidth of the laser can then be extracted by analyzing the frequency noise at higher frequencies where the measurement is relatively free from technical noise from electronics, vibrations, and other environmental factors.

Figure 3.14(a) shows a typical one-sided power spectral density of the laser frequency fluctuation as a function of frequency of the fabricated laser, taken at 120 mA pump current and slightly detuned from the peak resonance of 1576 nm wavelength. $1/f$ (flicker) and $1/f^2$ (random walk) frequency noises are dominant at the frequency range below 1 MHz. Also, some spikes corresponding to current source electronic noise and FM radio noise are also

observed. A white noise floor of $S_F(f) = 650$ Hz^2/Hz level starts to be seen at an offset frequency of 35 MHz. This white noise level corresponds to a modified Schawlow-Townes linewidth of $\pi S_F(f) = 2.1$ kHz [14].

Figure 3.14(b) plots the best linewidth measured when wavelength was tuned across the tuning range at the same pump current level. The linewidths are consistently about 2 kHz over the full span. This is close to the linewidth expected from our model (*Figure 3.9(b)*).

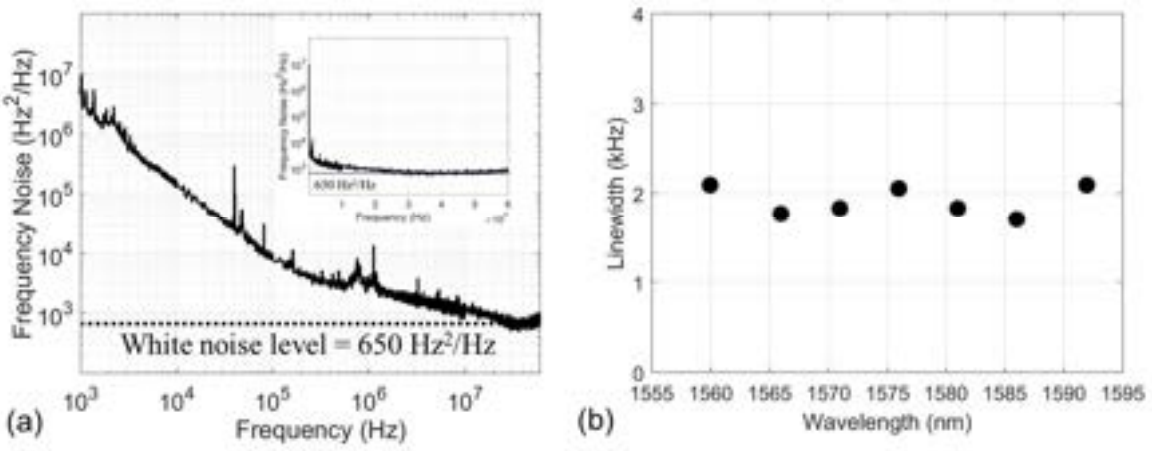

Figure 3.14 (a) Frequency noise spectrum of the fabricated dual-ring mirror laser measured at 120 mA. The inset replots the figure with frequency in linear scale to clearly show the white noise level (b) Best linewidth measured at wavelengths across the tuning range.

3.3.3 *Detuned loading (Optical negative feedback) effect*

One property of our laser that is worth re-emphasizing here is the fact that the lowest linewidth is achieved when the lasing frequency is detuned to the lower side of resonance, as discussed in laser simulation section, and shown in *Figure 3.9(b)*. Since the output power in our laser is collected at the front-mirror side, the highest output power is obtained when the reflectivity on the back-mirror is maximized. The output power's maximal operation point is, therefore, right at the resonance peak of the ring mirror. A direct implication of this for our laser

operation in practice is that, *the lowest linewidth operation point is not the same as the highest output power operation point*.

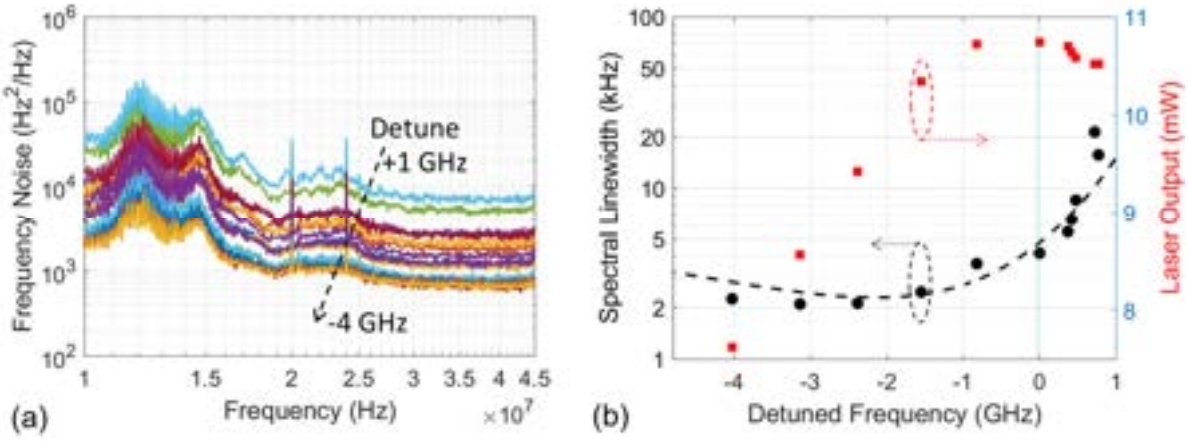

Figure 3.15 (a) Frequency noise spectra of the dual-ring mirror laser when the lasing frequency is detuned away from resonance peak (b) Laser output power and the extracted linewidth from frequency noise measurement as functions of the detuned frequency. The dash-line show the theoretical curve calculated in Figure 3.9(b).

This detuned loading effect has been observed as shown in *Figure 3.15*. The output power from our laser is split to two ports, one to a high resolution OSA (20 MHz resolution) and another to the laser noise measurement system, so that the lasing frequency and the frequency noise can be acquired simultaneously. At a fixed pump current of 120 mA to the gain, we first tune the two ring resonators and the phase section to obtain the maximum output power (assisted by the on-chip photodiode) so that lasing is now occurring at the peak of the ring mirror's reflection resonance spectrum. We then start to change power to the heater on the phase section to detune the lasing frequency from the resonance peak. As we detune the lasing frequency to the positive side (up to +1 GHz), the frequency noise of the laser rapidly increased significantly. In contrast, as we detune to the negative side (down to -4 GHz), the frequency gradually decreases to a certain point before starting to turn back. The frequency

noise spectra are plotted all together in *Figure 3.15(a)*. The extracted Lorentzian linewidths are plotted together with the output power as a function of the detuned frequency in *Figure 3.15(b)*. The detune frequency dependence of the measured Lorentzian linewidth matches quite well with the theoretical curve (the dash-line curve) that we calculated previously (*Figure 3.9(b)*). At zero detuning, the output power of the laser is maximized, and the linewidth is about 4 kHz, about two times the minimum achievable linewidth.

3.4 Summary

This chapter described the design, theoretical modeling, fabrication and characterization of a heterogeneously integrated Si/III-V laser using a dual-ring mirror. The fabricated laser exhibits a smooth and linear tuning behavior over a 40 nm range across the C and L bands. The Lorentzian linewidth, extracted from the frequency noise spectrum of the laser, was consistently about 2 kHz across the whole tuning span. The detune loading (or negative optical feedback) effect was predicted by the theoretical model and observed experimentally.

References

[1] S. Srinivasan, M. Davenport, T. Komljenovic, J. Hulme, D. T. Spencer, and J. E. Bowers, "Coupled-ring-resonator-mirror-based heterogeneous III-V silicon tunable laser," *IEEE Photonics J.*, vol. 7, no. 3, 2015.

[2] T. Komljenovic *et al.*, "Widely-Tunable Ring-Resonator Semiconductor Lasers," *Appl. Sci.*, vol. 7, no. 7, p. 732, 2017.

[3] M. L. Davenport, S. Skendzic, N. Volet, J. C. Hulme, M. J. R. Heck, and J. E. Bowers, "Heterogeneous Silicon/III–V Semiconductor Optical Amplifiers," *IEEE J. Sel. Top. Quantum Electron.*, vol. 22, no. 6, pp. 78–88, Nov. 2016.

[4] L. Coldren, S. Corzine, and M. Mashanovitch, *Diode Lasers and Photonic Integrated Circuits*, 2nd ed. John Wiley and Sons, 2012.

[5] E. Patzak, A. Sugimura, S. Saito, T. Mukai, and H. Olesen, "Semiconductor laser linewidth in optical feedback configurations," *Electron. Lett.*, vol. 19, no. 24, p. 1026, 1983.

[6] R. F. Kazarinov and C. H. Henry, "The Relation of Line Narrowing and Chirp Reduction Resulting from the Coupling of a Semiconductor Laser to a Passive Resonator," *IEEE J. Quantum Electron.*, vol. 23, no. 9, pp. 1401–1409, 1987.

[7] C. T. Santis, Y. Vilenchik, N. Satyan, G. Rakuljic, and A. Yariv, "Quantum control of phase fluctuations in semiconductor lasers," *Proc. Natl. Acad. Sci.*, vol. 115, no. 34, pp. E7896–E7904, 2018.

[8] C. T. Santis, S. T. Steger, Y. Vilenchik, A. Vasilyev, and A. Yariv, "High-coherence semiconductor lasers based on integral high-Q resonators in hybrid Si/III-V platforms," *Proc. Natl. Acad. Sci.*, vol. 111, no. 8, pp. 2879–2884, 2014.

[9] K. Vahala and A. Yariv, “Detuned loading in coupled cavity semiconductor lasers - Effect on quantum noise and dynamics,” *Appl. Phys. Lett.*, vol. 45, no. 5, pp. 501–503, 1984.

[10] M. Osinski and J. Buus, “Papers Linewidth Broadening Factor in Semiconductor Lasers-An Overview,” *Quantum*, no. l, 1987.

[11] T. Okoshi, K. Kikuchi, and A. Nakayama, “Novel method for high resolution measurement of laser output spectrum,” *Electron. Lett.*, vol. 16, no. 16, p. 630, 1980.

[12] L. B. Mercer, “1/f Frequency Noise Effects on Self-Heterodyne Linewidth Measurements,” *J. Light. Technol.*, vol. 9, no. 4, pp. 485–493, 1991.

[13] “HI-Q Optical TMS | OEwaves.” [Online]. Available: https://oewaves.com/hi-q-optical-tms. [Accessed: 13-Mar-2019].

[14] K. Kikuchi and T. Okoshi, “Estimation of Linewidth Enhancement Factor of AlGaAs Lasers by Correlation Measurement Between FM and AM Noises,” *IEEE J. Quantum Electron.*, vol. 21, no. 6, pp. 669–673, 1985.

Chapter 4. Ultralow Loss Silicon Waveguides

As described in the linewidth modeling section in chapter 2, the reduction in spectral linewidth of the extended cavity lasers is proportional to the square of the magnitude of the effective cavity length enhancement and optical negative feedback effect combined. Both effects are stronger with narrower (higher-Q) reflection resonance peak, which is equivalent to lower waveguide loss. Hence, lowering the waveguide loss is key to achieving lower laser linewidth. One order of magnitude improvement in waveguide loss would result in roughly two orders of magnitude reduction in linewidth, as shown in *Figure 4.1*.

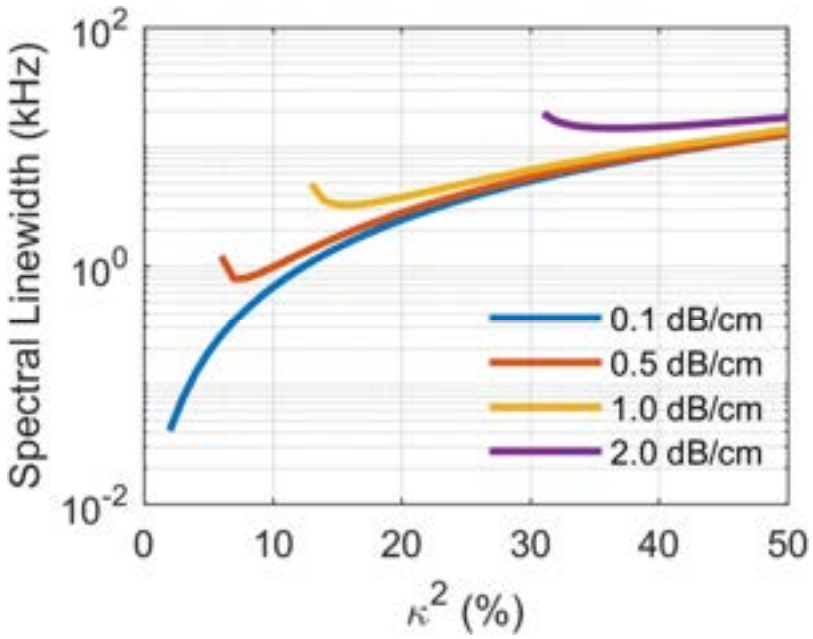

Figure 4.1 Simulated Lorentzian linewidth of widely-tunable laser as a function of coupling strength of the high-Q ring for four waveguide propagation loss scenarios. Calculation follows the analysis and parameters in [1]. © MDPI 2018

As a critical step on the path towards ultralow noise lasers, the work in this chapter sets the goal to achieve one order of magnitude in the reduction of the waveguide loss, from ~1 dB/cm (standard waveguides) down to ~0.1 dB/cm.

4.1 Ultralow loss silicon waveguide design

Due to the line-edge roughness associated with optical lithography, which is further aggravated in dry-etching processes, the propagation loss of the planar waveguides is typically dominated by the scattering loss induced by the interaction between the optical mode and the roughness on the waveguide sidewalls. Given the same materials, lithography and etching techniques, we can modify the waveguide geometry to lower the loss by having less interaction between the optical mode the waveguide sidewall. In the scope of this dissertation, we pursue the approach of making very shallow rib waveguides to achieve ultralow loss (ULL) performance. Reducing the etch depth of rib waveguides, most of mode electric field resides in the slab and only weakly interacts with the rib edges and the etched surfaces.

4.1.1 *Waveguide geometry*

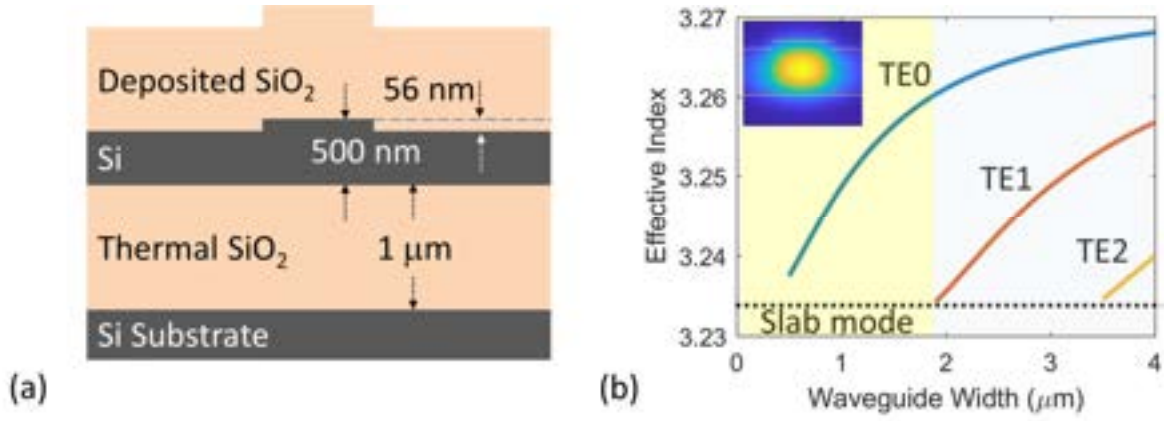

Figure 4.2 (a) Cross-sectional geometry of the ultra-low loss (ULL) Si waveguides. The 56 nm tall Si rib is formed by dry-etching, leaving a 444 nm thick Si slab. (b) Effective index versus waveguide width in the 56 nm rib Si waveguide. The waveguide is quasi-single mode within the yellow colored region. Inset: Electric field profile of the fundamental mode in 1.8 µm wide waveguide. © MDPI 2018

The ULL waveguide cross-sectional geometry is shown in *Figure 4.2(a)*. To lower the optical mode interaction with the rib sidewall, the waveguide rib height is targeted to be about 10% of the total Si layer thickness. An etch depth of 56 nm was chosen because it can be accurately controlled using a laser-based interferometric etch depth monitor (Intellemetrics LEP500) system, as shown in Chapter 2 Section 2.1.1. The effective index of the TE modes versus the waveguide width is calculated with a commercial mode solver and plotted in *Figure 4.2(b)*, suggesting that the waveguide guides a single TE mode when the width is 1.8 μm or lower.

We estimate the waveguide loss using the n_w model approximation, which is a simple model to implement [2]. This approximation is particularly useful if one only needs to quantify the relative comparisons of the propagation losses among different waveguide geometries under the same fabrication conditions. According to this model, waveguide loss can be approximated as

$$\alpha_r = A\left(\sigma, L_c, n_{eff}\right)\frac{\partial n_{eff}}{\partial w} \qquad (4.15)$$

where A is the proportionality factor determined by the sidewall roughness rms (σ) and the roughness correlation length (L_c), n_{eff} is the effective index of the waveguide optical mode, and w is the width of the waveguide. A full expression of A can be found in [3]. Given a waveguide geometry that is far from mode cut-off condition, the magnitude of the factor A in general does not depend on the waveguide width.

Figure 4.3(a) shows the measured propagation loss of the two different silicon waveguide geometries for the heterogeneous silicon platform used in previous works [4]–[6]. One is a fully 500 nm etched strip waveguide, and the other is 231 nm etched rib waveguide – the standard waveguide geometry for the Si/III-V heterogeneous integration platform. The widths of both waveguides are 1 μm. An empirical value of the parameters of the roughness

parameters were obtained (line edge roughness rms σ ~5 nm and correlation length L_c ~60 nm) and then equation *(4.15)* is used to generate theoretical curve corresponding to the radiative losses at varying etch depth. The theoretical waveguide loss curves with varying etching depths are then calculated and plotted in *Figure 4.3(b)*, showing a reasonable agreement with experimental data for the 500 nm and 231 nm etch depths. According to this model results, low propagation loss in the range of 3-10 dB/m can be expected for a much shallower - 56 nm - rib silicon waveguides if the width is larger than 1.5 µm.

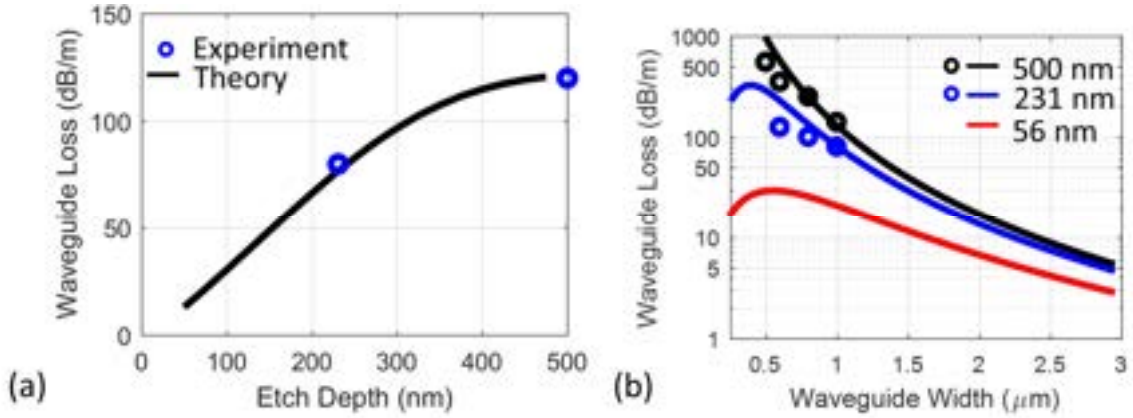

Figure 4.3 (a) Experimental data (circular markers) and theoretical curve (solid line) for the propagation loss of 1 µm wide waveguide at varying etch depth. (b) Theoretical calculations (solid lines) of the waveguide loss at varying waveguide width at three different etch depth (500 nm, 231 nm and 56 nm). The measured results are plotted in circular markers. © MDPI 2018

4.1.2 *Ultralow loss waveguide characterization*

The waveguide is fabricated using an oxide hard mask followed by a pseudo Bosch dry etching process as described in Appendix 3. The top cladding oxide is deposited using plasma-enhanced chemical vapor deposition (PECVD).

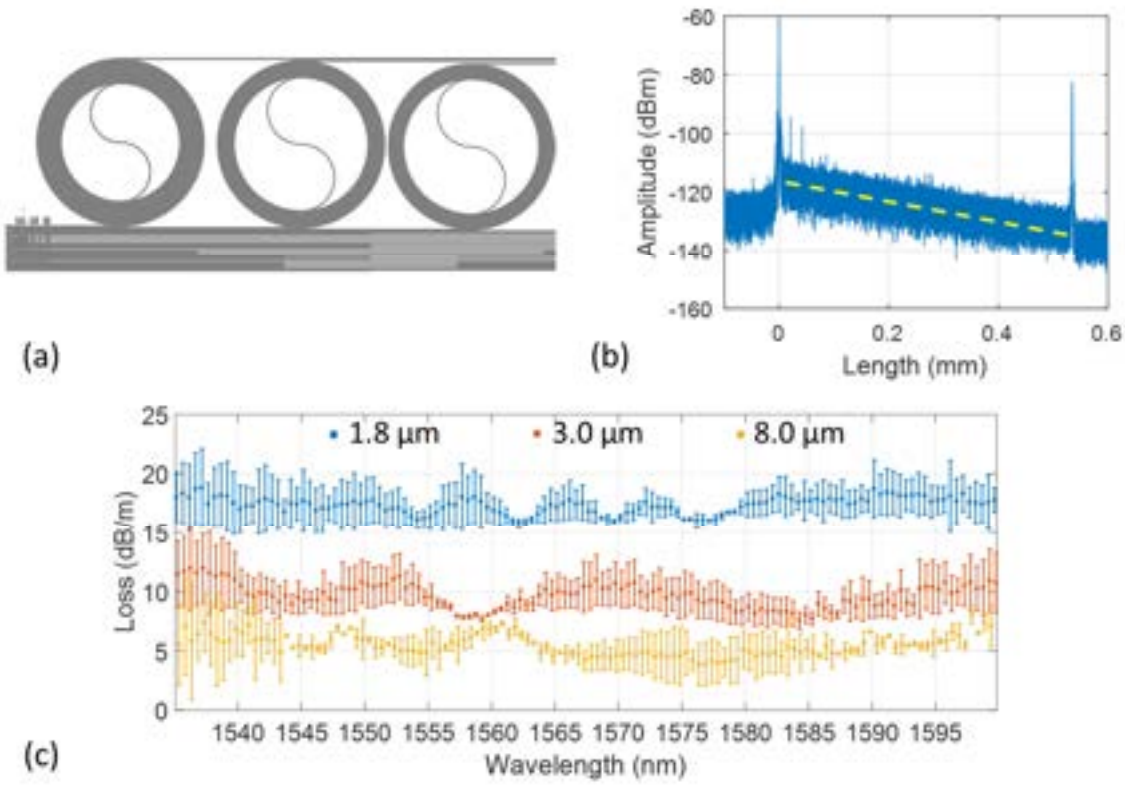

Figure 4.4 (a) Mask layout of spiral delay lines with 52.2 cm total length and 850 □m minimum bend radius (b) Optical Backscatter Reflectometry (OBR) data from the spiral with 1.8 µm width. A linear fit of the waveguide backscatter is shown with the dashed red line. The propagation loss of the waveguide can be approximated as 1/2 of the slope of the fitted line. (c) Wavelength dependence of the propagation loss (mean and standard deviation) of waveguides with different widths (1.8 µm, 3.0 µm and 8.0 µm). © MDPI 2018

We designed 52.2 cm long spiral delays illustrated in the *Figure 4.4(a)* to characterize the propagation loss. Waveguide widths were 1.8, 3.0 and 8.0 µm and the minimum bend radius used in all spirals was 800 µm. We, again, use the coherent optical frequency domain reflectometry (OFDR) technique with a commercially available system (Luna Inc. OBR 4400) [7] to quantify the propagation loss of the fabricated Si rib waveguides. The technique has been proven to calculate the propagation loss with high accuracy independent of the fiber-waveguide coupling loss uncertainty [8]. Figure 4.4*(b)* shows the data measured for the 52.2

cm long spiral of 1.8 μm wide ULL silicon waveguide. The peaks on the left-hand side (near 0 m distance) and right-hand side (near 0.5 m distance) are the reflections at the waveguide facets. The linearity of the trace verifies that the waveguide loss is not bend-loss limited. The measured mean and deviation of spectral dependence of the propagation loss of the three waveguide widths are plotted in *Figure 4.4(c)*. A single mode 1.8 μm wide waveguide achieves an average of 16 dB/m propagation loss over the C+L band. The propagation loss in multimode ULL waveguide with 3.0 μm and 8.0 μm widths are lower, at 10 dB/m and 4 dB/m respectively.

The measured loss of the ULL waveguides show a relatively large discrepancy to the values predicted by the n_w approximation method described in Section 2.2 (*Figure 4.4(b)*). The model made several simplifications such as ignoring the surface roughness of the etched slab surfaces. For fully etched (500 nm) or halfway etched (231 nm) waveguides, the optical field that interacts with the etched surface is small enough to be neglected in the total loss calculation. However, with the very shallow rib (56 nm) waveguides the optical field expands laterally (similar to a slab mode) and the interaction between the mode field and the etched surface cannot be ignored. The roughness rms of the etched surface is typically on order of several nanometers, which is more than one order of magnitude larger than the unetched waveguide top surface roughness (~0.1 nm). The scattering due to the etched surface roughness is significant and results in the discrepancy between the experimental and theoretical waveguide loss.

4.2 Ultralow loss passive component demonstrations

We utilize these ULL silicon waveguides to successfully demonstrate high quality-factor (Q) ring resonators and low kappa (κ), narrow bandwidth Bragg grating reflectors with record performance for sub-micron SOI waveguides.

4.2.1 *High quality-factor ring resonators*

One key component made possible by low-loss waveguides is the high-Q ring resonator. Ring resonators are an essential building block to realize compact optical filters and delays on chip. Higher Q-factors enable sharper, narrowband filters and longer delays, which are requirements for the aforementioned ultra-long laser cavity. There has been a plethora of recent work to demonstrate high-Q integrated resonators using different materials and cavity geometries. These results include fully integrated resonators with an intrinsic Q of 22 million in silicon [9], 81 million in a silicon nitride resonator [10] and over 200 million in a silica resonator [11]. However, the latter two results are multimoded, which can lead to multiple sets of resonances or excess loss at the coupling regions unless special care is taken to optimize the coupler [12]. These three results all have bend radii > 2mm, which limits the compactness of the device and complicates the design of a Vernier-effect filter due to the small free spectral range of each ring. Finally, it is unlikely that these resonators were designed with laser integration in mind, and cannot be integrated with the heterogeneous silicon/III-V laser without significant extra processing [13], [14].

In this work, we demonstrate ring resonators readily integrable with the heterogenous silicon/III-V platform with a loaded Q of 2.1 million, and an intrinsic Q of 4.1 million. The ring is in an all-pass configuration, and is 1.8 microns in width, which is single-mode for the TE polarization. The ring is connected to a bus waveguide of the same dimensions using a

straight-to-curved coupler with a 1.2 micron coupling gap. The transmission spectra of the ring are measured by sweeping a high-resolution tunable laser (0.1 pm steps) across the resonance and measuring the output power. The resulting spectra is depicted in Figure 4.5*(a)* and fitted with a Lorentzian function. The measured full width half max (FWHM) is 91.3MHz.

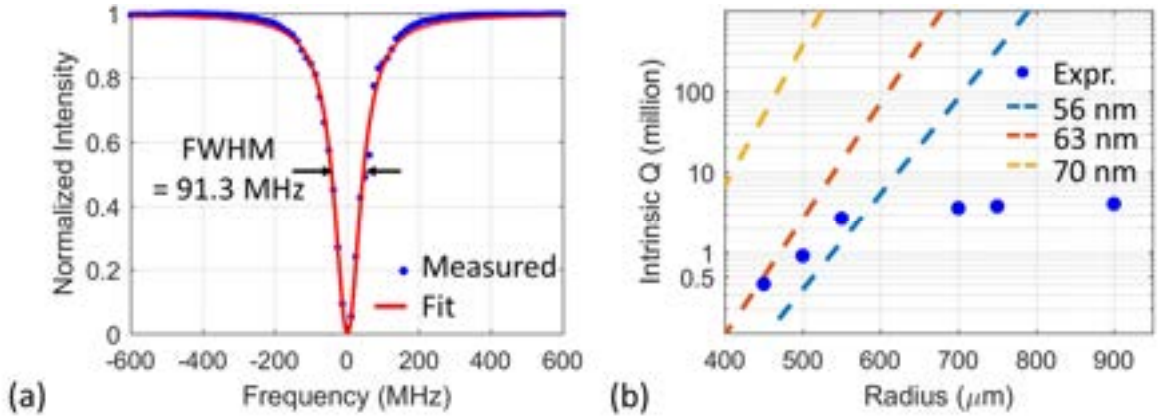

Figure 4.5. (a) Measured spectral responses of the 750 μm radius Si ring resonator (all-pass configuration) plotted with a Lorentzian fit. The extracted intrinsic quality factor Q_{int} = 4.1 million. (b) Simulated bend-loss limited intrinsic Q of the rings versus ring radius at three etch depths. The experimental data of the targeted 56 nm etch depth are depicted as blue circular markers. © MDPI 2018

The ring in *Figure 4.5(a)* has a 750 μm bend radius, for which we did not observe any bend-loss induced radiation in the resonator. To confirm this, we investigated rings with varying radii, and plot their intrinsic Q factor alongside the theoretical bend-loss limit for Q in Figure 4.5*(b)*. The experimental results are extracted from the measured FWHM, while the dashed lines are simulated using a commercial mode solver. The simulations are shown for three different etch depths, as that is the most sensitive parameter to the bend-loss. We find that our ring in this experiment is a bit over etched compared the target 56 nm, judging by the Q of the smaller rings. We do not observe significant bend loss in the rings until the radius is less than

550 mm. For practical reasons, the ring radius should be larger than 600 mm to avoid bend-loss possibly caused by an underetch of the waveguide.

4.2.2 *Narrow bandwidth Bragg gratings*

Another useful component that can be realized with low-loss waveguides is a low-kappa (κ) Bragg grating. These gratings are widely used in filters, sensors, and semiconductor lasers as a wavelength selective element, much like the ring resonator. The bandwidth of the grating is directly proportional to power coupling coefficient κ, and therefore can be minimized by reducing the perturbation strength of the grating [15]. At the same time, the length (L) of the grating should be long enough (κL ~ 1) and the loss of the waveguide must be low in order to obtain sufficient reflection. Care must be taken in the design of the grating in order to achieve weak κ as conventional sidewall or top surface gratings tend to have stronger κ. Instead, we utilize "post" (or inversely, "hole") gratings in which small areas of the waveguiding material are placed (removed) periodically on either side of the waveguide. The dimensions of the posts (holes) and proximity to the waveguide can be lithographically defined and tailored to achieve the desired κ. This approach has been successful for low loss silicon nitride gratings [16]. For our waveguides, it is simpler to etch holes on either side of the waveguide, as shown in *Figure 4.6(a)*. The resulting κ of the grating is directly controlled by the hole-to-waveguide distance, while the period of the grating is set to be 240 nm, corresponding to a stopband at 1563 nm for an unperturbed waveguide $n_{eff} = 3.2560$.

We fabricate uniform gratings with lengths of 0.5 and 1.0 cm. The waveguide width is 1.8 μm, and the length is 2.2 cm. We used an e-beam lithography to write the grating teeth, although DUV immersion lithography can also resolve 120 nm features. Transmission and reflection spectra are measured and fitted using transfer matrix modeling. This approach also

accounts for Fabry-Perot cavities formed by the waveguide facets, which affects the grating shape. From this, we extract the bandwidth and peak reflectivity of the grating, which can then be used to estimate κ. A few selected gratings are depicted in *Figure 4.6(b)* along with the predicted grating bandwidth. Using 1 cm long gratings, we were able to achieve a 50 pm FWHM bandwidth with roughly 70% reflectivity, with potential to further reduce the bandwidth with a longer grating.

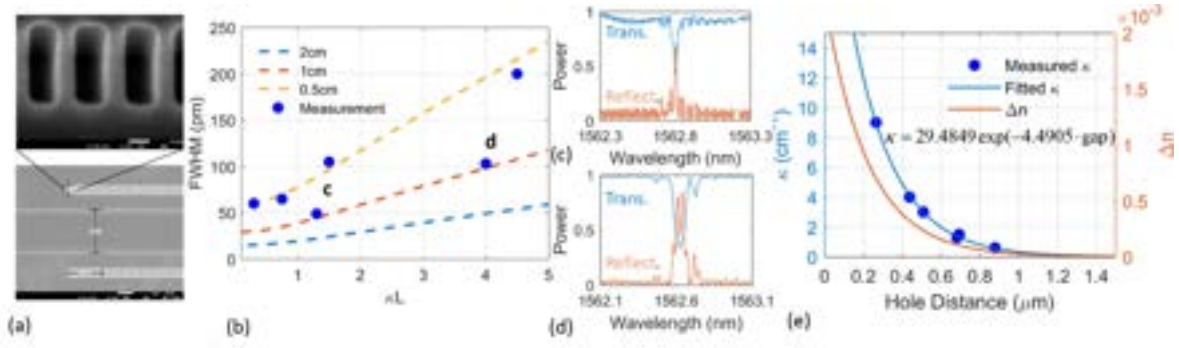

Figure 4.6 (a) An SEM image of the fabricated low κ Bragg grating waveguide with a close-up of the holes on both sides of the waveguide. (b) Theoretical calculations of gratings' full width half max (FWHM) versus varying κL for 0.5, 1 and 2 cm long grating waveguides. Circular blue markers show the measured data. (c-d) Spectra of reflection and transmission of 1 cm long grating waveguides with κ=1.25 cm^{-1} and κ=4.0 cm^{-1}, respectively. The ripples are caused by reflections off the waveguide facets. (e) The extracted κ, Δn, and exponential fit as a function of waveguide to hole distance. © MDPI 2018

4.3 Bridging ultralow loss to standard silicon waveguides

A low loss taper to transition from ULL waveguides to a waveguide geometry with smaller bend radius is the key for adding the ultralow loss passive devices into the heterogeneous Si/III-V platform. This allows us to basically expand the versatility of the heterogeneous silicon platform and, most importantly in the scope of this dissertation, allows for lowering the frequency noise of the lasers by orders of magnitude.

Figure 4.7 shows the schematic of an adiabatic taper for a low loss, low reflection transition of the optical mode from the 56 nm etched rib ULL waveguide to the standard 231 nm etched rib waveguide, which has a smaller critical bend radius (40 μm). The waveguide width is set at 1.8 μm. The mode transition happens along the linear taper formed by etching on the Si slab. *Figure 4.7 (a-c)* shows the simulated profiles of the waveguide's fundamental mode at points a, b and c denoted on the schematic figure.

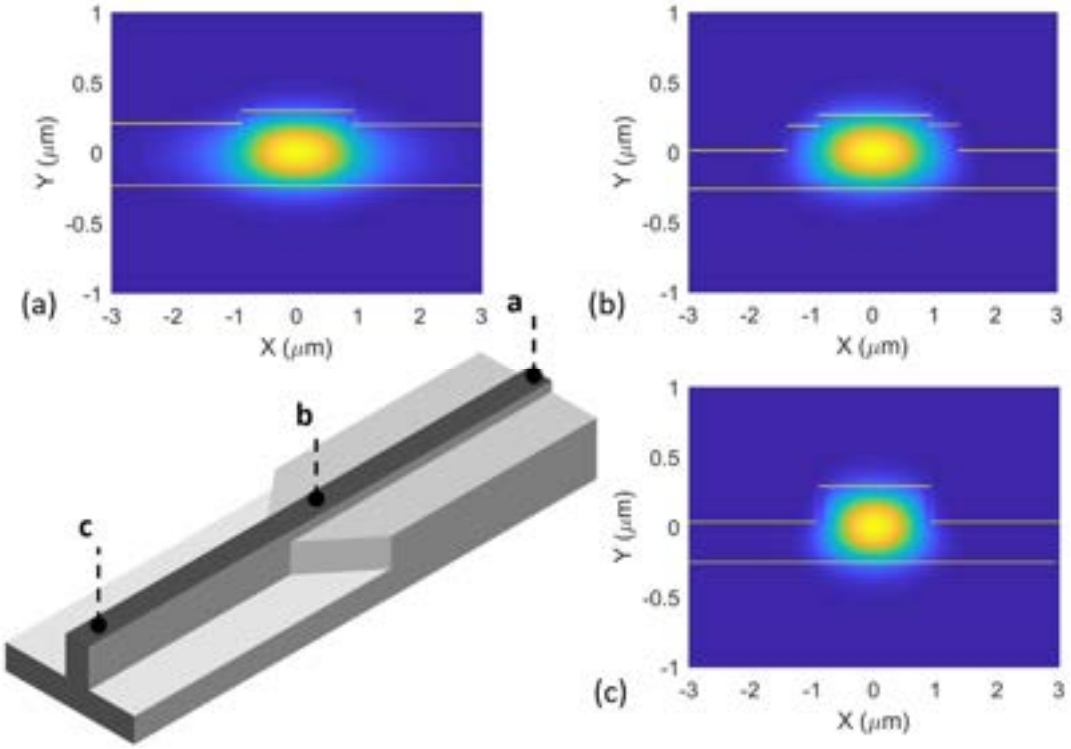

Figure 4.7 Schematic of the taper converting the optical mode from an ULL waveguide to standard rib (231 nm etch-depth) waveguide. Figures (a), (b) and (c) show the waveguide mode profiles at locations labeled a – ULL silicon waveguide, b – central part of the taper, and c - standard silicon waveguide along the taper structure. © MDPI 2018

In order to ensure an adiabatic transition from fundamental mode of the 56 nm etched waveguide to the 231 nm etched waveguide, the length of the linear taper must be sufficiently long. As shown in *Figure 4.8(a)*, at 1550 nm wavelength, high order modes in the deeper rib

waveguide are excited if the taper length is shorter than 25 μm. With a taper longer than 50 μm, both mode expansion and FDTD simulations show that essentially 100% transmission in the fundamental mode is achieved. The reflection power is also simulated and is shown to be lower than -60 dB level. To be safe, the taper length of 200 μm is chosen in practice. The wavelength dependence of the transmission efficiency and reflection power are again simulated in FDTD and shown in *Figure 4.8(b)*. Larger than 99.8% transmission and lower than -55 dB reflection should be achievable over the whole C+L band.

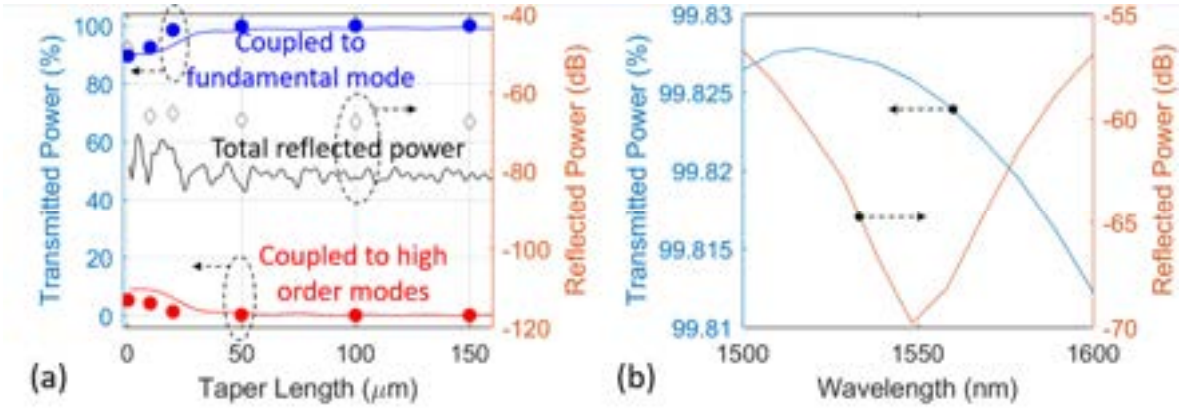

Figure 4.8 (a) Simulation results at 1550 nm wavelength of the optical transmissions and reflections at the deep-shallow taper. The fundamental mode was launched from the ULL silicon waveguide side. Transmitted and reflected powers to the fundamental mode and high order modes were simulated using two methods. The solid lines show the results using mode expansion simulation, while the markers are the data points simulated with FDTD (b) Wavelength dependence of the transmission and reflection from fundamental input mode to fundamental output mode, simulated with FDTD. © MDPI 2018

4.4 Summary

In this chapter, we have successfully developed and accomplished a new type of silicon waveguides with ultralow propagation loss. The waveguides use a shallow (56 nm) rib geometry and can be seamlessly integrated into our standard heterogeneous silicon/III-V

active components such as lasers, modulators, and photodetectors. Waveguide loss is as low as 0.04 dB/cm for a multimode waveguide and 0.16 dB/cm for a quasi-single mode waveguide. This low loss performance results in record high-Q ring resonators and narrowband grating-based filters. We have demonstrated ring resonators with 4.1 million intrinsic Q, and ultra-narrow band Bragg gratings, which are essential to achieve ~100 Hz level linewidth lasers on silicon. Finally, we show a simple way to bridge this ultralow loss waveguide to the standard waveguide using a taper design with negligible insertion loss.

References

[1] T. Komljenovic and J. E. Bowers, "Monolithically Integrated High- Rings for Narrow Linewidth Widely Tunable Lasers," *IEEE J. Quantum Electron.*, vol. 51, no. 11, pp. 1–10, 2015.

[2] D. Melati, A. Melloni, and F. Morichetti, "Real photonic waveguides: guiding light through imperfections," *Adv. Opt. Photonics*, vol. 6, no. 2, p. 156, Jun. 2014.

[3] D. Melati, F. Morichetti, and A. Melloni, "A unified approach for radiative losses and backscattering in optical waveguides," *J. Opt. (United Kingdom)*, vol. 16, no. 5, p. 055502, 2014.

[4] M. L. Davenport, S. Liu, and J. E. Bowers, "Integrated heterogeneous silicon / III – V mode-locked lasers," *Photonics Res.*, vol. 6, no. 5, pp. 468–478, 2018.

[5] M. A. Tran, T. Komljenovic, J. C. Hulme, M. Kennedy, D. J. Blumenthal, and J. E. Bowers, "Integrated optical driver for interferometric optical gyroscopes," *Opt. Express*, vol. 4, no. 4, pp. 3826–3840, 2017.

[6] C. Zhang, S. Zhang, J. D. Peters, and J. E. Bowers, "$8 \times 8 \times 40$ Gbps fully integrated silicon photonic network on chip," *Optica*, vol. 3, no. 7, p. 785, 2016.

[7] B. J. Soller, D. K. Gifford, M. S. Wolfe, and M. E. Froggatt, "High resolution optical frequency domain reflectometry for characterization of components and assemblies."

[8] J. F. Bauters *et al.*, "Planar waveguides with less than 0.1 dB/m propagation loss fabricated with wafer bonding.," *Opt. Express*, vol. 19, no. 24, pp. 24090–101, Nov. 2011.

[9] A. Biberman, M. J. Shaw, E. Timurdogan, J. B. Wright, and M. R. Watts, "Ultralow-Loss Silicon Ring Resonators," vol. 37, no. 20, pp. 4236–4238, 2012.

[10] D. T. Spencer, Y. Tang, J. F. Bauters, M. J. R. Heck, and J. E. Bowers, “Integrated Si 3 N 4 / SiO 2 Ultra High Q Ring Resonators,” vol. 4, pp. 141–142, 2012.

[11] K. Y. Yang *et al.*, “Bridging ultrahigh-Q devices and photonic circuits,” *Nat. Photonics*, vol. 12, no. 5, pp. 297–302, May 2018.

[12] M. H. P. Pfeiffer, J. Liu, M. Geiselmann, and T. J. Kippenberg, “Coupling Ideality of Integrated Planar High- Q Microresonators,” *Phys. Rev. Appl.*, vol. 7, no. 2, p. 024026, Feb. 2017.

[13] M. Davenport, J. Bauters, M. Piels, A. Chen, A. Fang, and J. E. Bowers, “A 400 Gb/s WDM Receiver Using a Low Loss Silicon Nitride AWG Integrated with Hybrid Silicon Photodetectors,” *Opt. Fiber Commun. Conf. Fiber Opt. Eng. Conf. 2013*, p. PDP5C.5, 2013.

[14] M. L. Davenport and J. E. Bowers, “Efficient and broad band coupling between silicon and ultra-low-loss silicon nitride waveguides,” in *2016 IEEE Photonics Conference (IPC)*, 2016, pp. 631–632.

[15] M. Poulin *et al.*, “Ultra-narrowband fiber Bragg gratings for laser linewidth reduction and RF filtering,” 2010, vol. 7579, p. 75791C.

[16] D. T. Spencer, M. Davenport, S. Srinivasan, J. Khurgin, P. A. Morton, and J. E. Bowers, “Low kappa, narrow bandwidth Si_3N_4 Bragg gratings,” *Opt. Express*, vol. 23, no. 23, p. 30329, 2015.

Chapter 5. Ultralow Noise Widely Tunable Lasers

This chapter presents ultralow noise lasers (140 Hz fundamental linewidth) with ultrawide wavelength tuning range (up to 120 nm). These record-breaking performances are achievable only with the incorporation of the ultralow loss silicon waveguides developed in chapter 4.

The laser structural concept is shown in *Figure 5.1*. The laser utilizes the ultralow loss high Q ring resonators (56 nm etch-depth) in the extended cavity (multiring mirrors) for linewidth narrowing. The standard Si waveguides (231 nm etch-depth) are used elsewhere for a high gain performance Si/III-V in the active section and for small footprint in the passive components (*e.g.* couplers, small loop mirror, phase shifters).

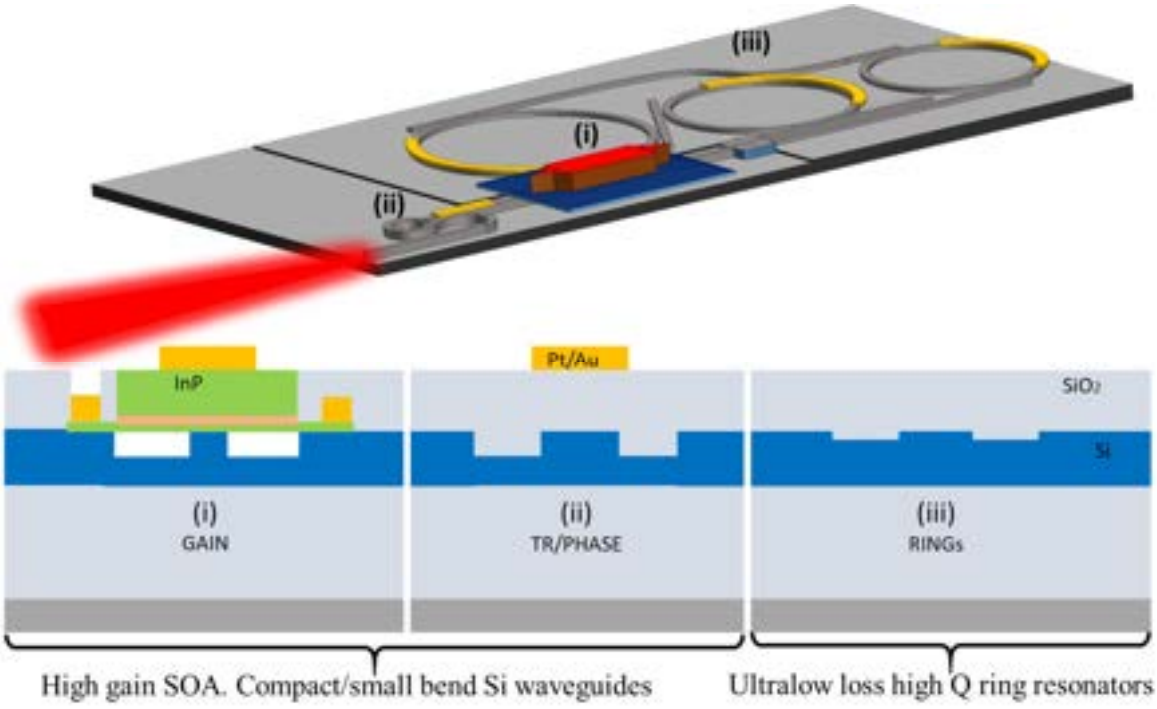

Figure 5.1 Conceptual illustration of the ultralow noise tunable laser integrated on Si/III-V.

5.1 Laser Designs

The structure of the lasers is similar to that of the dual-ring mirror laser presented in chapter 3 with some necessary modifications to suit for the desired ultrawide tunability. The schematic

designs of the lasers with triple-ring mirror and quad-ring mirror are illustrated in *Figure 2.1(a)* and *(b)* respectively.

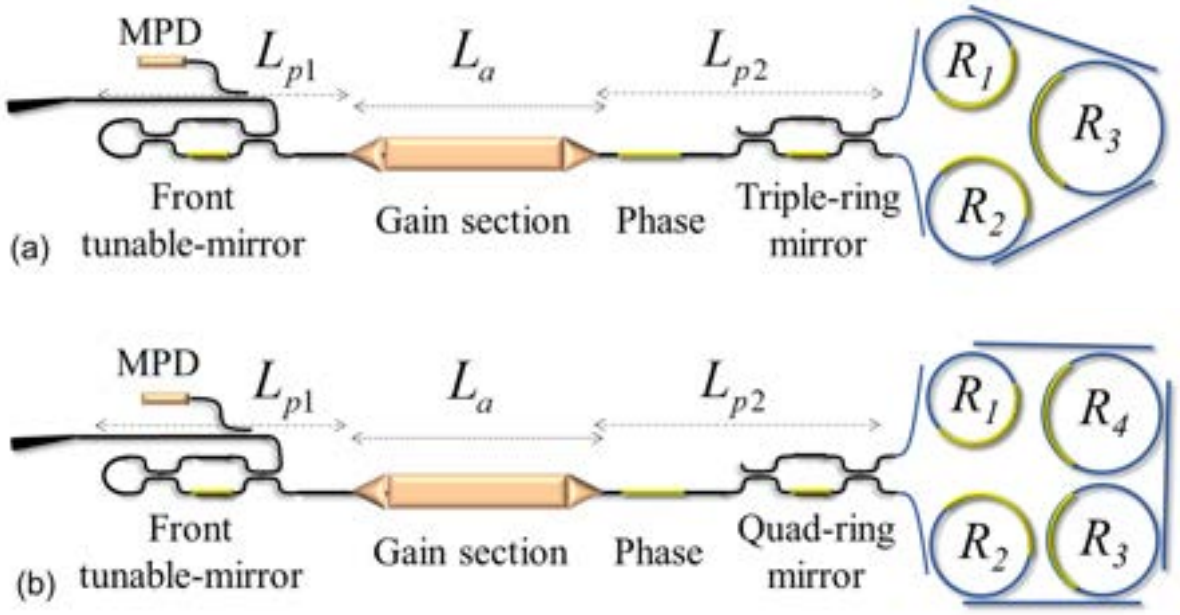

Figure 5.2 Schematic of tunable lasers. The front-mirror is a tunable-mirror formed with an MZI tunable directional coupler. Gain section is an optical amplifier heterogeneous Si/III-V waveguide, connected to the Si passive waveguides via two Si/III-V tapers. The phase tuner is a microheater on the top cladding of the Si waveguide. The back-mirror is a multiring mirror with, (a) three rings, (b) four rings, and a tunable coupler. 231 nm etch Si waveguides are drawn in black while 56 nm etch Si waveguides are in blue.

Key components are listed below:

(a) *Front tunable-mirror (low reflective mirror)*: The front-side loop mirror formed by looping the two ports of a tunable MZI directional coupler. Since the reflectivity is adjustable for any wavelength, we can achieve the optimal point over the whole ~120 nm span. The rib Si waveguide is 231 nm etched from the 500 nm thick Si layer

(b) *A single-sectioned optical amplifier Si/III-V waveguide (gain section)*: We keep the same design of the amplifier waveguides used previously in Chapter 3 but the length

of this active element is made 2.5 mm long to scale up with the total cavity length design.

(c) *Phase tuner*: A long metal (Ti/Pt) strip is deposited vertically on the top of the oxide cladding of the Si waveguide to form the microheater for phase tuning using the thermo-refractive effect.

(d) *Multiring mirrors*: The back-side mirror of the laser is a multiring mirror structure formed by a tunable coupler and three ring resonators - as in triple-ring mirror design, or four ring resonators - as in quad-ring mirror design, cascaded in a loop in add-drop configurations. The ring resonators are all 56 nm etched Si rib waveguides (therefore sketched in different color from the rest in *Figure 5.2*. The designs of these multiring mirrors are the focus of the sub-sections that follow.

5.1.1 *Ring resonators*

The geometry of the ultralow loss waveguides used for the ring resonators should be single-mode for good laser operation. From the mode analysis shown (see chapter 4), a waveguide width of 1.8 μm and 56 nm etch-depth rib is chosen to meet that requirement. From the experiment results in chapter 4, the waveguide loss was measured to be lower than 0.16 dB/cm across the C+L bands and minimum bend radius is about 600 μm. Similar to the implementation in chapter 3, we also design the ring resonators here in the simple configuration of a circular ring closed to a straight bus waveguide (*Figure 5.3(a)*). The power cross coupling ratio between the bus and the ring is simulated using the eigen-mode expansion and CMT methods. A sweep of the two key parameters, ring radius and gap, were carried out to obtain a two-dimensional map shown in *Figure 5.3(b)*. The map is convenient for the designer to look up for appropriate pairs of parameter values for desired coupling ratios.

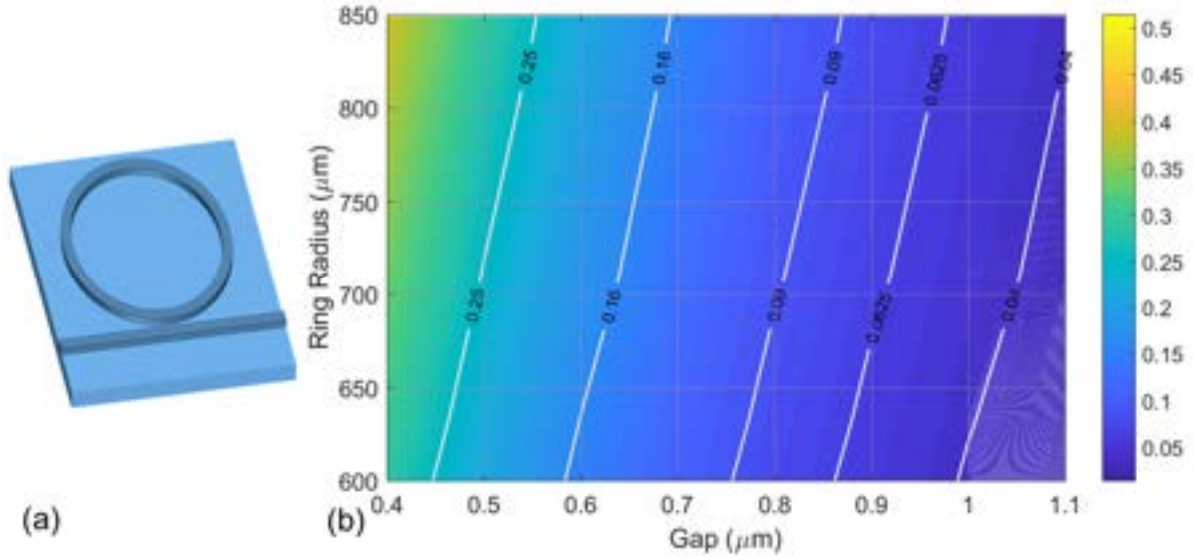

Figure 5.3 (a) Schematic of the ring-bus coupler structure for simulation. (b) Power cross coupling ratio as a function of the ring radius and the gap between the ring and bus waveguide.

5.1.2 *Multiring mirrors*

One immediate downside of the ultralow loss waveguides is their large bend radius, which is almost 10x larger than that of the standard Si waveguides. The large radius results in a small FSR of the ring and renders the dual-ring mirror incapable of providing sufficient side-mode-suppression-ratio (SMSR) for stable single mode lasing. To see this, *Figure 5.4* shows the reflection spectrum of a dual-ring mirror with ring radii of 599.97 and 600.86 μm, and power coupling ratios all equal to 0.09. The spectrum is very dense when looking at wide wavelength span (*Figure 5.4(a)*) due to the individual ring's ring FSR. When zooming in as in *Figure 5.4(b)*, we could see many strong resonant modes closed to each other. That is not good for our single frequency laser design.

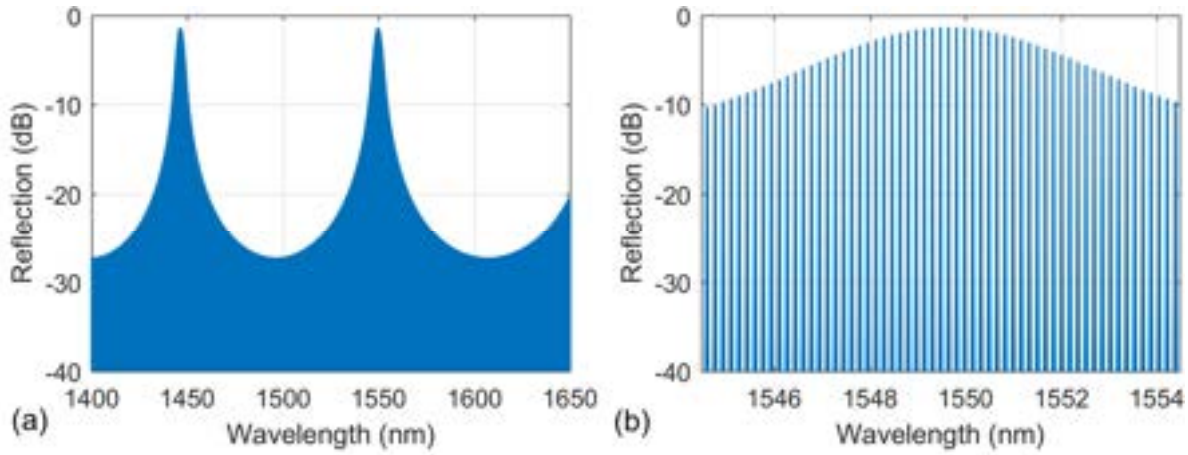

Figure 5.4 Reflection spectrum of dual-ring mirror structure with large bend radii (~600 µm) shows low side mode suppression ratio. Plot (b) is the close-up of (a).

To overcome this issue, we need to enhance the SMSR by having more filtering elements. Here, we do that by the addition of more ring resonators, *i.e.* multiring mirrors with three and four ring resonators, as illustrated in *Figure 3.2(a, b)*.

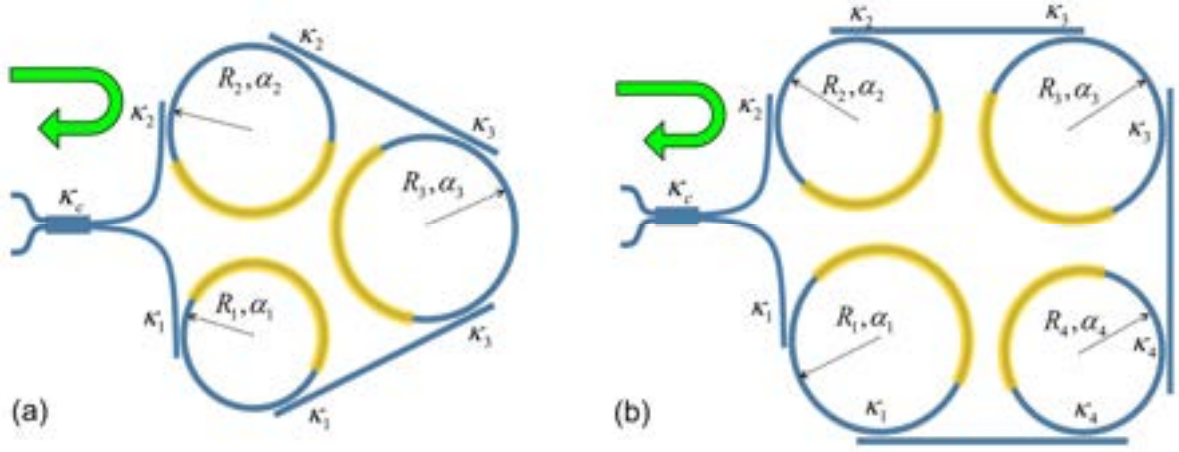

Figure 5.5 Generic configuration of (a) triple-ring mirror (b) quad-ring mirror.

Multiring mirrors are simply the extension of the dual-ring mirror configuration presented in Chapter 3. The Vernier FSR, which sets the tuning span of the tunable lasers, is determined by the first two rings, so-called the Vernier rings. The radii of the third and the fourth ring (if

applicable) would be chosen appropriately to achieve the maximum side mode suppression effect.

For spectral analysis, we come back to the analytical results for multiring ring mirrors derived in Appendix 1. The bus-ring coupling ratios for each ring, ring radius and amplitude propagation loss constant are denoted by κ_m, R_m, α_m ($m = \overline{1,4}$). For triple- and quad-ring mirror structures as shown in *Figure 5.5* where the coupling ratios for add and drop are the same on each ring, the complex amplitude reflectivity of the mirrors is given by

$$r_{mirror} = -2j\sqrt{\left(1-\kappa_c^2\right)\kappa_c^2}\cdot\prod_{m=1}^{4} t_{drop}\left(\kappa_m,\kappa_m,R_m,\alpha_p\right) \qquad (5.16)$$

$$t_{drop}\left(\kappa_m,\kappa_m,R_m,\alpha_p\right) = \frac{-\kappa_m^2\left(2\pi R_m\alpha_p\right)^{1/2} e^{j2\pi R_m\beta_p/2}}{1-\left(1-\kappa_m^2\right)2\pi R_m\alpha_p e^{j2\pi R_m\beta_p}} \qquad (5.17)$$

where β_p is the effective propagation constant in the waveguide and the subscript *m* stands for the ring resonators.

Table 5.1 Multi-ring mirror design parameters

Mirror design	κ^2	**R_1 (μm)**	**R_2 (μm)**	**R_3 (μm)**	**R_4 (μm)**	**Vernier FSR (nm)**
Triple-ring	0.09	599.97	600.86	707.57	-	*113.9*
Quad-ring	0.16	599.97	600.79	711.6	849.43	*123.4*

Upon all considerations, our chosen designs for triple-ring mirror and quad-ring mirror are listed in *Table 5.1*. Within each mirror, the power cross coupling ratios at all the ring resonators are chosen to be the same value (κ^2). The spectral responses of the triple-ring mirror are shown in *Figure 5.6*, where a broad reflection spectrum and a close-in spectrum are plotted. The broad spectrum (*Figure 5.6(a)*) shows us a ~114 nm Vernier FSR, while the close-in spectrum (*Figure 5.6(b)*) reveals how effectively the third ring resonator helps suppress the

sidemodes. As a result, an SMSR over the whole span of > 8dB is achieved, a substantial improvement from what we got with only the two Vernier rings (as in *Figure 5.4(b)*).

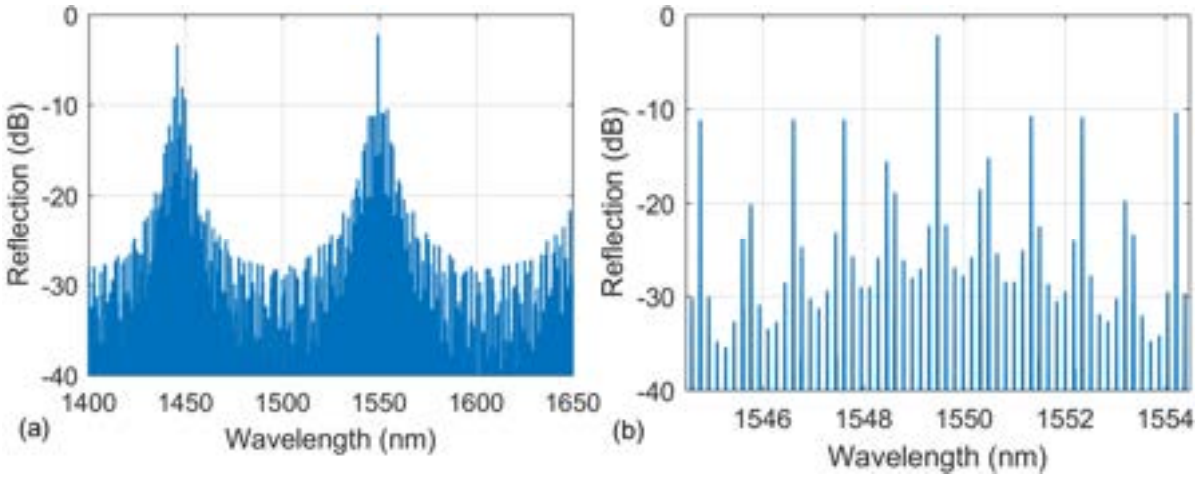

Figure 5.6 Reflection spectra of the triple-ring mirror (a) Broad spectrum shows the wavelength response across two Vernier FSRs (b) Close-in spectrum shows the sidemodes near the central reflection resonance peak with SMSR >8 dB.

For the quad-ring mirror, the addition of two more ring resonators provides more capability to engineer the mirror wavelength response. As shown in the *Figure 5.7*, higher (>16 dB) SMSR can be achieved even with the higher power coupling ratios ($\kappa^2 = 0.16$) than the triple-ring mirror. This means resonators in quad-ring mirror can have lower Q than that in the triple-ring mirror to obtain equivalent performance. The price for this additional advantage is, obviously, the increase in the total foot print and the addition of one more control element needed for resonance alignment. The calculated designed FSR is about ~123 nm.

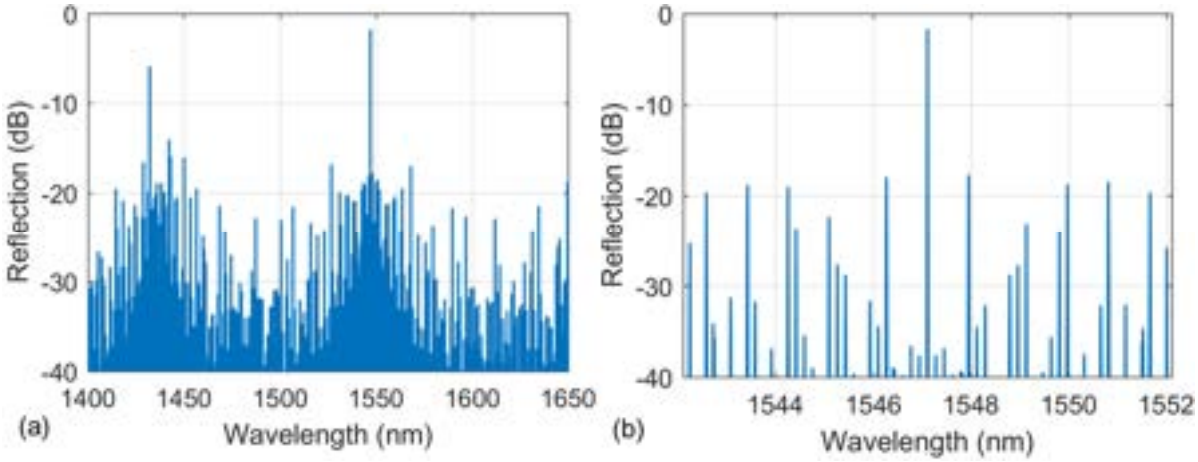

Figure 5.7 Reflection spectra of the quad-ring mirror (a) Broad spectrum shows the wavelength response across two Vernier FSRs (b) Close-in spectrum shows the sidemodes near the central reflection resonance peak with SMSR >16 dB.

Finally, *Figure 5.8* plots the laser's effective cavity length calculated for the case of (a) triple-ring mirror and (b) quad-ring mirror. Both mirrors result in very long cavity length (>50 mm), which would provide a highly coherent laser field.

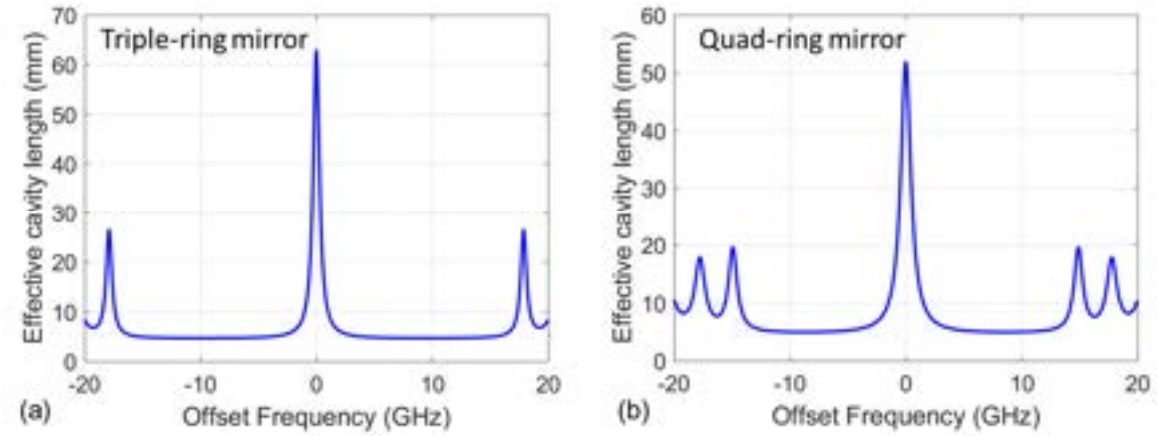

Figure 5.8 Effective cavity length of the laser with (a) the triple-ring mirror (b) the quad-ring mirror.

5.1.3 *Laser linewidth simulation*

We reuse the modeling and approximation method previously used in chapter 3. The list of parameters is shown in *Table 5.2*; most of these parameters are identical to what were used in Chapter 3 with changes in bold.

Table 5.2 List of parameters used for laser linewidth calculations

Parameter	Symbol	Value	Unit
Wavelength	λ	1.575	μm
Planck constant	h	$6.62607004 \times 10^{-34}$	m^2kg / s
Light velocity	c	299792458	m/s
Optical frequency	ν	c / λ	Hz
Mode's group index	n_g	3.8/3.61	
Mode's group velocity	v_g	c / n_g	cm/s
Spontaneous emission factor	n_{sp}	1.5	
Linewidth enhancement factor	α_H	4	
Gain section internal loss	α_i	6	cm^{-1}
Si waveguide loss	α_p	**0.16**	dB/cm
III-V/Si taper loss	δ_{taper}^{dB}	0.5	dB
Gain length	L_a	**2.5**	mm
Routing waveguide total length	L_p	**2**	mm
Output Power	P_0	10	mW

The estimated values of *A, B*, and *F* and the modified Schawlow-Townes linewidth as functions of the frequency detuning from the resonance peak frequency are then calculated for the two designs (revisit the laser simulation section in Chapter 3 for details), with the output power assumed to be 10 mW. Both designs show achievable linewidths in 10s of Hz

level, in theory. This is two order of magnitude improvement in linewidth from the results achieved with dual-ring mirror using higher loss Si waveguides in chapter 3.

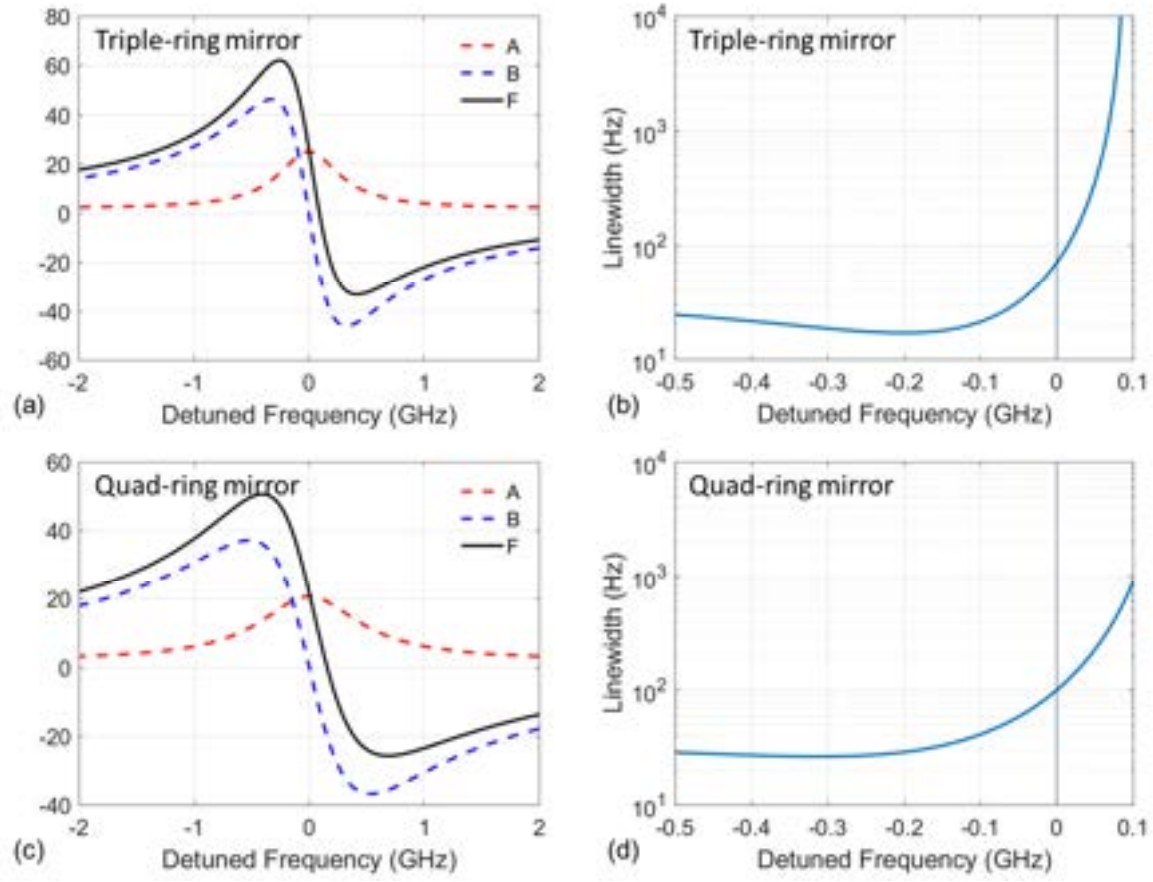

Figure 5.9 Calculated values for coefficients A, B and F and estimated Lorentzian linewidth as functions of frequency detuned from the reflection peak resonance for a laser output power of 10 mW. Values of parameters used for these calculations are listed in Table 5.1 and Table 5.2. Figures (a-b) are of the triple-ring mirror laser and (c-d) are of the quad-ring mirror laser.

5.2 Laser fabrication

The designed laser is then fabricated in a modified version of Si/III-V heterogeneous process. Some modification was necessary, including the self-aligned process for etching Si waveguides for zero-misalignment in the transition between 56 nm and 231 nm etch-depths,

and the selective bonding process to preserve the ultralow loss Si waveguide area from III-V bonding. The fabrication process flow can be found in Appendix 3. Stitched microscopic images of completed devices are shown in *Figure 5.10(a)* and *(b)*. SEM images of the self-aligned transition between two types of Si waveguides and Si/III-V taper are also shown in the insets *(i)* and *(ii)*. The facets of the lasers were mechanically polished for fiber coupling.

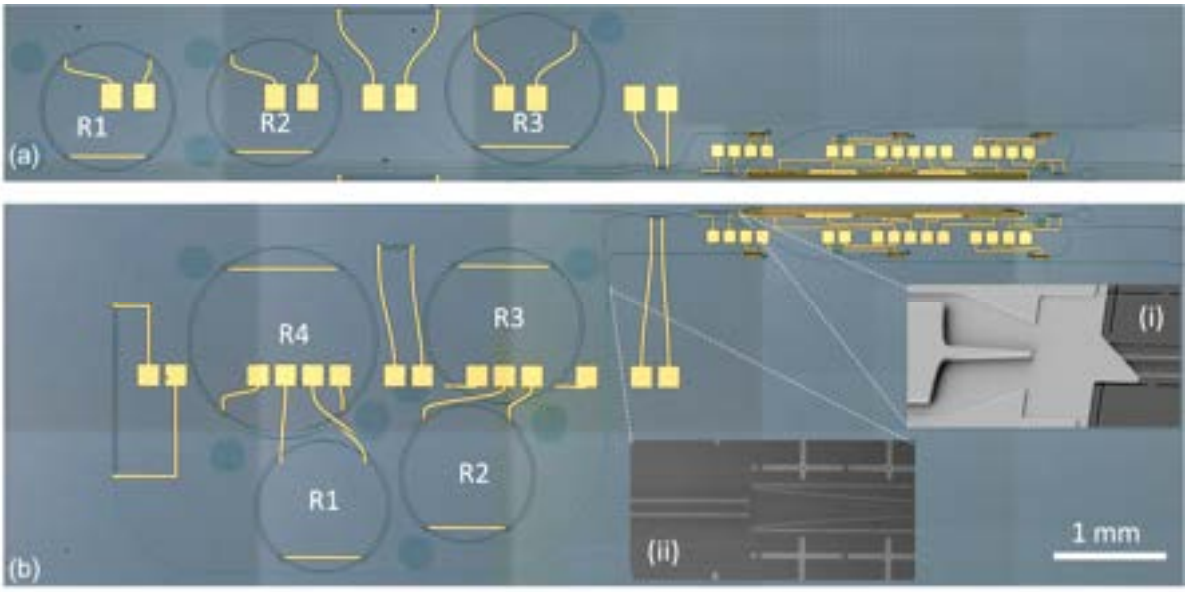

Figure 5.10 (a) Microscopic images of a fabricated triple-ring mirror laser (b) Microscopic images of a fabricated triple-ring mirror laser. (i) SEM image of a Si/III-V taper. (ii) SEM image of a transition from 56 nm to 231 nm etched waveguides.

Unfortunately, right after the fabrication is completed, the lasers had an extremely high contact resistivity due to some unclear fabrication issues. Very small amount of current could barely flow despite high bias voltage. The diode electrical property was notably remedied after an additional rapid-thermal-annealing, and then improved to an acceptable level after tens of minutes of continuous burn-in process, *i.e.* when a fixed current was forced to flow through the diode, the bias voltage gradually reduces until saturates. These issues possibly relate to 1) hydrogen contamination happened during some dry etching and oxide deposition processes

that contain hydrogen gas [11], and 2) bad interface between contact metal and semiconductor. Future work should definitely address this issue to achieve lasers with better performance.

5.3 Laser characterization

The lasers were measured on a temperature-controlled stage set at 20°C. The output light is coupled into a 2.5 μm spot-size lensed fiber for characterization of spectral properties such as wavelength tuning, spectral linewidth and frequency noise. A Faraday based in-line optical isolator with larger than 50 dB extinction ratio was connected to the lenses fiber to eliminate any unintentional reflections towards the laser. The current-voltage curve of the lasers are shown in *Figure 5.11*(*a)*, while the current-output power curve for the triple-ring mirror laser is shown in *Figure 5.11*(*b)*. The left y-axis in *Figure 5.11*(*b)* shows the lasing wavelength at each current point. At each point the rings and phase section were tuned to obtain the maximum power, but the wavelength shifted quite a bit due to the thermal crosstalk between the active sections and the rings, and that resulted in the non-smooth L-I curve. The laser's threshold current was about 100 mA. The max output power was only ~3 mW, which is ~3.3 times lower than the values used for the linewidth calculations in the previous section.

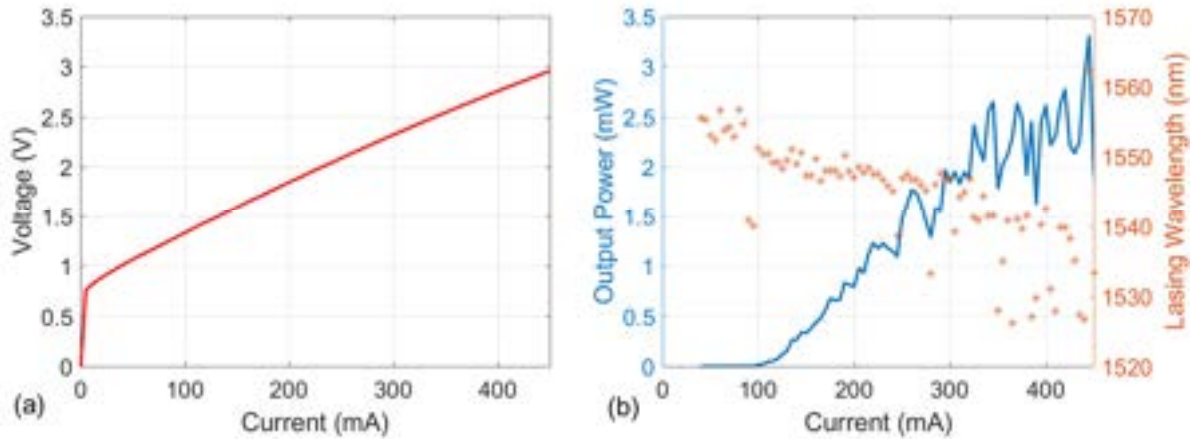

Figure 5.11 (a) Current-voltage relation of the 2.5 mm long gain section (b) The light-current curve of the triple-ring laser. The lasing wavelength was not kept constant across the current sweeping, shown in the right y-axis.

5.3.1 *Wavelength tuning*

We tested the laser wavelength tuning at a fixed injection current of 300 mA (~3x threshold current) to the gain section of the laser. The lasing spectra are acquired by a grating-based optical spectrum analyzer. An initial coarse tuning was done to acquire the lasing spectra across the tuning range and followed by a two-dimensional sweep of ring fine tunings to obtain the full tuning map for the laser. In our test procedure, the electrical powers applied to the heaters on top of two ring main Vernier resonators are stepped. For each operation point, the power applied to the heaters on top of the remaining ring resonators, phase section and the tunable couplers is was tuned to achieve the maximum output power indicated by the photocurrent read-out on the on-chip monitor photodiode. Because of thermal crosstalk between elements, it was necessary to run several tuning optimization cycles for each operation point. The measurement was automated by a computer program. The lasing spectra at different pair values of heater powers on two rings are recorded and post-processed for our analysis.

Results for the triple-ring mirror laser is shown in. The course tuning in *Figure 5.12 (a)* shows a 110 nm wide wavelength tuning from 1490 nm to 1600 nm. This is in good agreement with the designed Vernier FSR of ~113 nm (see *Table 5.1*). A linear and smooth 2D wavelength tuning map is achieved, as shown in *Figure 5.12(b)*. The corresponding SMSR map is shown in *Figure 5.12(c)*. SMSRs on almost all of lasing points are within the range 40 ~55 dB, even at wavelength far off from the SOA's gain spectrum peak (~1550 nm). The variation on the

SMSR originates from how well the two ring spectra are aligned to each other at the pre-determined heater setpoints in the test.

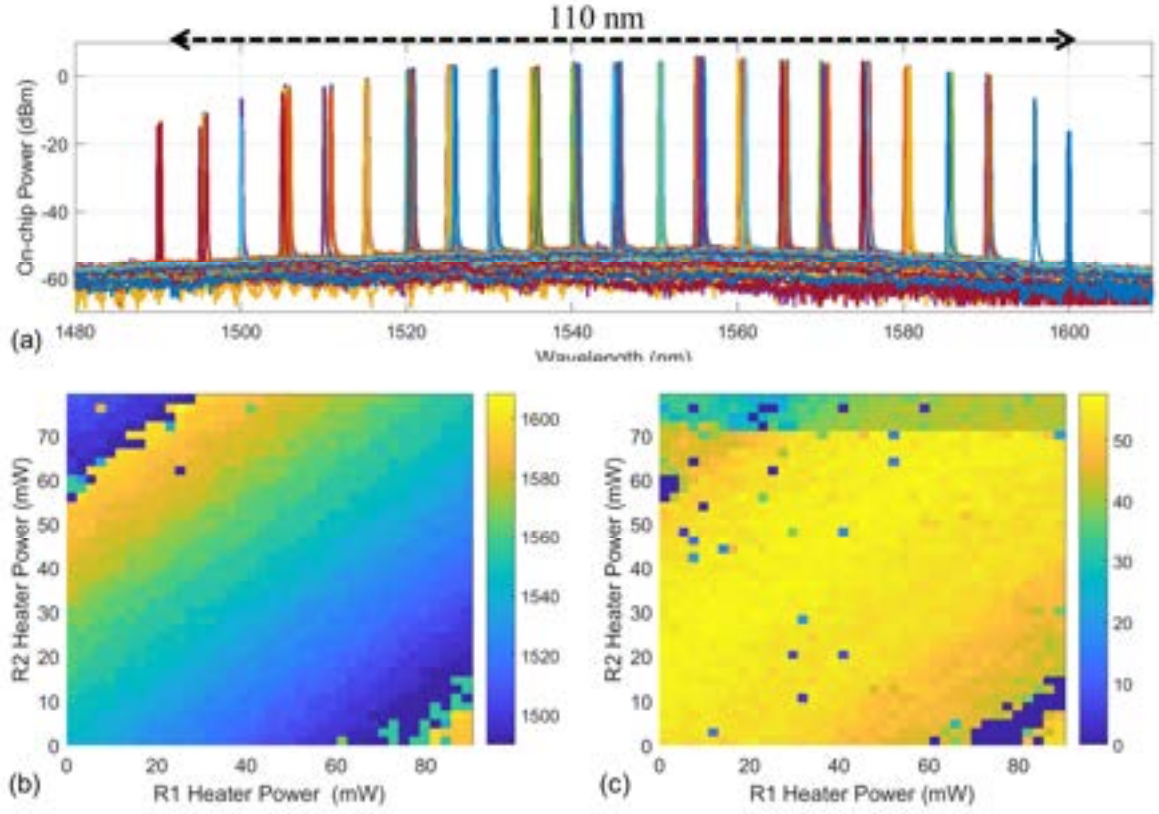

Figure 5.12 Tuning characteristic of the triple-ring mirror laser: (a) Course tuning spectra showing the tuning range of 110 nm (b) Two-dimensional wavelength tuning map of the dual-ring mirror laser. The color indicates the lasing wavelength in unit of nm. (c) Side-mode suppression ratio (SMSR) of the corresponding wavelength tuning map, showing >40 dB on most of the operation points.

Results for the quad-ring mirror laser is shown in *Figure 5.13*. Unfortunately, due to issues with electrical contact and for some unknown reasons, the gain spectrum had degraded quickly after operating for a short duration. The gain spectrum shape distorted after the degradation. Although we could still have lasing, the laser power was dropped by 10-15 dB. Despite all of those problem, the coarse tuning in *Figure 5.13(a)* still shows a 120 nm wide wavelength tuning from 1484 nm to 1604 nm, which is close to the designed 123 nm Vernier FSR (see

Table 5.1). The 2D wavelength tuning map is shown in *Figure 5.13 (b)* and the corresponding SMSR map is shown in *Figure 5.13 (c)*. The tuning map is more erratic than that of the triple-ring mirror laser, partially from the additional difficulty of having one more sensitive ring that needed to be tuned and the thermal crosstalk between many tuning elements. A more advanced tuning algorithm might be helpful in improving the wavelength tuning performance of the laser.

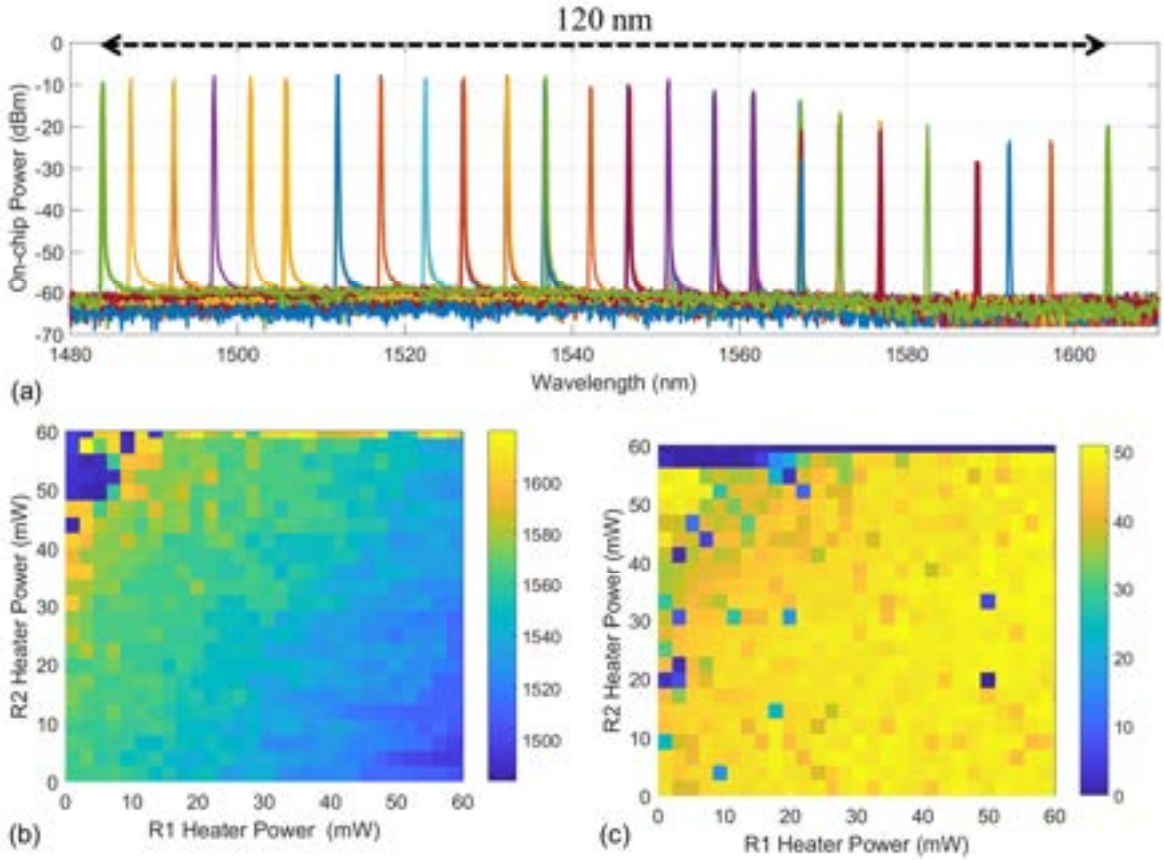

Figure 5.13 Tuning characteristic of the fabricated quad-ring mirror laser: (a) Course tuning spectra showing the tuning range of 120 nm (b) Two-dimensional wavelength tuning map of the dual-ring mirror laser. (c) Side-mode suppression ratio (SMSR) of the corresponding wavelength tuning map.

5.3.2 *Frequency noise and linewidth*

We measured the laser's frequency noise to characterize the linewidth of interest. Due to the availability of the testing tools at the time, the triple-ring mirror laser was measured with a Sycatus/Ogmentum phase noise measurement system [1], which has 20 MHz bandwidth, while the quad-ring mirror laser was tested with a measurement system provided by OEWaves [2] which extends up to 100 MHz.

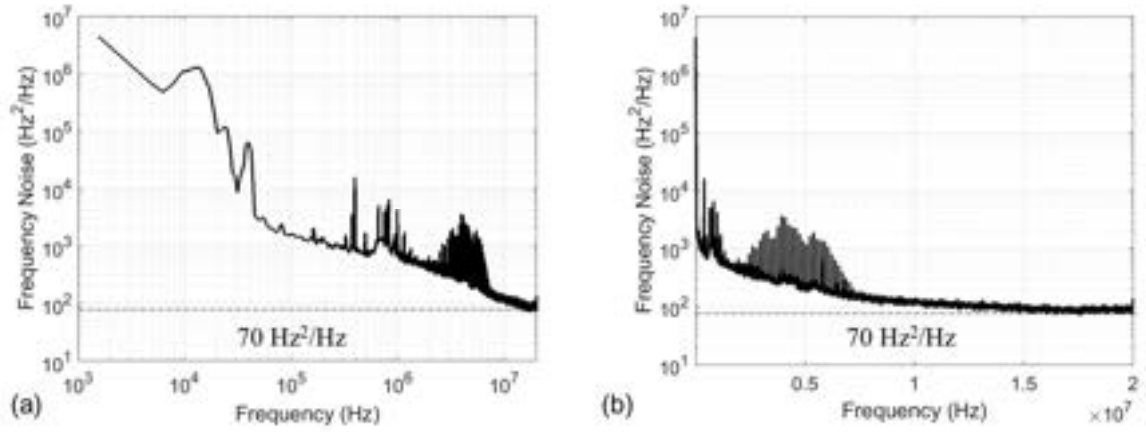

Figure 5.14 (a) Frequency noise spectrum of the fabricated triple-ring mirror laser measured at 300 mA. (b) The same spectrum plotted with x-axis in linear scale to zoom-in on the noise at high frequency range. An upper bound of 70 Hz²/Hz for the white noise level is drawn.

The one-sided spectrum of frequency noise power spectral density of the fabricated triple-ring mirror laser is shown in *Figure 5.14*. The measurement was taken at 300 mA pump current and slightly detuned from the peak resonance of 1545 nm wavelength. Despite using all battery powered current sources isolated from power lines, there is still significant contribution to the measurement from other sources in the 10kHz to 10MHz range. The frequency noise spectrum seems to have not fully reached its white noise level within 20 MHz measurement bandwidth. Therefore, we deem 70 Hz^2/Hz as the upper-bound of the laser's

white noise level. It is equivalent to state that the Lorentzian linewidth of the fabricated triple-ring mirror is lower than 220 Hz [3].

The frequency noise of the quad-ring mirror laser was tested, fortunately, before the catastrophic degradation happened, at 1565 nm wavelength and output power of about 2 mW. The one-sided spectrum of frequency noise power spectral density is shown in *Figure 5.15.* The spectrum was somewhat hindered by the spikes at 18 MHz and harmonics, which are the frequency fringes corresponding to the free spectral range of the fiber MZI used in the measurement system. However, it is possible to observe the laser's true noise behavior outside the spike areas. We could see that the laser frequency noise is still dominated by colored noise up to 35 MHz level. A white noise level of 45 Hz^2/Hz starts to be seen at about 60 -80 MHz frequency range. That corresponds to a Lorentzian linewidth of 140 Hz.

Note that the factor of 5.5 times difference between this measured linewidth of the quad-ring laser with the predicted linewidth (~25 Hz) in *Figure 5.9(d)* in section 5.1.3 is largely due to the fact that the measured output power (2 mW) is 5 times lower than the assumed output power for the calculation (10 mW). This justifies the result discrepancy because the laser linewidth is inversely proportional to output power level.

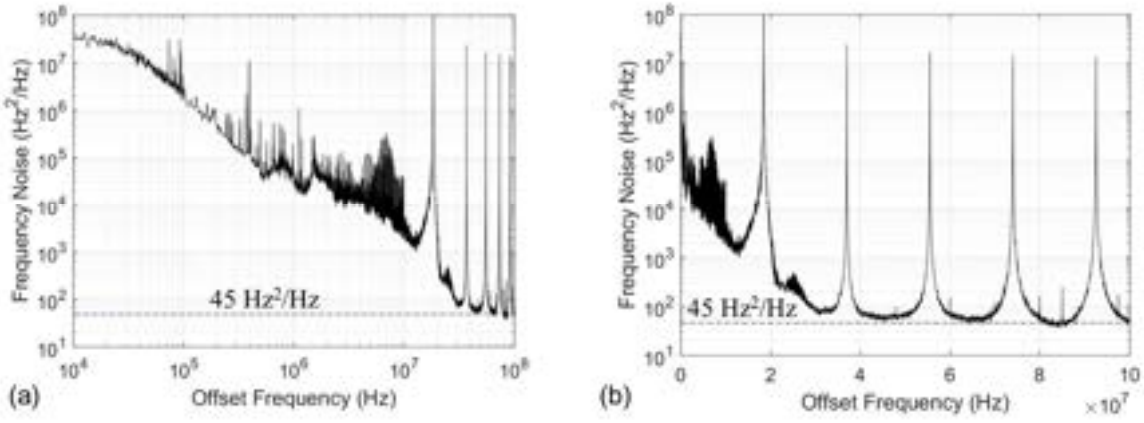

Figure 5.15. (a) Frequency noise spectrum of the fabricated quad-ring mirror laser. (b) The same spectrum plotted with x-axis in linear scale to zoom-in on the noise at high frequency range. The spikes at 18 MHz and harmonics are from the measurement tool. A white noise level of 45 Hz^2/Hz is drawn.

5.4 Summary

This chapter described the design, theoretical calculation, fabrication and characterization of heterogeneously integrated Si/III-V lasers using triple-ring and quad-ring mirrors. Both lasers exhibit ultrawide tuning range of 110 nm on the triple-ring and 120 nm on the quad-ring mirror lasers, which is in great compliance with the design.

In term of spectral linewidth, the lasers were expected to achieve 10s Hz linewidth level, but the best linewidth measured experimentally is 140 Hz on the quad-ring mirror laser. The triple-ring mirror laser's linewidth was measured to be lower than 220 Hz, although a conclusive linewidth measurement was not possible due to the measurement tool's limit.

References

[1] "Optical Noise Analyzer." [Online]. Available: http://www.sycatus.com/en/products/ona/. [Accessed: 17-Mar-2019].

[2] "HI-Q Optical TMS | OEwaves." [Online]. Available: https://oewaves.com/hi-q-optical-tms. [Accessed: 13-Mar-2019].

[3] K. Kikuchi and T. Okoshi, "Estimation of Linewidth Enhancement Factor of AlGaAs Lasers by Correlation Measurement Between FM and AM Noises," *IEEE J. Quantum Electron.*, vol. 21, no. 6, pp. 669–673, 1985.

Chapter 6. Ultralow Noise Extended-DBR Lasers

In this chapter, we present the designs and characteristics of fixed wavelength DBR lasers. The so-called Extended-DBR lasers are created by incorporating centimeter-long weak Bragg grating (first demonstrated in Chapter 4) into a part of the laser cavity. The laser architectural concept is shown in *Figure 6.1*. The E-DBR laser shows linewidth lower than 1 kHz. By adding a high-Q ring resonator in cascade with the gratings, the spectral linewidth is lowered to ~500 Hz level on the Ring-Assisted Extended-DBR laser.

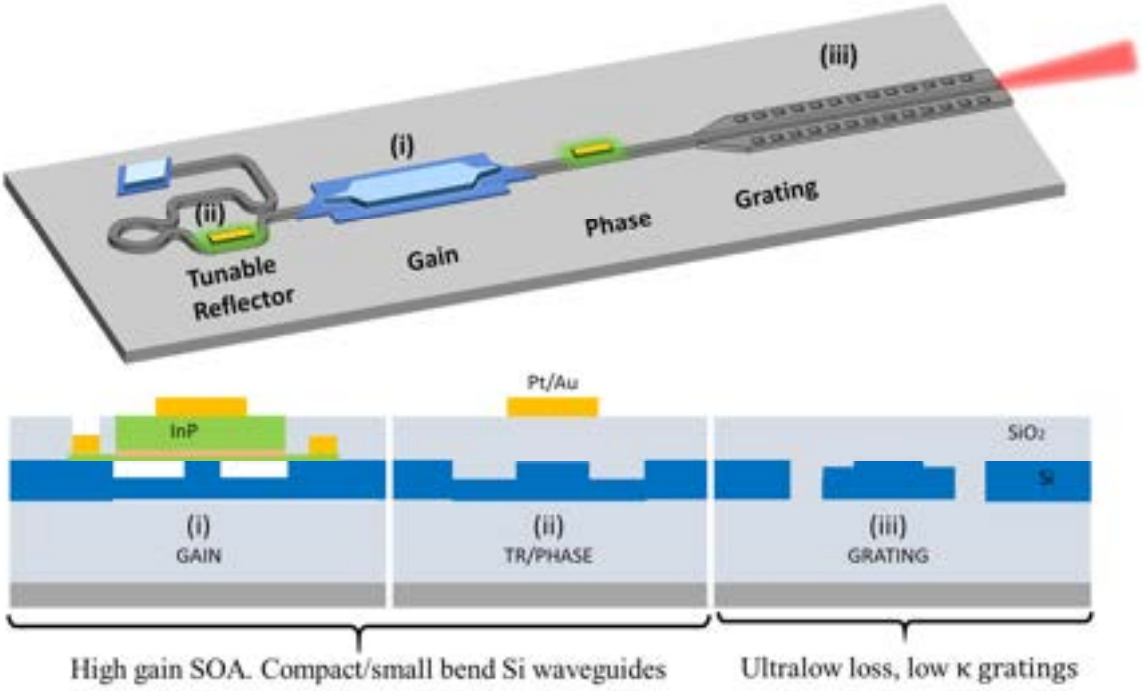

Figure 6.1 Concept of the ultralow noise extended-DBR laser on Si/III-V integrated platform.

6.1 Laser Designs

The requirements to fabricate a Bragg grating with long length and narrow bandwidth are low propagation loss and sufficiently weak perturbations, i.e. low κ. This is depicted in *Figure 6.2*, in which the bandwidth and reflectivity of a uniform grating are simulated. Weakening

the grating decreases the full-width half maximum (FWHM) of the grating and lowers the reflectivity. For the same κL, a longer grating will provide an even narrower passband, but is more sensitive to the optical loss, which also decreases the reflectivity and increases mirror loss. Thus, both weak κ and low waveguide loss are needed to achieve a narrowband grating reflector with enough reflectivity. For E-DBR lasers, we target grating strengths with $\kappa L < 1$, and optical losses less than 0.2dB/cm, both of which are achievable using the ULL silicon platform.

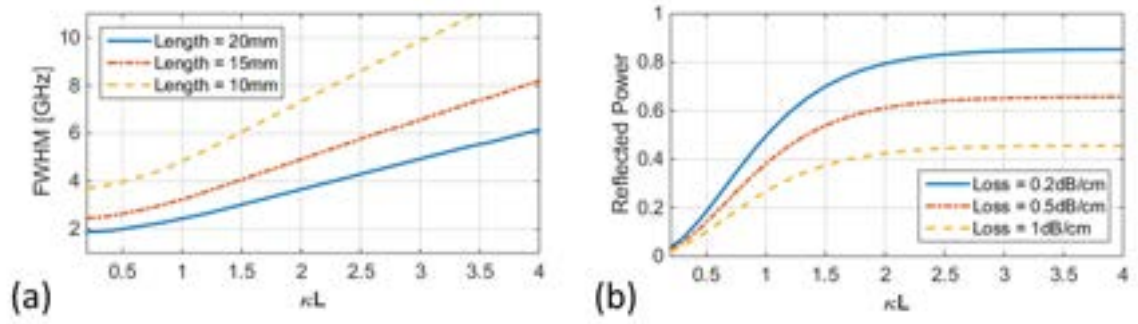

Figure 6.2 Impact of grating strength on the (a) full-width half maximum (FWHM) bandwidth and (b) reflected power assuming a 15mm long uniform grating. The simulations are shown over various lengths and waveguide losses.

For conventional sidewall or surface etched gratings, the power coupling coefficient κ is directly proportional to the perturbation in waveguide width or height respectively. These perturbations become too small to resolve in device fabrication in the limit that κ approaches zero. Alternate grating designs to achieve ultra-low κ were demonstrated for ULL Si_3N_4 waveguides, including etched pillars set back from the waveguide, sampled gratings and higher order gratings [1]. As first demonstrated in chapter 5, ULL shallow etched silicon waveguides utilizes periodically etched holes through the silicon layer on either side of the waveguide to achieve the same low κ values. In this design, κ is inversely proportional to the

distance between the holes and the waveguide, which can be well controlled with lithography. The dependence between this distance and κ was previously simulated and experimentally verified [2]. Finally, the other component enabled by the ULL Si platform is the high-Q ring resonator, which was demonstrated to be as high as 4.1 million for intrinsic Q and 2.1 million for loaded Q. Using a high-Q ring in the laser cavity can serve to further reduce the linewidth, as it provides enhanced cavity length near resonance and sharpens the cavity filter, as we have seen in the previous chapters.

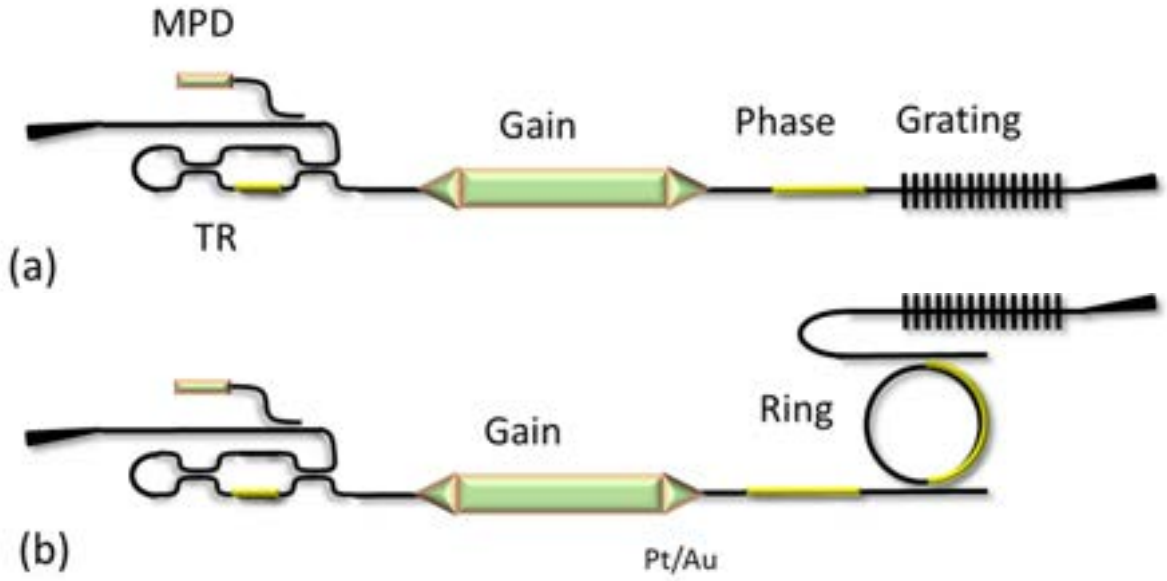

Figure 6.3 (a) Schematic of the E-DBR laser. A ring resonator is incorporated in the cavity (b) to form the RAE-DBR laser.

The two laser designs detailed in this work are shown in *Figure 6.3*; the Extended-DBR (E-DBR) laser and Ring-Assisted E-DBR (RAE-DBR) laser. The lasers include a tunable back mirror, a III-V on silicon gain section, a phase control section, and a long Bragg grating-based front mirror through which the light is output. The RAE-DBR laser has an additional ring

filter as part of the laser cavity to increase the effective cavity length and reduce the reflector sidelobes.

The gain section is the same for the two lasers and consists of InAlGaAs multiple quantum well (MQW) material with 3 quantum wells [3]. The length of the gain section is 2.5mm, and it is connected to the ULL silicon waveguides and gratings through two tapered transitions, as shown in *Figure 6.3(a)*. Each laser also includes a phase control section that can be tuned to align the lasing mode to the reflector peak. The tuning in the laser is achieved via thermal tuning by heating up a metallic resistor located on top of each element. There are no heaters on top of the grating, but one could be included to provide some tunability of the Bragg wavelength. The heaters are separated from the optical waveguide layers by 1μm of sputtered oxide cladding, which is sufficient to avoid any absorption loss by the metal.

The back mirror of the lasers is a tunable reflector consisting of a Mach-Zehnder interferometer (MZI) with a loop mirror. The reflectivity of the mirror can be varied from zero to 4**s**(1-**s**), where **s** is the power splitting ratio of the couplers in the MZI. To obtain the maximum tuning range, **s** is designed to be 0.5. A monitor photodiode (MPD) is included to monitor the reflectivity of the tunable reflector as well as the tuning of the ring and phase sections.

The lasers were fabricated in the same process as the tunable ultralow noise ring-coupled lasers, described in Appendix 3. The light is then edge coupled through a polished angled facet.

6.2 Passive filter characterization

The grating-based reflector for each laser is characterized by the setup shown in *Figure 6.4(a)*. The gain section of the laser is reverse biased to operate as a photodiode, and the photocurrent is recorded as light from an external tunable laser is injected through the grating.

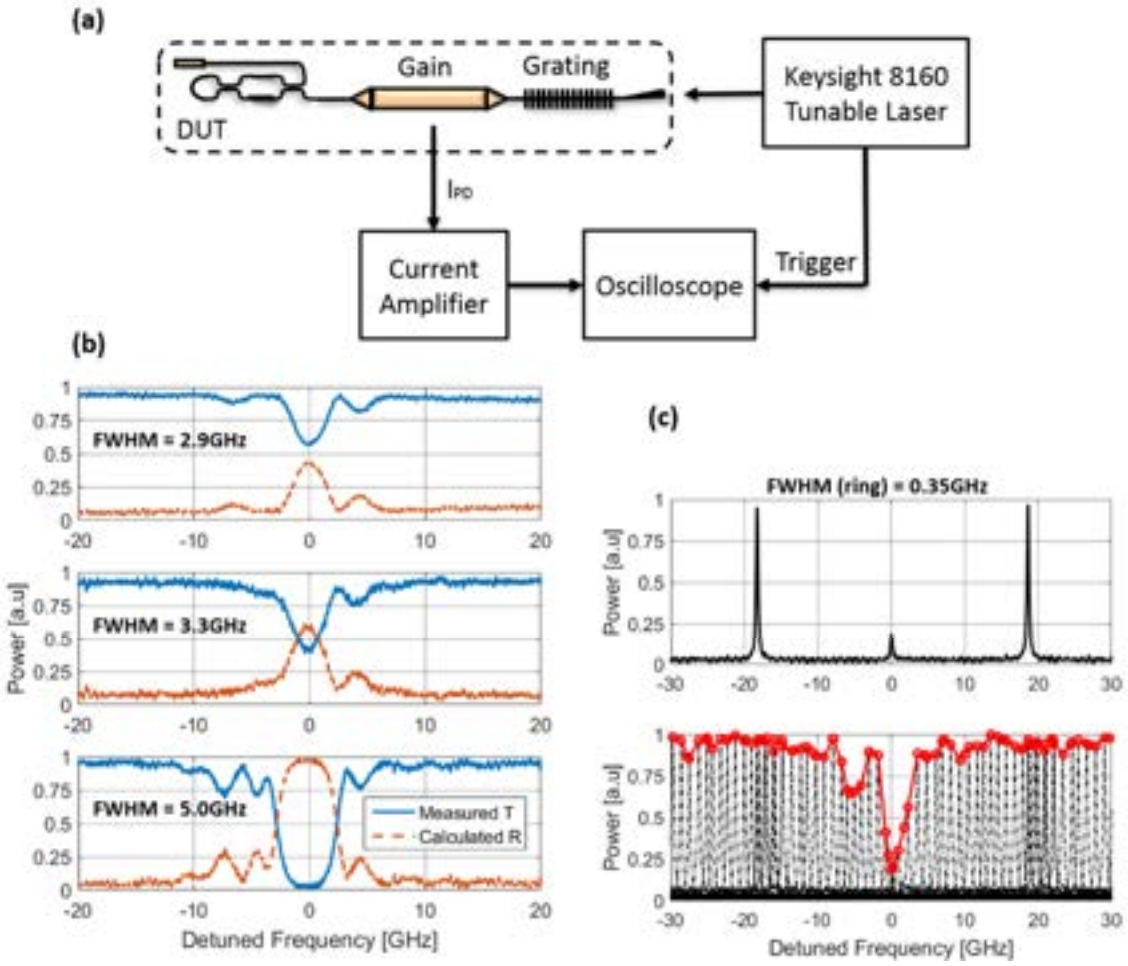

Figure 6.4 (a) Test setup used to characterize the grating-based reflectors in each laser without having to use separate test structures. The measurements for the E-DBR are shown in (b) for a 15mm long grating with designed κL = 0.375, 0.75, and 3 respectively. The measurement for the RAE-DBR is shown in (c), in which the transmission through both the grating and ring is recorded. By tuning the ring across a full FSR, the shape of the grating can be revealed.

For the E-DBR, the photocurrent provides a direct measurement of the transmission spectrum through the grating. The reflection spectrum can then be calculated from the measurement. This method directly characterizes the reflector in the laser rather than relying on test structures, which could deviate from the actual grating in the laser. This also largely avoids the influence of Fabry-Perot ripples from reflections off facets and fibers, which often corrupt the measurement if the reflection spectrum of the grating is measured directly with the use of a circulator. The results for three 15 mm long grating reflectors with designed κL = 0.375, 0.75, and 3 are shown in *Figure 6.4(b)*. As the grating strength increases, the bandwidth and reflectivity increase as well. For the weakest grating, the 3-dB bandwidth of the grating is 2.9 GHz and the peak reflectivity is roughly 40%.

For the RAE-DBR, the photocurrent is a measurement of the grating transmission multiplied by the transmission of the ring filter, as seen from the drop-port. The resulting measurement is shown in *Figure 6.4(c)*, in which the ring resonance at the Bragg wavelength is suppressed by the stopband of the grating. The FWHM of the ring is only 0.35GHz, which is over ten times narrower than the grating. To map out the response of the grating, we tune the ring across a full FSR (18.5GHz) while recording the photocurrent. The resulting traces are overlaid on top of each other in *Figure 6.4(c)*, in which the transmission through the grating can be seen. The FWHM of the grating is roughly 4 GHz, which is much smaller than the FSR of the ring. Thus, only the resonance at the Bragg wavelength will provide reflection back into the laser. The peak reflectivity of the grating is estimated to be nearly 80%, which is higher than expected, given the designed κL = 1.

6.3 Laser characterization

The lasers are characterized on a temperature-controlled stage at room temperature. The output power is measured with a broad-area photodetector, as well as a lensed fiber. Comparisons between the two show 6.5 dB of coupling loss from the 7-degree angled facet to the lensed fiber, which agrees with simulations. This can be reduced with the use of a spot-size converter on the laser output. The tunable loop mirror is set to provide maximum reflection by minimizing the photocurrent at the monitor photodiode, providing the condition with the lowest threshold current for the laser.

6.3.1 *Laser operation and mode hopping*

The measured LIV curve for an E-DBR laser with a designed $\kappa L = 0.375$ is shown in *Figure 6.5(a)*. The laser has a threshold current of 50 mA and a maximum on-chip power of over 37 mW. When coupled into a fiber, the maximum power in the fiber is 8.3 mW. Kinks in the laser power correspond to longitudinal mode hopping in the E-DBR caused by heating of the gain section as the current is increased. This causes the lasing mode to be detuned from the grating peak, which reduces the output power until eventually, the lasing mode hops to the next longitudinal mode. These mode hops are more common at higher currents, since Joule heating is more significant at high currents. By controlling the laser cavity phase, with the tunable phase control element, the E-DBR lasing mode can be aligned with the grating peak through a large part of the LIV curve, providing the cleaner and continuous single-mode output blue curve shown in in *Figure 6.5(a)*. A spectrum of the E-DBR laser is included in the inset, for which the side-mode suppression ratio (SMSR) is over 55 dB.

The LIV of a RAE-DBR laser is shown in in *Figure 6.5(b)*, shown both with and without tuning of the ring. Since the FWHM of the ring is smaller than the grating, it must be tuned to

the Bragg wavelength to minimize losses – providing the higher power and cleaner blue curve. We observe a threshold current of 60 mA and on-chip maximum output power of 4.8 mW. The output power of the RAE-DBR is much lower than the E-DBR due to the higher cavity losses (both propagation loss and coupling loss) going through the add-drop ring twice per round trip, as well as a higher output mirror loss due to stronger than designed grating reflectivity. These losses can be reduced by weakening the grating, increasing the ring coupling coefficients, and/or moving the ring to the back mirror (inside the tunable reflector) so that the light only undergoes one path through the ring per round trip in the cavity. The SMSR for the RAE-DBR laser is also over 55dB.

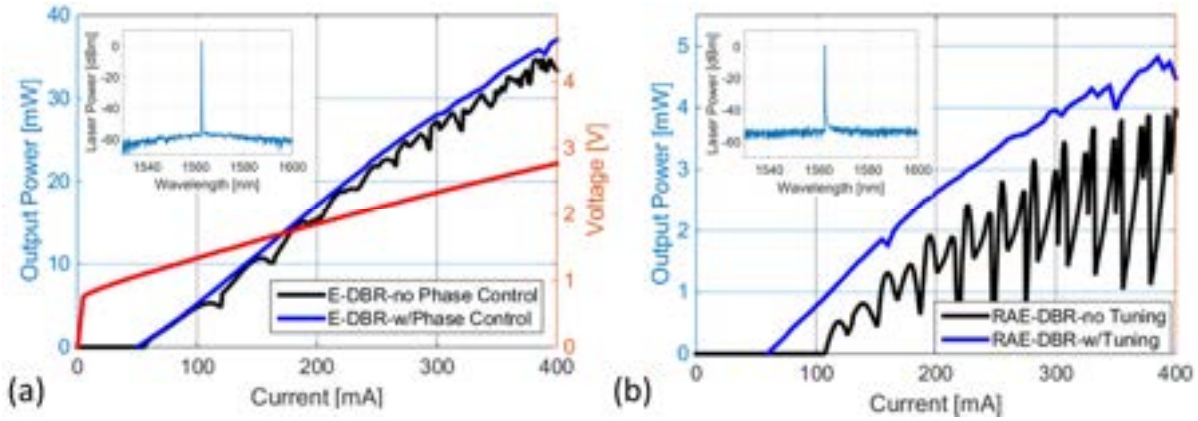

Figure 6.5 (a) LIV curve for the E-DBR laser with $\kappa L = 0.375$ with and without active tuning of the phase control section. The on-chip output power reaches over 37mW. The LI characteristics of the RAE-DBR are shown in (b), with and without active tuning of the ring heater.

Operating the E-DBR near a mode hop can result in multimode, chaotic, or self-pulsing behavior [4], [5]. To study these mode hops in more detail, the power to the phase control section was tuned (up and down) at a fixed gain current of 200 mA, while monitoring the lasing wavelength and peak power at that wavelength using a Yokogawa AQ6150 wavemeter.

The results are shown in *Figure 6.6*. When the laser operates in the vicinity of a mode hop, there is a sudden drop in output power at the lasing wavelength, as multiple longitudinal modes compete to lase. High resolution scans with an OSA show that the E-DBR undergoes several transitions. The laser displays hysteresis effects as to where these mode hops happen. It also appears to be more stable when decreasing the phase power, which shifts the longitudinal modes to shorter wavelengths, than when increasing the phase power. This may be due to the slightly asymmetric spectral response of the grating, as was previously shown in *Figure 6.5*. The on-chip MPD provides an excellent tool for providing real-time feedback as to whether the laser is approaching a mode-hop region, signaling that the phase should be tuned. The mode hops are avoided by actively tuning the phase section along with the gain – as shown in the blue LI curve in *Figure 6.6(a)*.

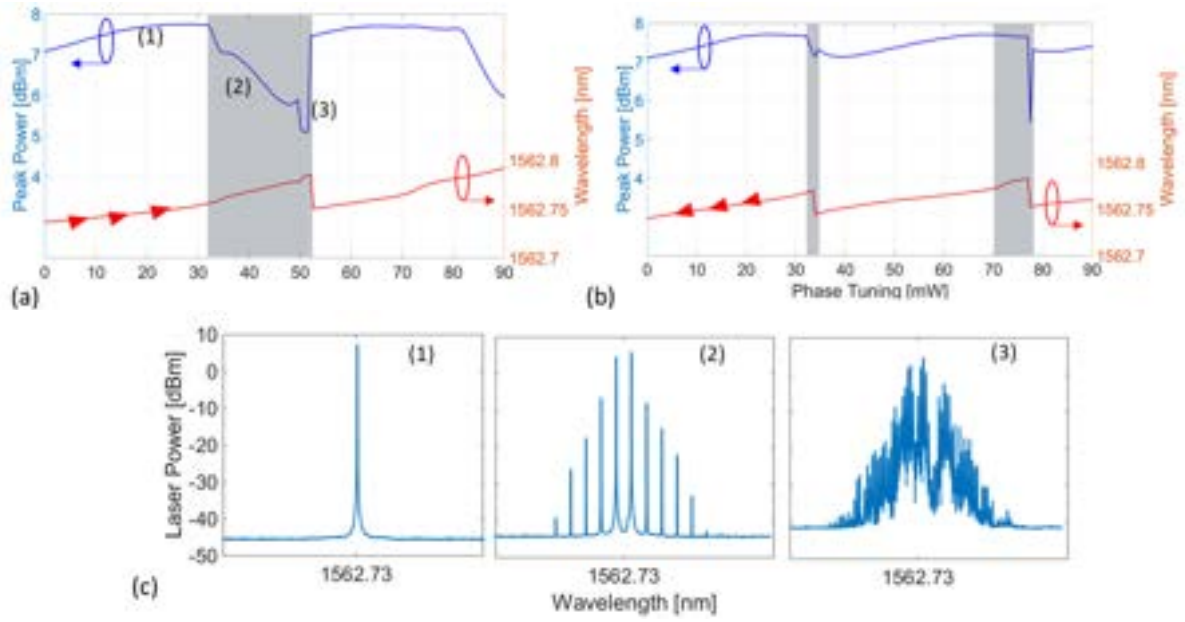

Figure 6.6 At a fixed gain of 200mA, the laser encounters different multi-mode regimes, which are shaded, depending on whether the longitudinal modes are (a) red-shifted with increasing power to the phase section, or (b) blue-shifted. In the multimode regions (c), the laser can enter a mode-locked state (2) or a chaotic state (3).

6.3.2 *Frequency and RIN noise*

The frequency noise of the lasers is measured using a Sycatus A0040A optical noise analyzer and Keysight X-series signal analyzer [6]. Despite using battery powered current sources isolated from power lines, there is still significant contribution to the measurement from other sources in the 10kHz to 10MHz range. Furthermore, within the 20 MHz limit of the tool's measurable frequency range, the white-noise limited frequency noise has not fully reached its flat level (i.e. the fundamental/Lorentzian linewidth). The spectra shown in *Figure 6.7(a)* and (b) indicate white-noise limited frequency noise of lower than 350 Hz^2/Hz for the E-DBR laser, and lower than 170 Hz^2/Hz for the RAE-DBR laser, corresponding to less than 1.1 kHz and 500 Hz Lorentzian linewidths after multiplying by π. A comparison of E-DBR lasers with different grating strengths is shown in *Table 2.1*. The correlation between grating strength and linewidth and optical power is clear for the E-DBR. The grating strength does not play a large role in determining the RAE-DBR's linewidth, as expected due to the ring being much more narrowband than the grating. A straightforward improvement is to decrease the grating strength for the RAE-DBR, which would lead to higher output power.

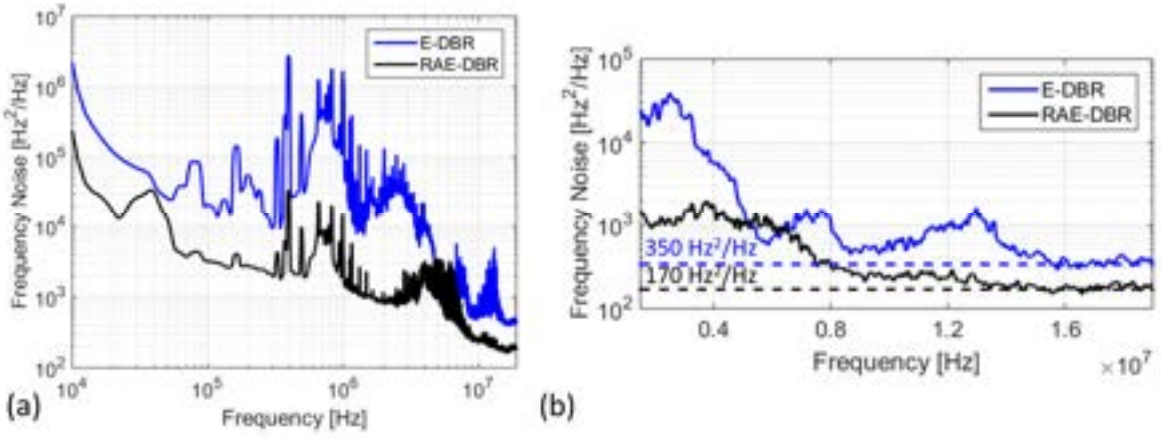

Figure 6.7 Frequency noise spectra for the E-DBR and RAE-DBR lasers on (a) logarithmic and (b) linear frequency scales. The analyzer is limited to 20MHz, which may not be sufficient to see the white noise floor of the FN.

Table 6.1 Comparison of Lorentzian linewidth of E-DBR and RAE-DBR lasers

Laser Type	*Grating Length [mm]*	*Designed κL*	*Ring Power Coupling*	*Ring Radius [μm]*	*Power @ 400mA [mW]*	*Linewidth [kHz]*
E-DBR	15	0.375	-	-	37	1.1
E-DBR	15	0.75	-	-	18	1.5
E-DBR	15	1.05	-	-	12	4.0
E-DBR	15	3	-	-	3.1	10.0
RAE-DBR	10	1	0.04	600	4.8	0.5
RAE-DBR	10	2	0.04	600	2.1	0.6

The relative intensity noise (RIN) spectra measured for the E-DBR laser at several drive currents are shown in *Figure 6.8*. There are several peaks in the 0-10 GHz range, which are attributed to mode interactions between the lasing mode and non-lasing cavity modes. This may be further suppressed by optimizing the phase control at each drive current, as was demonstrated in the LIV. Grating apodization could suppress these peaks by improving the SMSR. For 200 mA drive current, the RIN is measured to be less than -150 dB/Hz apart from the dominant peak at 7 GHz.

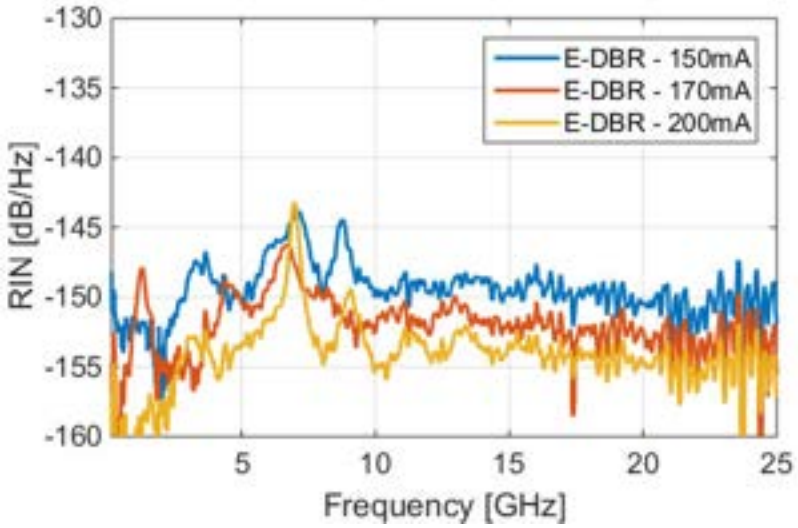

Figure 6.8 Measured Relative Intensity Noise (RIN) of the E-DBR with κL = 0.375 at different drive currents.

6.4 Summary

In this chapter, we have demonstrated an extended DBR lasers with <1 kHz linewidth and over 37 mW of output power. Adding a high-Q ring into the cavity further reduces the linewidth to 500 Hz, however, with a lower output power of 4.8 mW. The narrow linewidth and excellent single-mode stability are only achievable by using the ultralow loss silicon waveguides with extremely low κ gratings to form a 15 mm long extended Bragg reflector.

References

[1] D. T. Spencer, M. Davenport, S. Srinivasan, J. Khurgin, P. A. Morton, and J. E. Bowers, "Low kappa, narrow bandwidth Si_3N_4 Bragg gratings," *Opt. Express*, vol. 23, no. 23, p. 30329, 2015.

[2] M. Tran, D. Huang, T. Komljenovic, J. Peters, A. Malik, and J. Bowers, "Ultra-Low-Loss Silicon Waveguides for Heterogeneously Integrated Silicon/III-V Photonics," *Appl. Sci.*, vol. 8, no. 7, p. 1139, 2018.

[3] M. L. Davenport, S. Skendzic, N. Volet, J. C. Hulme, M. J. R. Heck, and J. E. Bowers, "Heterogeneous silicon/III-V semiconductor optical amplifiers," *IEEE J. Sel. Top. Quantum Electron.*, vol. 22, no. 6, 2016.

[4] P. Bardella and I. Montrosset, "Analysis of self-pulsating three-section DBR lasers," *IEEE J. Sel. Top. Quantum Electron.*, vol. 11, no. 2, pp. 361–366, 2005.

[5] X. Pan, H. Olesen, and B. Tromborg, "A Theoretical Model of Multielectrode DBR Lasers," *IEEE J. Quantum Electron.*, vol. 24, no. 12, pp. 2423–2432, 1988.

[6] "Optical Noise Analyzer." [Online]. Available: http://www.sycatus.com/en/products/ona/. [Accessed: 17-Mar-2019].

Chapter 7. Heterogeneous Si/III-V PIC for Optical Gyroscopes

In this chapter, we showcase a successful application of photonic integrated circuits (PICs) built based upon the heterogeneous Si/III-V platform described in Chapter 1. We will first describe the PIC design, fabrication and demonstrate a gyroscope operated with the integrated chip. The chip is, to the best of our knowledge, the first fully integrated optical driver (IOD) chip that comprises all optical active components and passive components needed for driving an interferometric optical gyroscope (except the sensing coil). We will then look closer into direct frequency modulation of laser sources as a power-efficient way to further improve the gyroscope's noise performance.

7.1 Fiber-optic gyroscopes

The interferometric fiber-optic gyroscope (IFOG) is a fascinating sensing apparatus, capable of measuring miniscule phase shifts on the order of 10^{-15}; which is made possible by careful optimization of individual components and utilizing reciprocity [1]. The performance of such units is state-of-the-art, but modern IFOGs still suffer from size, weight, power and cost (SWaP-C) limitations due to being based on discrete optical components. Each discrete component is normally packaged with a fiber pigtail to form the Sagnac reciprocal interferometer optical circuit leading to larger size and increased cost. The SWaP-C limitation is the reason why many low-cost applications utilize micro-electro-mechanical systems (MEMS) based gyroscopes, despite inferior performance and limitations. One of key limitations of MEMS based gyroscopes is the increased sensitivity to vibrations and shock. Optical gyroscopes, on the other hand, are almost completely insensitive to vibration and shock, and to electromagnetic interference, which is very important in today's complex

environments packed with electronic devices. The robustness would only increase with further integration. For that motivation, miniaturization of optical gyroscopes has been an active research topic for many years on various waveguide platforms [2]–[6].

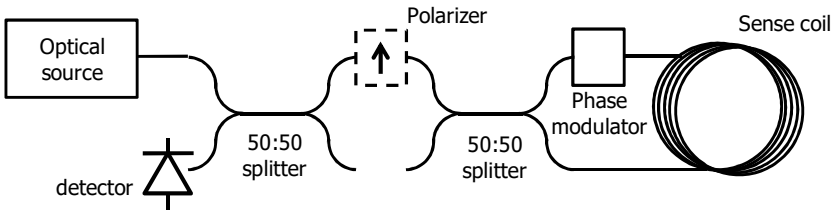

Figure 7.1 Minimum configuration of a reciprocal optical Sagnac interferometer, consisting of an optical source, optical power splitter, photodetector, phase modulator, polarizer (optional) and a sensing coil. ©OSA 2016

An IFOG consists of two main parts: front-end and sensing coil, as shown in *Figure 7.1*. The front-end commonly consists of an optical source, one or more detectors, two splitters and two phase-shifters. Currently only the last segment comprising one splitter and two phase-shifters is integrated in a LiNbO3 platform, while source and detectors are separate components. The sensing coil is usually optimized for gyroscope performance (small size, high reciprocity) by optimizing the cladding thickness and advanced fiber winding techniques to cancel out non-reciprocal noise and drift [7]. Depending on the specific implementation, the coil can be single-mode (SM) fiber or polarization-maintaining (PM) single-mode fiber. PM fiber generally has better performance, but at an increased cost. Integration of an IFOG would bring a huge SWaP-C improvement and would allow deployment of superior rotation sensing instrumentations in many areas where it was currently unfeasible.

7.2 Design of the integrated optical drivers for optical gyroscopes

The schematic layout of the IOD chip is illustrated in *Figure 7.2(a)*. The light source is a multi-mode Fabry-Perot laser. Utilization of a laser significantly reduces the power

consumption over, for example, a super luminescent light emitting diode (SLED), as at above threshold, most of the current is converted to photons. Three photodiodes are used to detect the Sagnac signal and provide a monitor for the laser output. Corrections to the read-out of the gyroscope or stabilization of the laser power by an electrical feedback loop are straightforward to implement since the control and feedback signals are available in the IOD. The phase modulators are laid out in a push-pull configuration to reduce the half-wave voltage. The two power splitters should ideally have 50% splitting ratio to reduce the backscattering noise and maximize the intensity of the Sagnac signal [8]. We address our coupler design in detail in later sections. The two output waveguides are inversely tapered for mode matching with optical fibers. We intentionally bring the two output waveguides to the opposite sides of the chip; it is expected that having uneven distances from the 3-dB splitters to the waveguide facets (ideally the difference between these distances should be larger than coherence length of the light source [1]) would help reduce the coherent back-reflection noise induced by the reflections at the chip-fiber interfaces. Details of all the components (*i.e.* lasers, photodiodes and phase modulators, adiabatic couplers, mode size converters) were provided in the previous sections.

When operating in a gyroscope system, the phase modulator will be modulated at the proper frequency of the gyroscope, which is strictly related to the length of the sensing coil by equation $f_p = \frac{\pi c}{n_{eff} L}$ where c is the speed of light in vacuum, n_{eff} is the effective index of the propagation mode and L is the length of the coil. Depending on the performance requirements and applications, the length of the sensing coil may vary from tens of meters to several kilometers, resulting in the proper frequency range from hundreds of kHz to hundreds of MHz level. Different modulation signals (sinusoidal, squared, triangle wave, etc.) can be used. To

cover all potential fiber lengths with sufficient margin, the modulators and the detectors are required to have bandwidths in the range of 1 GHz.

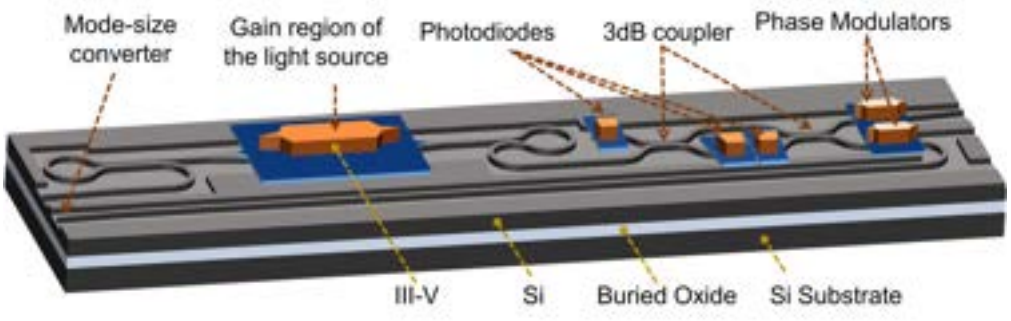

Figure 7.2 Three-dimensional schematic (not to scale) of the integrated optical driver (IOD) for fiber optic gyroscopes. ©OSA 2017

7.3 PIC-driven optical gyroscope operation

A microscopic image of a fabricated IOD chip is shown in *Figure 7.3* with break-downs of each component. The chip is 9 mm x 0.5 mm in size. A bar that comprises 12 individual IODs is put next to a US quarter dollar for comparison.

To test the functionality of the IOD chip, we formed an open-loop interferometric optical gyroscope by connecting the chip to a 180 m long polarization maintaining (PM) fiber coil with bench-top read-out electronics illustrated in *Figure 7.4(a)*. The fibers were aligned to the mode size converters of the IOD by using two 3-axis stages and electrical contacts to the chip were made by using RF probes (shown in *Figure 7.4(b)*). The chip was kept at room temperature by a thermoelectric cooler underneath the stage. The entire alignment setup was placed on an optical bench while the fiber coil was put on a separate rotation table; hence, it is possible to apply the rotation only to the sensing coil without disturbing the optical and electrical alignments on the chip. A 20dB RF amplifier was used to boost the interference

signal at the first photodiode on the IOD. The signal was analyzed with an electrical spectrum analyzer (ESA).

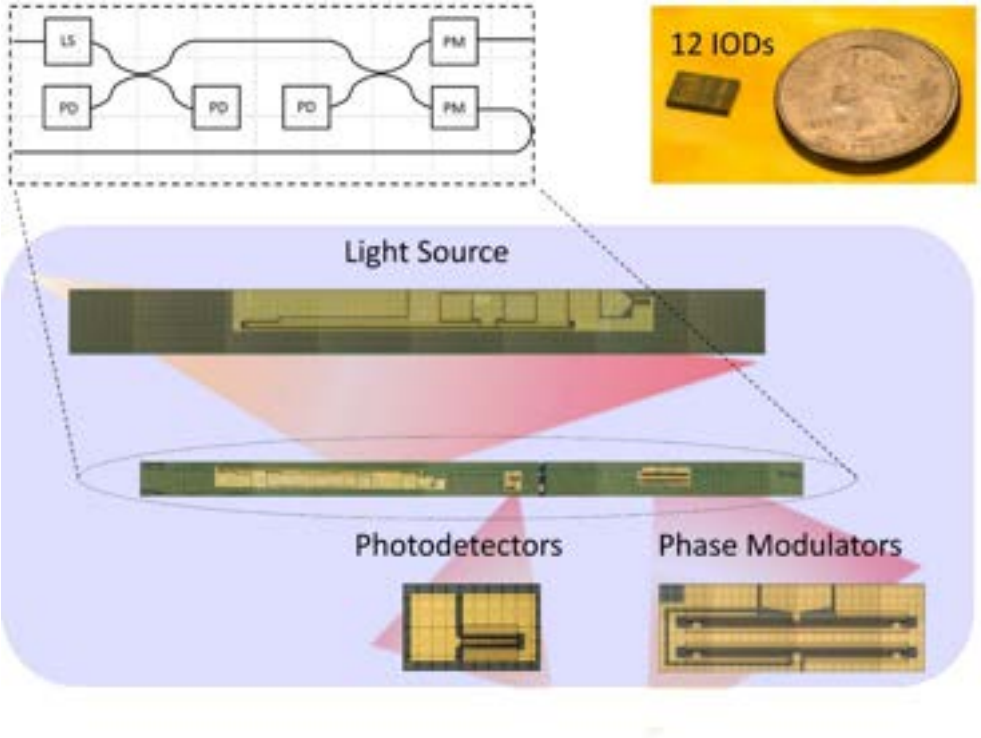

Figure 7.3 Picture of a fabricated IOD chip with close-up images of its components. LS: Light Source, PD: Photodiode, PM: Phase Modulator. A set of 12 devices is placed next to a US quarter coin for size comparison. ©OSA 2017

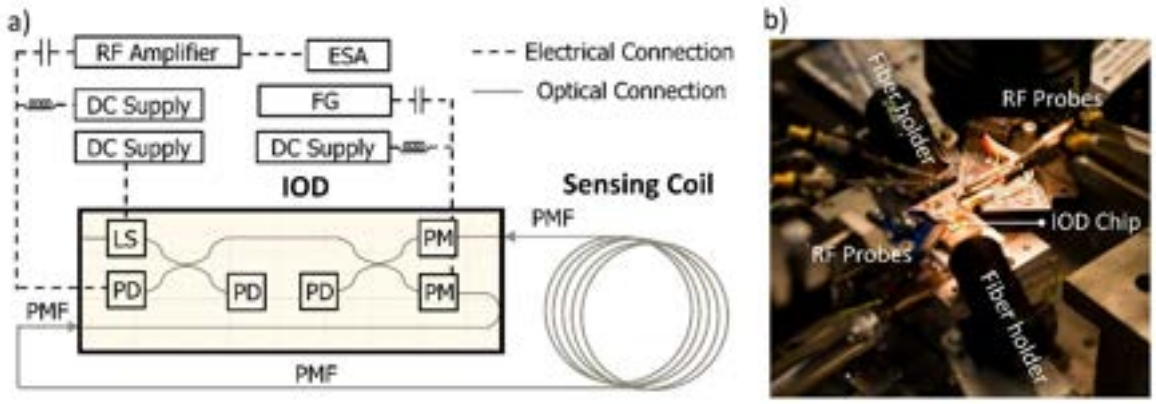

Figure 7.4 (a) Schematic of the interferometric optical gyroscope driven by the IOD chip. The PM fiber coil is 180 m long with a diameter of 20 cm. LS: Light Source, PD: Photodiode, PM:

Phase Modulator, PMF: Polarization Maintaining Fiber, ESA: Electrical Spectrum Analyzer, FG: Function Generator. (b) Photograph of the electrical and optical alignment onto the IOD chip. ©OSA 2017

In operation of the IOD, the DC current to the laser was set at 400 mA, well above the threshold current and near the maximum output power point. The phase modulators and photodiodes were operated in reverse bias regime. The total photo-current received at the detection photodiode was 8 μA, corresponding to 11.4 μW optical power. A sinusoidal wave was applied to the phase modulator at the proper frequency of $f_p = 560\ kHz$ which is governed by the length of the fiber coil [1]. The modulation amplitude on the phase modulator was set to 250 mV, corresponding to modulation depth of about $\phi_b = 0.1\ rad$. The rotation induced Sagnac phase shift is $\Delta\phi_R = \frac{8\pi LD}{\lambda c}\frac{\pi}{180}\Omega_R$ where $L = 180\ m$ is the length, $D = 0.2\ m$ is the diameter of the coil, $\lambda = 1.57\ \mu m$ is the mean-wavelength of the multimode laser and $\Omega_R\ (^\circ/s)$ is the rotation rate. Due to the sinusoidal modulation of the phase modulator, the gyroscope output voltage is given by

$$V(\Omega) = I_0 R_{ESA} G J_1(\phi_b)\sin\Delta\phi_R \qquad (7.18)$$

where $I_0 = 8\mu A$ is the detected DC photocurrent, $R_{ESA} = 50\ \Omega$ is the resistance of the ESA, *G=10* is the amplification of the RF amplifier and J_1 (where $J_1(\phi_b) = 0.1$) is the Bessel function of the first order at the phase modulation depth. Using the small angle approximation for the sine function, we can estimate $\mathrm{V}(\Omega) \approx 6.70 \times 10^{-6}\Omega$; in other words, the scale factor of the gyroscope is expected to be $6.70\ \mu V/^\circ/s$.

We carried out the gyroscope measurement by sweeping the rotation rates in clockwise (CW) and counter-clockwise (CCW) directions alternately and recorded the voltage at the

modulation frequency on the ESA. The output signal voltage versus the rotation rate is plotted in *Figure 4.3(a)*. It shows that the gyroscope output was linearly proportional to the applied rotation rate with a scale factor of $6.28\ \mu V/°/s$. This is in good agreement with the above calculation; the measured value is slightly smaller possibly due to some signal losses along the RF connections in the setup.

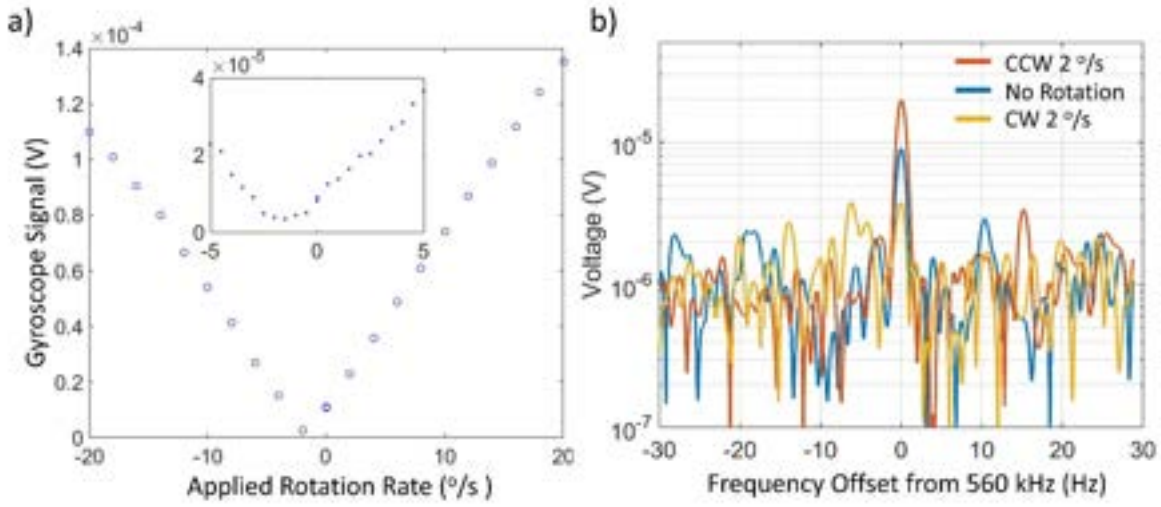

Figure 7.5 (a) IOD driven gyroscope's signal versus the rotation rate. Inset shows a zoom-in of small range of the rotation rate. (b) The spectra on the ESA of CW and CCW 2 °/s and zero-rotation. The plot is centered at the 560 kHz modulation frequency with the resolution width of 1 Hz. ©OSA 2017

We can observe that there is an offset of roughly $2\ °/s$ in the rotation measurement. As revealed in the ESA spectra shown in *Figure 4.3 (b)*, when no rotation was applied, there still appeared at the modulation frequency a peak of $8.5\ \mu V$ of an "offset signal" that is not caused by Sagnac phase shift. The possible causes for this offset could be electromagnetic interference (EMI) between components on the integrated circuit chip or phase error caused by residual amplitude modulation of the phase modulator [9]. Earth rotation and magnetic field induced nonreciprocal phase shift could have also contributed a fraction to the offset.

Nonetheless, the offset caused by these effects can be calibrated out to correct the gyroscope's read-out in practice.

The minimum measurable rotation rate in this current work is limited to about $3.39\ \mu V$ or equivalent $0.53°/s$ rotation rate (*Figure 4.3(a)* inset). It is mainly limited by a low signal to noise ratio (S/N), as can be seen on the spectrum of CW $2°/s$ rotation in Fig. 16(b). Larger S/N is necessary for improving the gyroscope sensitivity. To enhance the signal amplitude, we can increase the scale factor in equation *(3.8))* by choosing the optimal modulation depth for the phase modulator to maximize $J_1(\phi_b)$ and by having larger gain A in the RF amplifier. To suppress the noise floor, we will show in the next section that frequency modulating the laser could be extremely helpful [10]. Combining these methods, we can expect to obtain at least two order of magnitude improvement on the sensitivity of the gyroscope.

7.4 Frequency Modulated Lasers for Optical Gyroscopes

Although using a multimode laser as above is preferred in term of power efficiency compared to a broadband source thanks to the high quantum efficiency upon lasing, it has been known to be disadvantageous for a gyroscope's noise performance due to coherent interference between various parasitic waves generated in the system due to back reflections, backscattering, and Kerr nonlinearity [1], [11]. It has been found that sources with short coherence lengths significantly suppress those interfering processes, which in turn lead to reduced noise and improved system performance [1]. IFOGs have therefore generally utilized super-luminescent diodes (SLED) or erbium-doped fiber (EDF) based sources for medium and high-performance gyroscopes, and sometimes Fabry-Pérot (FP) lasers biased below threshold as a low-cost solution. EDF based sources generally offer the best performance, primarily due to higher temperature stability, but at the same time are more costly and harder

to package. Recently, the use of single-frequency lasers with high-spectral purity has been considered as an alternative to broadband sources [12]. A single-frequency laser source does not suffer from excess noise and can achieve higher scale factor stability due to a greater degree of wavelength stability. The authors show that through a careful selection of laser coherence (narrow-linewidth) and adoption of the push-pull phase modulation technique (common in most modern IFOG setups), a better (lower) resolution limit can be achieved, although at the expense of higher drift.

As we showed in the previous section, the gyroscopes driven by our integrated lasers are quite limited in sensitivity. Since making broadband on-chip to meet the desired SWaP+C specs is not feasible, we prefer to use laser diodes as the light source. Here, we explore the use of high-speed frequency modulated (FM) lasers in interferometric optical gyroscopes. We show that frequency modulation of both single-frequency and FP lasers is a useful technique to control source coherence length and improve gyroscope performance simultaneously. FM modulation in conjunction with gyroscopes has received relatively little attention. Cutler et al. suggested that a fast change in source frequency can reduce the errors due to Rayleigh scattering [13] and Culshaw et al. investigated heterodyne detection of FM modulated laser light in an IFOG primarily to overcome 1/f noise problems [14]. More recently Blin et al. investigated frequency-modulated lasers in IFOGs and concluded that fast sweeping of laser source frequencies can reduce backscatter noise [15]. Here we go a step further, showing that more complex FM modulation signals can result in even better overall gyro system performance. We relate the FM modulated signals to their corresponding coherence functions and show that by optimizing the source coherence functions we can clearly improve both the angular random walk (ARW) and the bias drift performance.

7.4.1 *Controlling the coherence lengths of laser sources*

We study both single-frequency and FP lasers for use in a fully-integrated laser gyroscope. To explain the improvements in interferometric optic gyroscope performance through the application of FM modulation, we turn to the coherence functions, C(τ), of the sources.

To simplify the measurements of coherence functions of various ranges (from ~10 meters down to single-digit centimeters), we employed a high-resolution optical spectrum analyzer (OSA) with 20 MHz resolution, and utilized the fact that the coherence (or auto-correlation) function is the inverse Fourier transform of the centered intensity spectrum [1]. The method applied here has some limitations, such as the resolution limitation of our OSA and the omission of potential spectral asymmetry, but nevertheless serves to illustrate the method through which the complex FM modulation signals reduce the backscatter related noise and improve gyroscope performance.

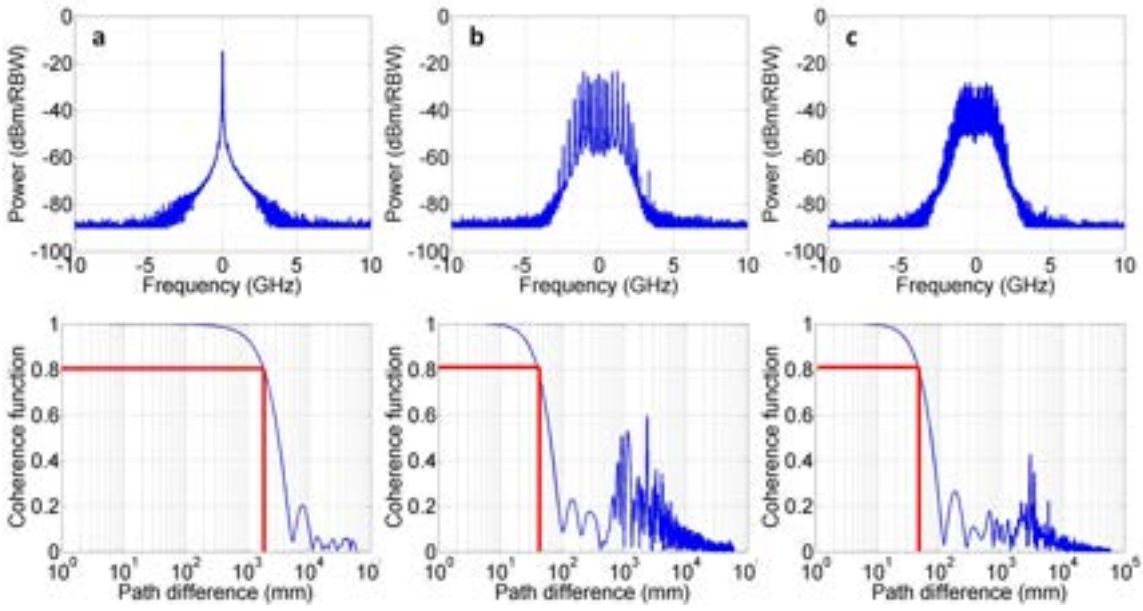

Figure 7.6 Measured spectra and corresponding coherence function for DFB laser. The three rows correspond to: (a) continuous wave (coherence length Lc = 1871 mm, underestimated due to measurement method) (b) single-tone modulation (300 MHz, Lc = 42 mm) (c) two-tone

modulation (300 MHz and 99 MHz, Lc = 48 mm). By applying fast FM modulation, the coherence length can be reduced by approximately two orders of magnitude. ©OSA 2016

We begin with a commercially available DFB laser. The measurement of the coherence length of the unmodulated DFB laser is limited by the OSA, as the linewidth is specified as narrower than 20 MHz, so its coherence length is under-estimated. We compare this coherence length to the resulting coherence lengths when the laser is modulated by a single frequency (300 MHz) tone and when we modulate the laser with two frequencies whose ratio is not an integer value (300 MHz and 99 MHz). The corresponding spectra and coherence functions are shown in *Figure 7.6*. We can see that the modulation allows for a reduction of coherence length by a minimum of two orders of magnitude, as the continuous wave laser coherence is under-estimated as described above. In the case of single-tone modulation, there is a coherence peak around 1 m, which corresponds to the applied 300 MHz signal. By applying two-tone modulation this coherence peak is largely suppressed, further improving the gyroscope performance as shown in the next section. A single-tone modulation can be considered as a laser frequency sweep similar to the ramp used in [16], and we show that more elaborate modulation signals can further improve performance. In theory, more complex modulation signals, such as pseudo-random sequences, could even further reduce the coherence function peaks at longer path differences, but care has to be taken that this added modulation does not introduce noise at frequencies close to the gyroscope signal (the sensing coil proper frequency and its harmonics).

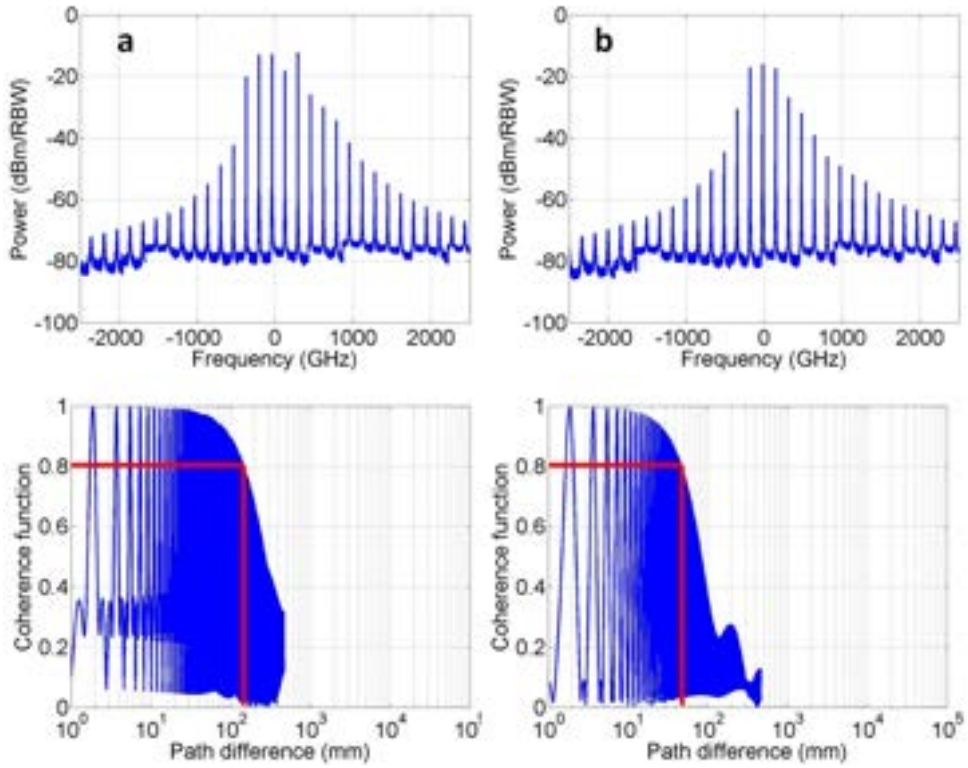

Figure 7.7 Measured spectra and corresponding coherence function for FP laser. The two rows correspond to: (a) continuous wave (coherence length Lc = 145 mm) (b) single-tone modulation (300 MHz, Lc = 47 mm). ©OSA 2016

Fabry-Pérot lasers are another choice for an integrated gyroscope, and as a first guess, one might intuitively guess that multiple peaks in the lasing spectrum will further reduce the source coherence, and thus consequently further improve eventual gyroscope performance. Measured spectra and corresponding coherence functions of a typical commercial FP laser are shown in *Figure 7.7*. The coherence function for a continuous wave FP laser shows a number of coherence peaks separated by the longitudinal mode spacing and an envelope whose path distance is determined by the spectral linewidths of the individual modes. These FP results suffer from under-sampling, as the high-resolution OSA has a limited number of data points it can take, and we have to take much wider traces to capture the majority of the longitudinal

modes. Unfortunately, stitching together multiple measurements with a reduced span resulted in additional artifacts, further obscuring the results. The coherence function is truncated around 500 mm due to the large sample separation in the frequency domain, so the coherence peak that should correspond to 300 MHz modulation is not visible. Nevertheless, it is obvious that the coherence function is more complex and has interlocked minimums and maximums. This will result in increased bias drift due to small changes within the sense coil due to *e.g.* temperature changes as the backscatter signature drifts between the minima and maxima of the coherence function. Mode-hopping can also influence gyroscope performance due to the resulting change of mean wavelength. Such an effect would manifest itself primarily as a scale factor drift. By applying FM modulation to an FP laser, one can reduce the path length difference of the envelope, similar to reducing the coherence of the DFB laser. The envelope reduces due to an increase in linewidth of the individual modes, but the coherence peaks are still present potentially resulting in bias drift. Direct modulation can hardly suppress the coherence peaks as they are dictated by cavity length and usually separated by 50 to 150 GHz in common FP lasers. A possible route to reduce such peaks could be to design a laser with multiple gain sections and higher frequency deviation efficiency [17]. This complex coherence function, together with a higher RIN and greater degree of thermal drift, indicate that the performance of a gyroscope utilizing a FM modulated multimode laser will be worse than one that utilizes a FM modulated single mode laser.

7.4.2 *Interferometric fiber-optic gyroscope performance evaluation*

The performance of the various above-mentioned optical sources was quantified with a fiber-based optical gyroscope (*Figure 7.8*). The use of a circulator prevented feedback to the optical sources, and as we noted above, the resulting effect of such feedback is currently under study

and will be reported in a future publication. We implemented a simplified configuration, containing only a single commercial LiNbO3-based phase modulator. An EDF based broadband source was included as a baseline comparison. The lock-in amplifier had a 30 ms integration time with a 12 dB/octave roll-off corresponding to ~4 Hz bandwidth. The signal from the lock-in was sampled at 50 Hz.

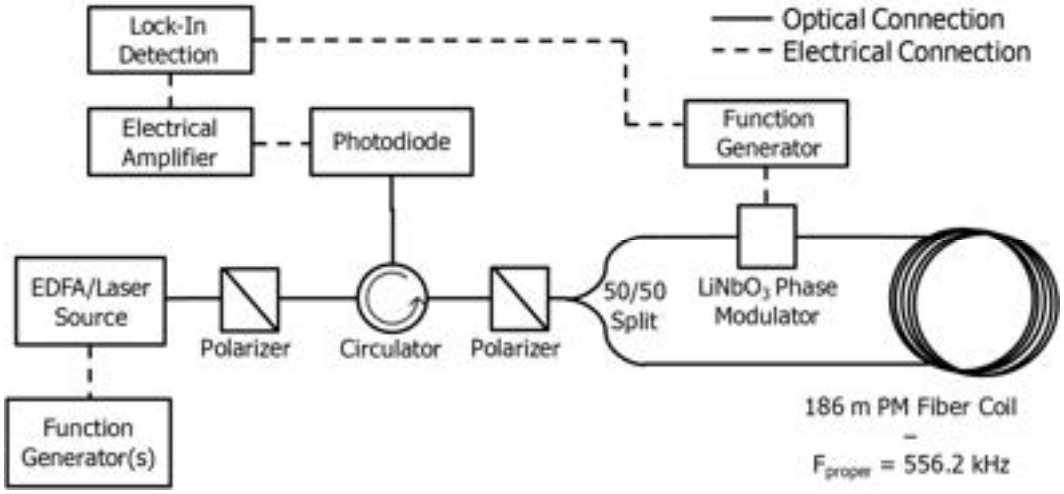

Figure 7.8 Schematic of in-house assembled fiber-based optical gyroscope. All fibers after the first polarizer are PM and input polarization are optimized for maximum power at the photodiode. Each fiber component is connected to the next by an FC/APC. ©OSA 2016

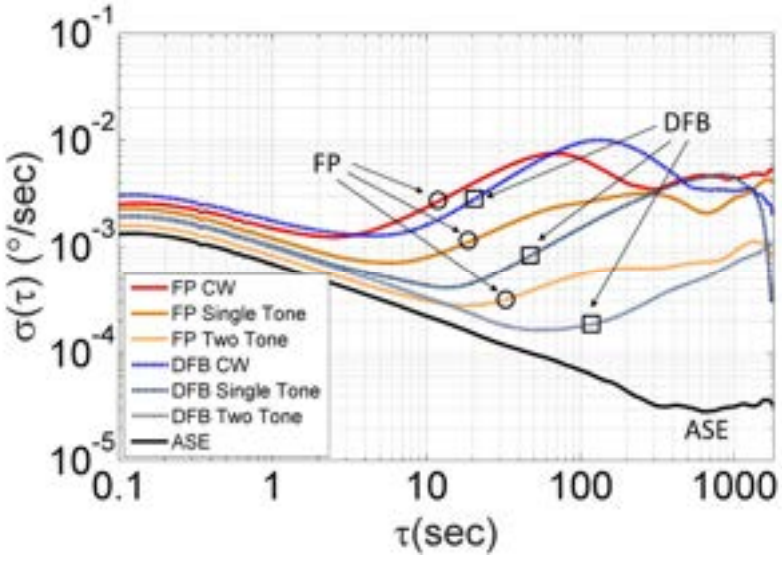

Figure 7.9 Allan deviation measurements for each optical source at CW, single, and two-tone modulation. FM modulation improves both the ARW and bias stability in all cases. ©OSA 2016

Measurements of Allan deviation were performed over a period of one hour, with the results plotted in *Figure 7.9*. The results are each converted to °/s by measuring the gyroscope scale factor using a rotation table. We have included the best results for each configuration to illustrate that FM modulated lasers can be a serious candidate for an optical source in a fully-integrated interferometric gyroscope. We should point out that the end performance is sensitive to external factors such as temperature drift. From *Figure 7.9*, we can see that the laser sources generally provide an ARW that is comparable to the ASE source, but suffer from much higher bias drift, which is in agreement with previous studies. Additionally, DFB lasers outperform FP lasers, which is consistent with our predictions from the previous section. FM modulation improves performance in all cases, and the two-tone modulation scheme further improves both the ARW and bias drift compared to the single-tone modulation scheme. Key performance numbers are summarized in *Table 7.1*. In all cases we applied direct laser modulation, but external modulation could also be utilized to the same effect of controlling coherence.

Table 7.1 Key performance indicators for ASE and laser-based gyroscope measurements. FM modulation improves both the ARW and bias instability. ©OSA 2016

Source Type	*Laser Drive Frequency (MHz)*	*Mean Detector Power (dBm)*	*ARW* $(°/\sqrt{hr})$	*Bias instability* $(°/hr)$
FP Laser	CW	-13.33	0.09	4.48
FP Laser	300	-13.37	0.072	2.576
FP Laser	300, 99	-13.33	0.05	1.015

DFB Laser	CW	-12.40	0.106	4.624
DFB Laser	300	-12.37	0.061	1.527
DFB Laser	300, 99	-12.40	0.059	0.602
ASE	-	-12.96	0.041	0.102

7.5 Summary

In this chapter, we have presented the design, fabrication and characterization of an integrated optical driver (IOD) for interferometric optical gyroscopes. The chip was made using the optimized heterogeneous Si/III-V photonic integration platform developed throughout the work in this thesis. The fabricated IOD contains a Fabry-Perot multi-mode laser, photodiodes, phase modulators and adiabatic 3-dB splitters on a single chip within a 0.5 mm x 9 mm area. We have succeeded in demonstrating, for the first time, a working IFOG driven by a fully integrated chip, although the initial device still showed a relatively limited sensitivity.

To investigate the pathway for a suitable method to improve the noise performance of the laser-driven optical gyroscopes, we have explored the use of high-speed frequency modulated (FM) lasers in interferometric optical gyroscopes and showed that frequency modulation of both single-frequency and multimode lasers is a valuable technique to control source coherence length, and as a result improve gyroscope performance. Utilizing an in-house fiber-based gyroscope test bed, we showed that FM modulation improves both angular random walk (ARW) and bias drift. We related this improvement in performance to coherence length reduction and showed that more complex FM modulation signals can further improve gyroscope performance. When directly comparing typical multimode FP and single frequency lasers, we showed that single frequency lasers offer superior performance. These are important results for future directions.

References

[1] H. C. Lefevre, *The Fiber-Optic Gyroscope*, Second Edi. Artec House, 2014.

[2] M. A. Tran, T. Komljenovic, J. C. Hulme, M. Kennedy, D. J. Blumenthal, and J. E. Bowers, "Integrated optical driver for interferometric optical gyroscopes," *Opt. Express*, vol. 25, no. 4, p. 3826, 2017.

[3] S. Gundavarapu *et al.*, "Interferometric Optical Gyroscope Based on an Integrated Si3N4 Low-Loss Waveguide Coil," *J. Light. Technol.*, 2018.

[4] F. D. Olio, T. Tatoli, and C. Ciminelli, "Recent advances in miniaturized optical gyroscopes," vol. 14013, 2014.

[5] J. Li, M.-G. Suh, and K. Vahala, "Microresonator Brillouin gyroscope," *Optica*, vol. 4, no. 3, p. 346, 2017.

[6] W. Liang *et al.*, "Resonant microphotonic gyroscope," *Optica*, 2017.

[7] C. M. Lofts, "Investigation of the effects of temporal thermal gradients in fiber optic gyroscope sensing coils," *Opt. Eng.*, 2006.

[8] J. M. Mackintosh and B. Culshaw, "Analysis and Observation of Coupling Ratio Dependence of Rayleigh Backscattering Noise in a Fiber Optic Gyroscope," *J. Light. Technol.*, 1989.

[9] E. Kiesel, "Impact Of Modulation Induced Signal Instabilities On Fiber Gyro Performance," in *Fiber Optic and Laser Sensors V*, 2012.

[10] T. Komljenovic, M. A. Tran, M. Belt, S. Gundavarapu, D. J. Blumenthal, and J. E. Bowers, "Frequency modulated lasers for interferometric optical gyroscopes," *Opt. Lett.*, vol. 41, no. 8, p. 1773, 2016.

[11] R. Bergh, H. Lefevre, and H. Shaw, "An overview of fiber-optic gyroscopes," *J. Light.*

Technol., vol. 2, no. 2, pp. 91–107, Apr. 1984.

[12] S. W. Lloyd, S. Fan, and M. J. F. Digonnet, "Experimental observation of low noise and low drift in a laser-driven fiber optic gyroscope," *J. Light. Technol.*, vol. 31, no. 13, pp. 2079–2085, 2013.

[13] C. C. Cutler, S. a Newton, and H. J. Shaw, "Limitation of rotation sensing by scattering.," *Opt. Lett.*, vol. 5, no. 11, pp. 488–490, 1980.

[14] B. Culshaw and I. Giles, "Frequency modulated heterodyne optical fiber Sagnac interferometer," *IEEE J. Quantum Electron.*, vol. 18, no. 4, pp. 690–693, 1982.

[15] S. Blin, M. J. F. Digonnet, G. S. Kino, and L. Fellow, "Noise Analysis of an Air-Core Fiber Optic Gyroscope," vol. 19, no. 19, pp. 1520–1522, 2007.

[16] S. Blin, M. J. F. Digonnet, and G. S. Kino, "Fiber-optic gyroscope operated with a frequency-modulated laser</title>," vol. 7004, p. 70044X–70044X–4, 2008.

[17] J. E. Bowers, R. S. Tucker, and C. A. Burrus, "6 GHz DIRECT FREQUENCY MODULATION OF CLEAVED-COUPLED-CAVITY CHANNELED-SUBSTRATE BURIED-HETEROSTRUCTURE LASERS.," *IEEE J. Quantum Electron.*, vol. QE-20, no. 11, pp. 1230–1232, 1984.

Chapter 8. Summary and future work

8.1 Thesis summary

This thesis described the path we have pursued to successfully established a significant advancement in the state-of-the-art of low frequency noise laser diodes. Several new records for narrow linewidth laser diodes have been continuously set (and broken). Some of the key achievements in the scope of this dissertation include:

- Demonstration of tunable lasers of sub-mm^2 size, 2 kHz fundamental linewidth, 40 nm wavelength tuning range and 12 mW output power (chapter 3).
- Demonstration of ultralow loss silicon waveguides that are compatible to the Si/III-V heterogeneous integration platform. Meter-scale delay lines, million-Q resonators and tens of picometer bandwidth grating filters are accomplished (chapter 4)
- Demonstration of tunable lasers of sub-cm^2 size, 140 Hz fundamental linewidth, 120 nm wavelength tuning range (1484 nm – 1604 nm) and 3 mW output power (chapter 5).
- Demonstration of an Extended-DBR laser with <1 kHz linewidth and 37 mW output power at 1562 nm wavelength (chapter 6)
- Demonstration of a Ring-Assisted Extended-DBR laser with < 500 Hz linewidth and 4.8 mW output power at 1562 nm wavelength (chapter 6).

This unprecedented laser performance is the direct results of the successful integration of the newly developed ultralow loss waveguides into the optimized Si/III-V heterogeneous photonic platform. The low loss silicon waveguides have expanded our access to high Q narrow band resonant cavity designs, which are essential for low noise lasers. Compared with other foundry compatible low-loss platforms such as silicon, silicon nitride, and indium phosphide in *Table 8.1*, the ultralow loss silicon platform benefits from high group index

(longer effective cavity length) and high power handling due to large modal volume. The use of a thick (500 nm) silicon layer has also been demonstrated to support high linearity heterogeneous silicon/III-V modulators [1] with high operating power [2], and high bandwidth photodetectors [3]. The realization of high performing laser demonstrated in this thesis have added a lot of value into the fast-growing heterogeneous Si/III-V platform [4].

Table 8.1 Comparison of foundry -compatible low loss single mode waveguide platforms

Platform	*Optical loss per unit length (dB/cm)*	*Min. Bend Radius (μm)*	*Group Index*	*Loss per unit time (dB/ns)*
ULL SOI rib (500nm) [5]	0.16	600	3.61	1.33
"Thin" SOI (220nm) [6]	0.5	35	3.82	3.93
"Thick" SOI rib (>1 μm) [7]	0.027	2400	3.64	0.22
ULL Silicon Nitride [8]	0.007	10000	1.48	0.14
TriPleX Silicon Nitride [9]	0.1	100	1.7	1.76
InP [10]	0.34	11600	3.81	2.68

In *Figure 8.1*, we compare the linewidth of widely-tunable lasers that have been reported in literature as of the time when this thesis is being written, including the results accomplished in this thesis. The best result obtained in this work is holding the world record for ultralow noise among all kinds of chip-scale electrically pumped lasers, including multi-chip assembled lasers. Although it is clear from *Table 8.1* that the silicon is not the best material to make ultralow loss waveguides, silicon/III-V heterogeneous lasers still have the best performances thanks to the benefits from the full integration, *e.g.* passive-active transition with low loss and low parasitic reflection, aside from the huge economic advantages resulted from the scalability and low-cost.

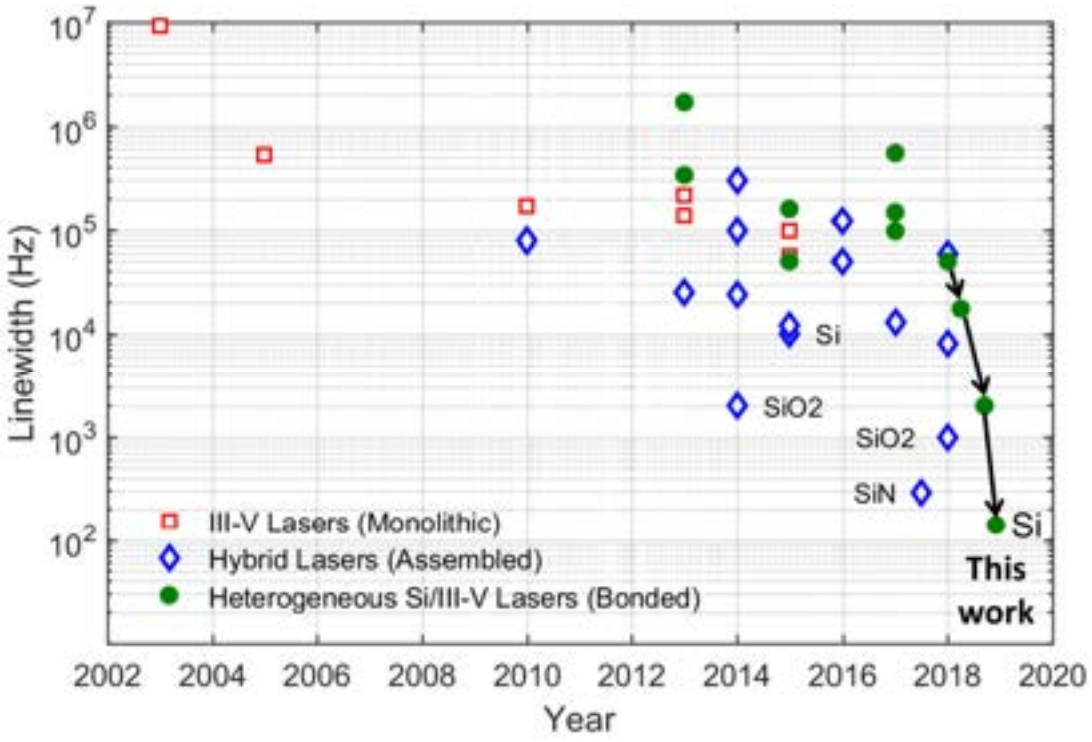

Figure 8.1. Widely-tunable integrated lasers linewidth progress in time. The arrows show the progress of results accomplished in the scope of this dissertation.

8.2 Future directions

The ultralow noise lasers in this thesis have a relatively high complexity in the architecture, containing many elements from actives to passives and tapers. That means every improvement in those individual components would help to enhance the laser performances. In particular, the most important improvements that could be the focuses for a continuation of this work include:

- Optical amplifier (for the gain section of the lasers): The gain epi design used in this thesis was a result of multiple iterations of epi optimization cycles done by Bowers group at UCSB [11]. However, there is plenty of room for epi design optimization. For example, increase the strain in quantum well would potentially help reduce the internal loss, which would benefit the linewidth. Furthermore, using a properly

designed GRINSCHs [12] instead of abrupt SCHs as in the current lasers would increase the current injection efficiency for higher laser output power. For broad gain spectrum which is beneficial for the ultrawide tunable lasers, variable-composition multi-quantum wells with different bandgaps can be used to obtain ultrabroad spectra [13], [14].

- Silicon waveguide loss: Since the propagation loss in the ultralow silicon waveguides is still dominantly limited by scattering loss, improvement in waveguide line edge and sidewall roughness would significantly bring the loss down. Some highly effective methods have been known from literature such as photoresist reflow [15], [16] and oxidation smoothening [17], [18]. These techniques can certainly be applied in future work to gain a several times reduction in the scattering loss, which could lead to order of magnitude improvement in the associated laser linewidth. Much care must be taken in calibration and mask bias, however, in order to reproducibly obtain the desired dimensions of fine structures going through those processes.
- Other cavity designs: One attractive point about the integrated extended cavity laser is the flexibility available for the cavity designs. For narrow linewidth lasers, the extended cavity could be anything but capable of achieving a high Q resonance to have very sharp filtering effect. In the limited scope of this thesis, we were only able to explore two types of extended cavity architectures for low noise lasers: ring resonator-based and long grating- based designs. Plenty of other high Q structures could be promising and interesting for future work exploration, such as slow-light photonic crystal [19] and high Q grating-defect resonators in DBR lasers.

References

[1] C. Zhang, P. A. Morton, J. B. Khurgin, J. D. Peters, and J. E. Bowers, "Ultralinear heterogeneously integrated ring-assisted Mach–Zehnder interferometer modulator on silicon," *Optica*, vol. 3, no. 12, p. 1483, 2016.

[2] P. A. Morton *et al.*, "High-Power, High-Linearity, Heterogeneously Integrated III-V on Si MZI Modulators for RF Photonics Systems," *IEEE Photonics J.*, vol. submitted, 2019.

[3] J. Hulme *et al.*, "Fully integrated microwave frequency synthesizer on heterogeneous silicon-III/V," *Opt. Express*, vol. 25, no. 3, p. 2422, 2017.

[4] T. Komljenovic, D. Huang, P. Pintus, M. A. Tran, M. L. Davenport, and J. E. Bowers, "Photonic Integrated Circuits Using Heterogeneous Integration on Silicon," *Proceedings of the IEEE*. 2018.

[5] M. Tran, D. Huang, T. Komljenovic, J. Peters, A. Malik, and J. Bowers, "Ultra-Low-Loss Silicon Waveguides for Heterogeneously Integrated Silicon/III-V Photonics," *Appl. Sci.*, vol. 8, no. 7, p. 1139, 2018.

[6] P. P. Absil *et al.*, "Imec iSiPP25G silicon photonics: a robust CMOS-based photonics technology platform," in *Proceedings of SPIE OPTO*, 2015.

[7] A. Biberman, M. J. Shaw, E. Timurdogan, J. B. Wright, and M. R. Watts, "Ultralow-loss silicon ring resonators," vol. 37, no. 20, pp. 4236–4238, 2012.

[8] D. Dai, J. Bauters, and J. E. Bowers, "Passive technologies for future large-scale photonic integrated circuits on silicon: Polarization handling, light non-reciprocity and loss reduction," *Light Sci. Appl.*, vol. 1, no. MARCH, pp. 1–12, 2012.

[9] C. G. H. Roeloffzen *et al.*, "Low-loss si3n4 triplex optical waveguides: Technology

and applications overview," *IEEE Journal of Selected Topics in Quantum Electronics*, vol. 24, no. 4. 2018.

[10] D. D'Agostino *et al.*, "Low-loss passive waveguides in a generic InP foundry process via local diffusion of zinc," *Opt. Express*, vol. 23, no. 19, p. 25143, 2015.

[11] M. L. Davenport, "Heterogeneous Silicon III-V Mode-Locked Lasers," UCSB, 2017.

[12] H. Hirayama, Y. Miyake, and M. Asada, "Analysis of current injection efficiency of separate-confinement-heterostructure quantum-film lasers," *IEEE J. Quantum Electron.*, vol. 28, no. 1, pp. 68–74, 1992.

[13] I. J. Fritz, J. F. Klem, M. J. Hafich, A. J. Howard, and H. P. Hjalmarson, "Broad-band light-emitting diode for 1.4-2.0 μm using variable-composition InGaAs quantum wells," *IEEE Photonics Technol. Lett.*, vol. 7, no. 11, pp. 1270–1272, Nov. 1995.

[14] Xiang Zhu *et al.*, "1.4-μm InGaAsP-InP strained multiple-quantum-well laser for broad-wavelength tunability," *IEEE Photonics Technol. Lett.*, vol. 9, no. 9, pp. 1202–1204, Sep. 1997.

[15] J. CAI, P. H. LIM, Y. ISHIKAWA, and K. WADA, "Silicon Waveguide Sidewall Smoothing By Resist Reflowing," *J. Nonlinear Opt. Phys. Mater.*, vol. 19, no. 04, pp. 801–809, 2010.

[16] G. A. Porkolab, P. Apiratikul, B. Wang, S. H. Guo, and C. J. K. Richardson, "Low propagation loss AlGaAs waveguides fabricated with plasma-assisted photoresist reflow," *Opt. Express*, vol. 22, no. 7, p. 7733, 2014.

[17] K. K. Lee, D. R. Lim, L. C. Kimerling, J. Shin, and F. Cerrina, "Fabrication of ultralow-loss Si/SiO(2) waveguides by roughness reduction.," *Opt. Lett.*, vol. 26, no. 23, pp. 1888–1890, 2001.

[18] D. K. Sparacin, S. J. Spector, and L. C. Kimerling, “Silicon waveguide sidewall smoothing by wet chemical oxidation,” *J. Light. Technol.*, vol. 23, no. 8, pp. 2455–2461, 2005.

[19] T. Baba, “Slow light in photonic crystals,” *Nat. Photonics*, vol. 2, no. 8, pp. 465–473, Aug. 2008.

Appendix 1. Multiring Mirrors – Theory

Multiring mirrors, the term used through this thesis, refers to a class of integrated waveguide mirror structures depicted in *Figure A1.1*. A multiring mirror is constructed by cascading multiple add-drop ring resonator filters within a loop mirror. The loop mirror is formed with either a 1x2 (as depicted in *Figure A1.1*) or 2x2 waveguide coupler. In this section, we will establish all the formulation of the mirror transfer functions needed for understanding the resonance spectral properties of the structures. We will use Mason's rule to derive the analytical equations for the basic add-drop filter responses and apply the same method to obtain the results for all multiring mirror structures above.

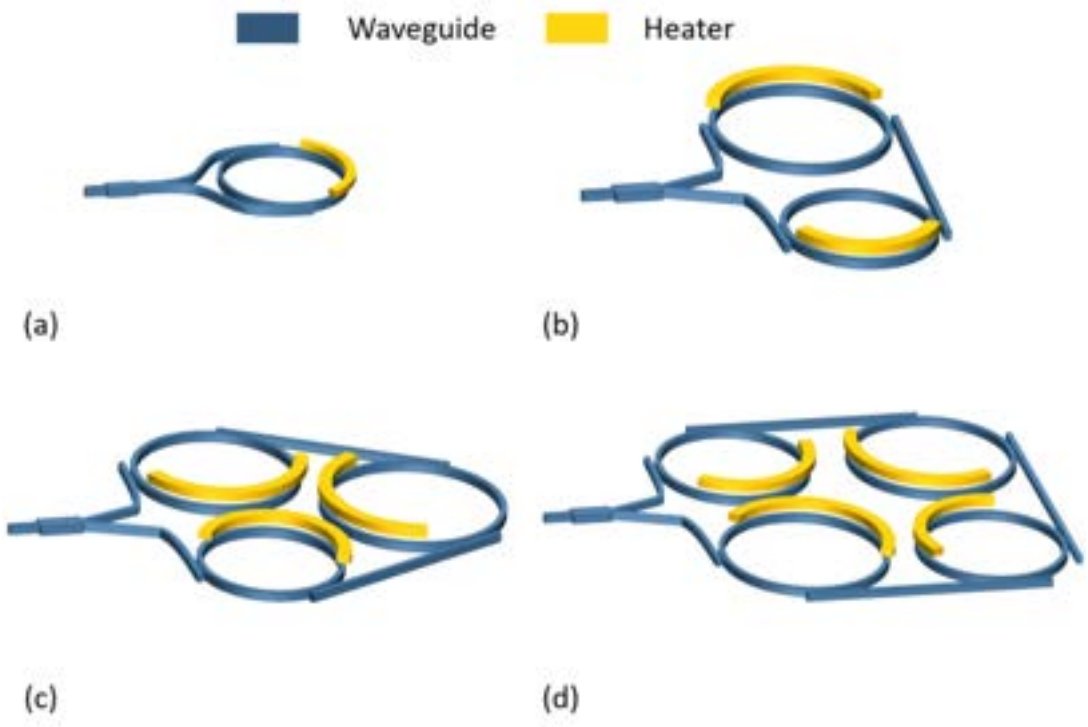

Figure A1.1 Schematic configurations of multiring mirrors (a) Single-ring (1R) mirror (b) Dual-ring (2R) mirror (c) Triple-ring (3R) mirror (d) Quad-ring (4R) mirrors. The heaters above the waveguides are used to change the local temperature of the rings, allowing resonance tuning due to thermo-optic effect.

1.1 Ring resonator structure analysis using Mason's rule

Mason's rule [1] is a technique coming from control systems engineering. It can be effective in directly obtaining the expression for relating the output of a system to its input. Mason's rule states that the overall transmittance (transfer function) of a signal flow graph is given by

$$T = \frac{\sum_k T_k \Delta_k}{\Delta} \qquad (1.19)$$

where k is the number of forward paths for the signal, T_k is the k^{th} forward path gain, and Δ is the determinant of the graph given by

$$\Delta = 1 - \sum L_i + \sum L_i L_j - \sum L_i L_j L_k + \ldots + (-1)^m \sum \ldots + \ldots \qquad (1.20)$$

where L_i is loop gain of each closed loop in the system, $L_i L_j$ is the product of the loop gains of any two non-touching loops, $L_i L_j L_k$ is the product of the loop gains of any three non-touching loops. Finally, Δ_k is the cofactor value of Δ for the k^{th} forward path, with all the loops touching the k^{th} forward path removed.

We will derive the transfer functions for an add-drop ring resonator filter, the essential building block for the multiring mirror structures considered here, to show the effectiveness of Mason's rule in ring resonator structure analysis. A schematic add-drop ring resonator filter and its equivalent signal flow graph are shown in *Figure 2.1*. For simplicity, we assume lossless coupling for the ring-bus couplers. The scattering matrix for a lossless ring-bus coupler, like that of a lossless directional waveguide coupler, is given by

$$\begin{bmatrix} t & -j\kappa \\ -j\kappa & t \end{bmatrix} \qquad (1.21)$$

where κ is the amplitude cross-coupling coefficient and $t = \sqrt{1-\kappa^2}$ is the amplitude self-coupling coefficient (note that $\kappa, t \in \mathbb{R}$ and $0 \le \kappa, t \le 1$). The term $z^{1/2}$ shown on the signal flow graph represents the ring half-roundtrip transmittance, *i.e.*

$$z = Ae^{j\theta} \qquad (1.22)$$

where $A = 2\pi R\sqrt{10^{-\alpha/10}}$ *(1.23)* is the ring round-trip amplitude loss and $\theta = 4\pi^2 n_{eff}\frac{R}{\lambda}$ *(1.24)* is the round trip accumulated phase. Here, R is the radius of the ring, n_{eff} is the effective index of the mode of consideration, α (normally in the unit of dB/cm) is the commonly used waveguide power propagation loss rate and λ is the wavelength.

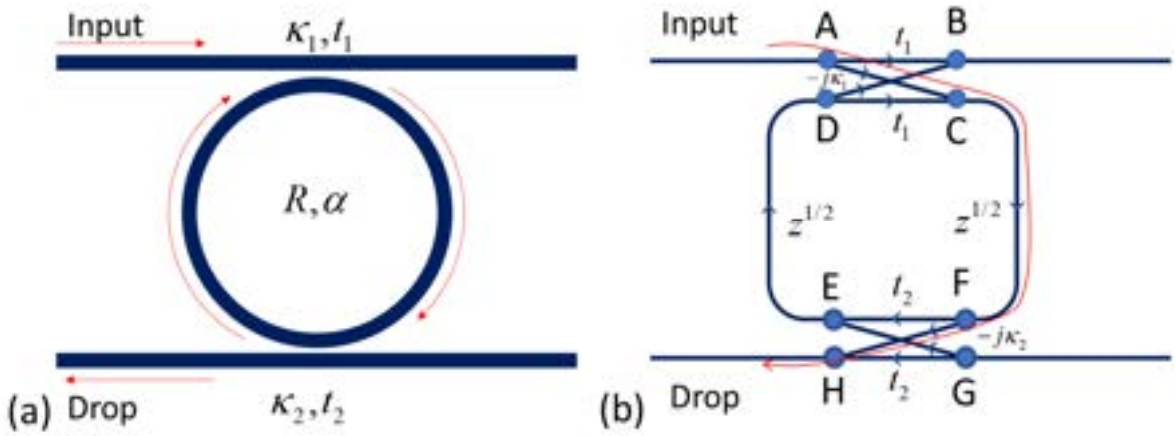

Figure A1.2 (a) Schematic of an add-drop ring resonator filter with two bus waveguides coupled to a ring resonator (b) Signal-flow graph of the same add-drop ring resonator filter.

In this simple case, for the drop signal, there is only one forward path (ACFH) indicated by the red arrowed curve in *Figure 2.1(b).* The transmittance of this path is $T_1 = (-j\kappa_1)z^{1/2}(-j\kappa_2) = -\kappa_1\kappa_2 z^{1/2}$. We also have only one closed-loop (CFDEC), and the gain of this closed-loop is $L_1 = t_2 z^{1/2} t_1 z^{1/2} = t_1 t_2 z$, therefore the determinant of the path $\Delta = 1 - L_1 = 1 - t_1 t_2 z$ and $\Delta_1 = 1$.

Hence, the transmittance to the drop port of the add-drop filter is given by

$$Drop(\kappa_1,\kappa_2,z)=\frac{-\kappa_1\kappa_2 z^{1/2}}{1-t_1t_2z} \quad (1.25)$$

Replacing z by the expression *(1.22)*, we achieve the full form

$$Drop(\kappa_1,\kappa_2,R,\alpha)=\frac{-\kappa_1\kappa_2 A^{1/2}e^{j\theta/2}}{1-t_1t_2Ae^{j\theta}}=\frac{-\kappa_1\kappa_2\left(2\pi R\sqrt{10^{-\alpha/10}}\right)^{1/2}e^{j4\pi^2 n_{eff}\frac{R}{\lambda}/2}}{1-\sqrt{\left(1-\kappa_1^2\right)\left(1-\kappa_2^2\right)}2\pi R\sqrt{10^{-\alpha/10}}e^{j4\pi^2 n_{eff}\frac{R}{\lambda}}} \quad (1.26)$$

Similarly, the transfer function of the through port of the filter can also be computed as follows. For the through port output, the signal flow graph is drawn in *Figure A1.3(b).* In this case, we have two forward paths indicated by the red arrowed curves.

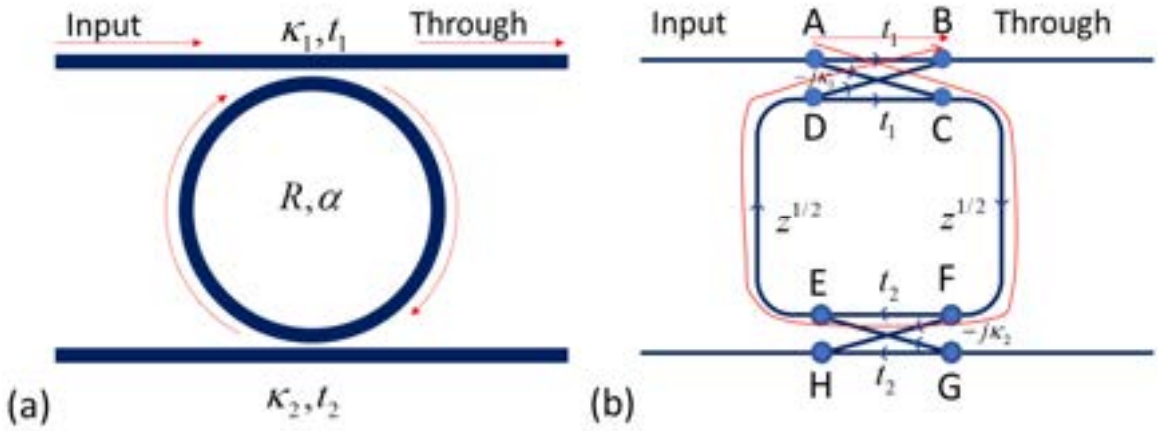

Figure A1.3 (a) Add-drop filter with output at the through port (b) Signal-flow graph shows the two forward paths from the input to the output at the through port.

The first path is (AB) with simply $T_1 = t_1$; the second path is (ACFEDB) with

$T_2 = (-j\kappa_1)z^{1/2}t_2z^{1/2}(-j\kappa_1) = -\kappa_1^2 t_2 z$.

We have only one closed-loop (CFEDC) with the loop gain $L_1 = t_1 z^{1/2} t_2 z^{1/2} = t_1 t_2 z$.

Therefore, therefore the determinant of the graph is $\Delta = 1 - L_1 = 1 - t_1 t_2 z$. Note that now we have $\Delta_1 = 1 - L_1 = 1 - t_1 t_2 z$ because the closed-loop (CFEDC) does not touch the 1st path, and $\Delta_2 = 1$ because the closed-loop touches the 2nd path.

Therefore, the transfer function for the through port is computed as

$$Through\left(\kappa_1, \kappa_2, z\right) = \frac{t_1\left(1 - t_1 t_2 z\right) - \kappa_1^2 t_2 z}{1 - t_1 t_2 z} = \frac{t_1 - t_1^2 t_2 z - \kappa_1^2 t_2 z}{1 - t_1 t_2 z} = \frac{t_1 - t_2 z}{1 - t_1 t_2 z} \qquad (1.27)$$

The last equality in the equation *(1.27)* is achieved because of the lossless assumption on the bus-ring coupler which leads to $\kappa_1^2 + t_1^2 = 1$. The full form of *(1.27)* can also be written as

$$Through\left(\kappa_1, \kappa_2, R, \alpha\right) = \frac{t_1 - t_2 A e^{j\theta}}{1 - t_1 t_2 A e^{j\theta}} = \frac{\sqrt{\left(1 - \kappa_1^2\right)} - \sqrt{\left(1 - \kappa_2^2\right)} 2\pi R \sqrt{10^{-\alpha/10}} e^{j 4\pi^2 n_{eff} \frac{R}{\lambda}}}{1 - \sqrt{\left(1 - \kappa_1^2\right)\left(1 - \kappa_2^2\right)} 2\pi R \sqrt{10^{-\alpha/10}} e^{j 4\pi^2 n_{eff} \frac{R}{\lambda}}} \qquad (1.28)$$

1.2 Single-ring mirror frequency response analysis

Using Mason's rule, we will derive the transfer functions for the single-ring mirror structure shown in *Figure A1.4(a)*. The single-ring mirror structure has reflection output on the same port of the waveguide coupler (denoted by cross-coupling coefficient κ_c) with the input signal but opposite moving direction. In the case of a 2x2 coupler being used, it also has a transmission output, which is the signal that comes out through the port of the coupler.

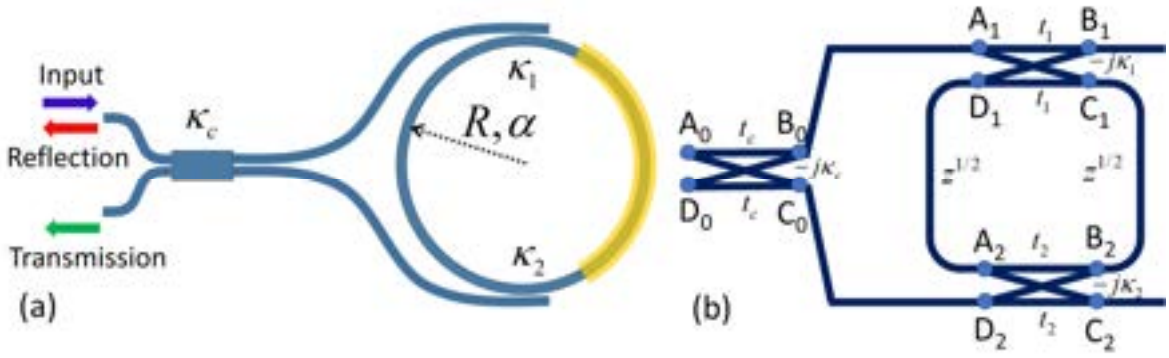

Figure A1.4 (a) Single-ring mirror schematic. The mirror is comprised of a 2x2 (or 1x2) couplers and two bus waveguides coupling to a ring resonator to form a loop. (b) The equivalent signal flow graph.

An equivalent signal flow graph with the same denotations as in a previous section is depicted in *Figure A1.4(b)*. For the reflection signal, we have two following forward paths:

The first path (clockwise) is ($A_0B_0A_1C_1B_2D_2C_0A_0$), with

$$T_1 = t_c(-j\kappa_1)z^{1/2}(-j\kappa_2)(-j\kappa_c) = jt_c\kappa_c\kappa_1\kappa_2 z^{1/2}$$

The second path (counter-clockwise) is ($A_0B_0A_1C_1B_2D_2C_0A_0$), with

$$T_2 = (-j\kappa_c)(-j\kappa_2)z^{1/2}(-j\kappa_1)t_c = jt_c\kappa_c\kappa_1\kappa_2 z^{1/2} = T_1$$

Accordingly, there are two closed-loops in total to count, although they are only different in the signal flowing directions:

The first loop (clockwise) is ($C_1B_2A_2D_2C_1$), with the loop gain $L_1 = z^{1/2}t_2z^{1/2}t_1 = t_1t_2z$.

The second one (counter-clockwise) is ($B_2C_1D_1A_2B_2$), with the loop gain $L_2 = z^{1/2}t_1z^{1/2}t_2 = t_1t_2z = L_1$.

These two closed-loops are non-touching because the waves move in opposite directions. The determinant of the graph is, therefore, given by

$$\Delta = 1-(L_1+L_2)+L_1L_2 = (1-L_1)(1-L_2)$$

Since the second loop does not touch the first path and the first loop does not touch the second path, we have $\Delta_1 = 1 - L_2$ and $\Delta_2 = 1 - L_1$. With that, we have

$$Reflection(\kappa_c, \kappa_1, \kappa_2, z) = \frac{T_1(1-L_2) + T_2(1-L_1)}{(1-L_1)(1-L_2)} = \frac{T_1}{1-L_1} + \frac{T_2}{1-L_2} = 2\frac{T_1}{1-L_1} = \frac{2jt_c\kappa_c\kappa_1\kappa_2 z}{1-t_1t_2z}$$

It can be rewritten as

$$Reflection(\kappa_c, \kappa_1, \kappa_2, z) = -2jt_c\kappa_c \frac{-\kappa_1\kappa_2 z}{1-t_1t_2z} = -2j\sqrt{(1-\kappa_c^2)\kappa_c^2} \cdot Drop(\kappa_1, \kappa_2, z) \qquad (1.29)$$

Therefore

$$Reflection(\kappa_c, \kappa_1, \kappa_2, R, \alpha) = -2j\sqrt{(1-\kappa_c^2)\kappa_c^2} \cdot Drop(\kappa_1, \kappa_2, R, \alpha) \quad (1.30)$$

Similarly, we can obtain the results for the transmission output signal (in the case of 2x2 coupler used for the loop mirror):

$$Transmission(\kappa_c, \kappa_1, \kappa_2, R, \alpha) = (1-2\kappa_c^2) \cdot Drop(\kappa_1, \kappa_2, R, \alpha) \qquad (1.31)$$

We notice that the first part of *1.30* is nothing but the transfer function of the reflection signal from a loop mirror based on a coupler with amplitude cross-coupling coefficient κ_c. Hence, we have

$$Reflection(\kappa_c, \kappa_1, \kappa_2, R, \alpha) = LoopMirror(\kappa_c) \cdot Drop(\kappa_1, \kappa_2, R, \alpha) \quad (1.32)$$

We can also analyze the structure using different method, as the following.

Let a_0 be the input wave to the input of the single-mirror structure shown in *Figure A1.4*. We first derive equations for the reflection waves b'_0 and b_0. Then we have the following relations:

$$
\begin{aligned}
a_1 &= \sqrt{1-\kappa_c^2}\, a_0 \\
a'_1 &= j\kappa_c a_0 \\
b_1 &= a_1 \cdot Drop\left(\kappa_1, \kappa_2, R, \alpha\right) \\
b'_1 &= a'_1 \cdot Drop\left(\kappa_2, \kappa_1, R, \alpha\right) \\
b_0 &= \sqrt{1-\kappa_c^2}\, b_1 + j\kappa_c b'_1 \\
b'_0 &= j\kappa_c b_1 + \sqrt{1-\kappa_c^2}\, b'_1
\end{aligned}
\qquad (1.33)
$$

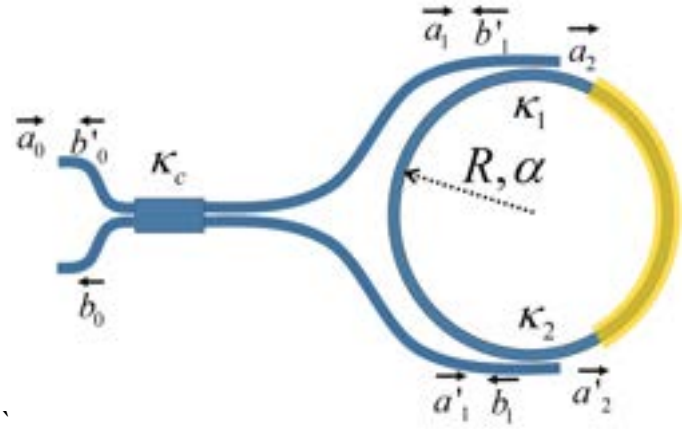

Figure A1.5 Single-ring mirror schematic with the annotation for the analysis

Relating the final equation to the previous ones, we can rewrite the equations of the reflection waves:

$$
\begin{aligned}
b_0 &= \sqrt{1-\kappa_c^2}\, b_1 + j\kappa_c b'_1 = a_0\left(1-\kappa_c^2\right)\cdot Drop\left(\kappa_1, \kappa_2, R, \alpha\right) - a_0\kappa_c^2 \cdot Drop\left(\kappa_2, \kappa_1, R, \alpha\right) \\
b'_0 &= j\kappa_c b_1 + \sqrt{1-\kappa_c^2}\, b'_1 = ja_0\sqrt{\left(1-\kappa_c^2\right)\kappa_c^2}\cdot Drop\left(\kappa_1, \kappa_2, R, \alpha\right) + ja_0\sqrt{\left(1-\kappa_c^2\right)\kappa_c^2}\cdot Drop\left(\kappa_2, \kappa_1, R, \alpha\right)
\end{aligned}
$$

(1.34)

Since we have $Drop\left(\kappa_1, \kappa_2, R, \alpha\right) = Drop\left(\kappa_2, \kappa_1, R, \alpha\right)$ from the previous section, the final forms of the reflection and transmission waves can be obtained, which are identical to the results computed previously with Mason's rule:

$$
\begin{aligned}
b_0 &= \sqrt{1-\kappa_c^2}\, b_1 + j\kappa_c b'_1 = a_0\left(1-2\kappa_c^2\right)\cdot Drop\left(\kappa_1, \kappa_2, R, \alpha\right) \\
b'_0 &= j\kappa_c b_1 + \sqrt{1-\kappa_c^2}\, b'_1 = ja_0 2\sqrt{\left(1-\kappa_c^2\right)\kappa_c^2}\cdot Drop\left(\kappa_1, \kappa_2, R, \alpha\right)
\end{aligned}
\qquad (1.35)
$$

The free spectral range (FSR) of the single-ring mirror is the same as that of the ring resonator itself, which is given by:

$$FSR^{Hz} = \frac{c}{n_g 2\pi R}$$
$$FSR^{meter} = \frac{\lambda^2}{n_g 2\pi R} \qquad (1.36)$$

where $n_g = n_{eff} - \lambda \frac{\partial n_{eff}(\lambda)}{\partial \lambda}$ is the group index of the mode and $2\pi R$ is the round-trip length of the resonator; however, we ignore the dispersion in our analysis for the simplicity of the model.

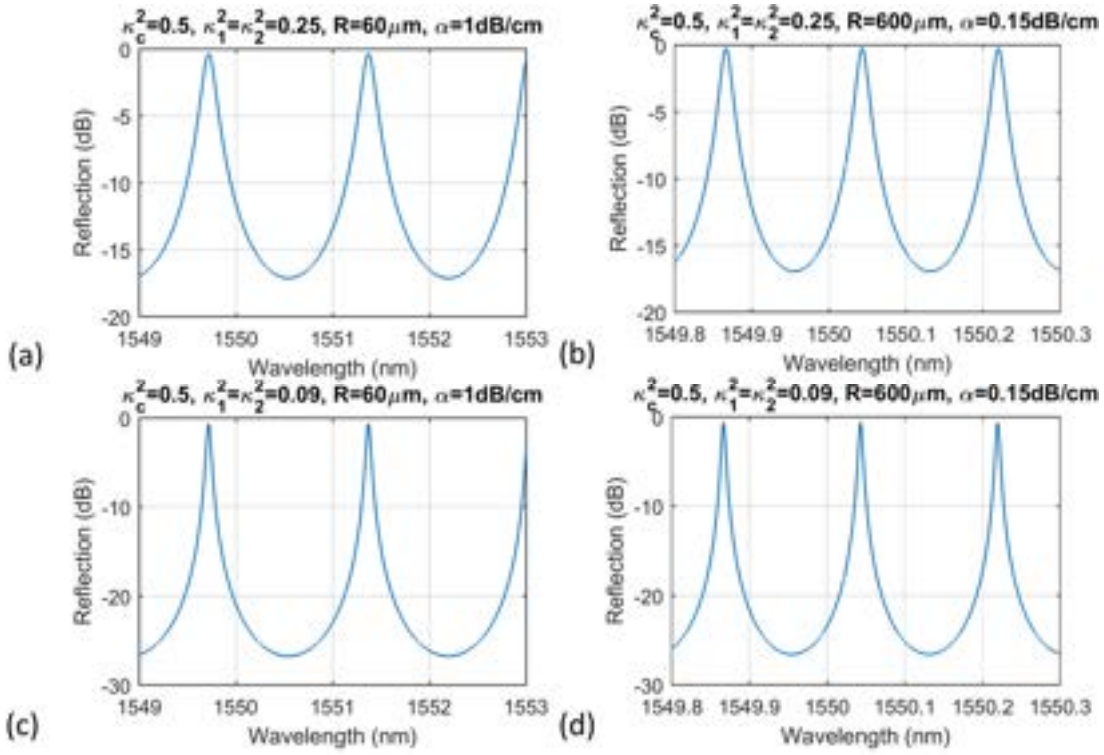

Figure A1.6 Reflection spectra of single-ring mirror structures with different sets of parameters

The wavelength response of single-ring mirrors with various sets of ring radii and coupling ratios are computed and plotted in *Figure A1.6*. The ring radii and the waveguide loss rate used to plot in *Figure A1.6*. (a) and (c) are that of typical 231 nm etched, 650 nm wide rib waveguides, and (b) and (d) are for the ultralow loss 56 nm shallowly etched, 1.8 μm wide waveguides.

As can be seen clearly, the sharpness of the resonances - which can be indicated by the quality factor *(Q)* - is a strong function of *the coupling ratios, waveguide loss* and *the ring radius* as governed by equation *1.37*:

$$\frac{1}{Q_{\text{loaded}}} = \frac{1}{Q_{\text{int}}} + \frac{1}{Q_{\text{ext}}} = \frac{\alpha_{wg}}{\omega} + \left(\frac{\kappa_1}{\omega 2\pi R} + \frac{\kappa_2}{\omega 2\pi R} \right) \qquad (1.37)$$

In practice, the two bus-ring couplers are preferably made identical to reduce the number of variables the designers have to handle.

1.3 Dual-ring mirror frequency response analysis

The dual-ring mirror is constructed by adding to the single-ring mirror one more add-drop ring resonator cascaded with the first ring. Using a similar path to derive equations for the mirrors, we can easily obtain the transfer function for the reflection wave as

$$Reflection\left(\kappa_c, \left\{\kappa_{n1}, \kappa_{n2}, R_n, \alpha_n\right\}_{n=\overline{1,2}}\right) = LoopMirror\left(\kappa_c\right) \cdot Drop\left(\kappa_{11}, \kappa_{12}, R_1, \alpha_1\right) \cdot Drop\left(\kappa_{21}, \kappa_{22}, R_2, \alpha_2\right)$$

(1.38)

Equation *1.38* reflects serial coupling between the components in the structure. It can be utilized to enable the expansion of the free spectral range of the composite spectrum of the mirror based on the Vernier principle.

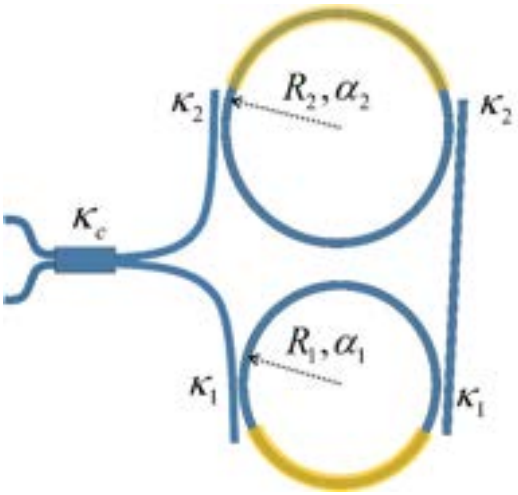

Figure A1.7 Dual-ring mirror schematic. The mirror is comprised of a 2x2 (or 1x2) couplers and two cascaded add-drop filters.

As shown in *Figure A1.8* (a, c, e), the spectra of the mirror reflection response have different FSR values depending on the relation between the radii of the two ring resonators. In *Figure A1.8*(a), R_1=60 μm and R_2=65 μm result in an extended FSR of ~20 nm; when R_2 is decreased to 62.5 μm as in *Figure A1.8*(c) and (e), the mirror's FSR then increases to ~40 nm.

For use of these mirror structures as filter for a single mode laser, the side mode suppression ratio (SMSR) within the optical gain bandwidth is an important figure of merit. Typical semiconductor lasers might have 40-60 nm bandwidth, rendering the usefulness of the structure in (a) because two resonance peaks can coexist within the gain spectrum. Extending the FSR to 40 nm makes structures in (c) and (e) applicable. However, the SMSR of the mirror when we extended the FSR from the structure (a) to (c), as shown in the close-up around the resonance in (d), became relatively low (~1 dB) for a stable lasing mode selection requirement. To increase the SMSR, one simple way is make the resonance peaks sharper, by lowering the bus-ring coupling ratios κ_1 and κ_2 (equivalently, increasing the loaded Q, for example from 0.25 to 0.12), as shown in figure (e) and (f). It is because the resonance peaks

of the two ring resonators separates more rapidly from each other when the width of each resonance gets smaller for lower κ.

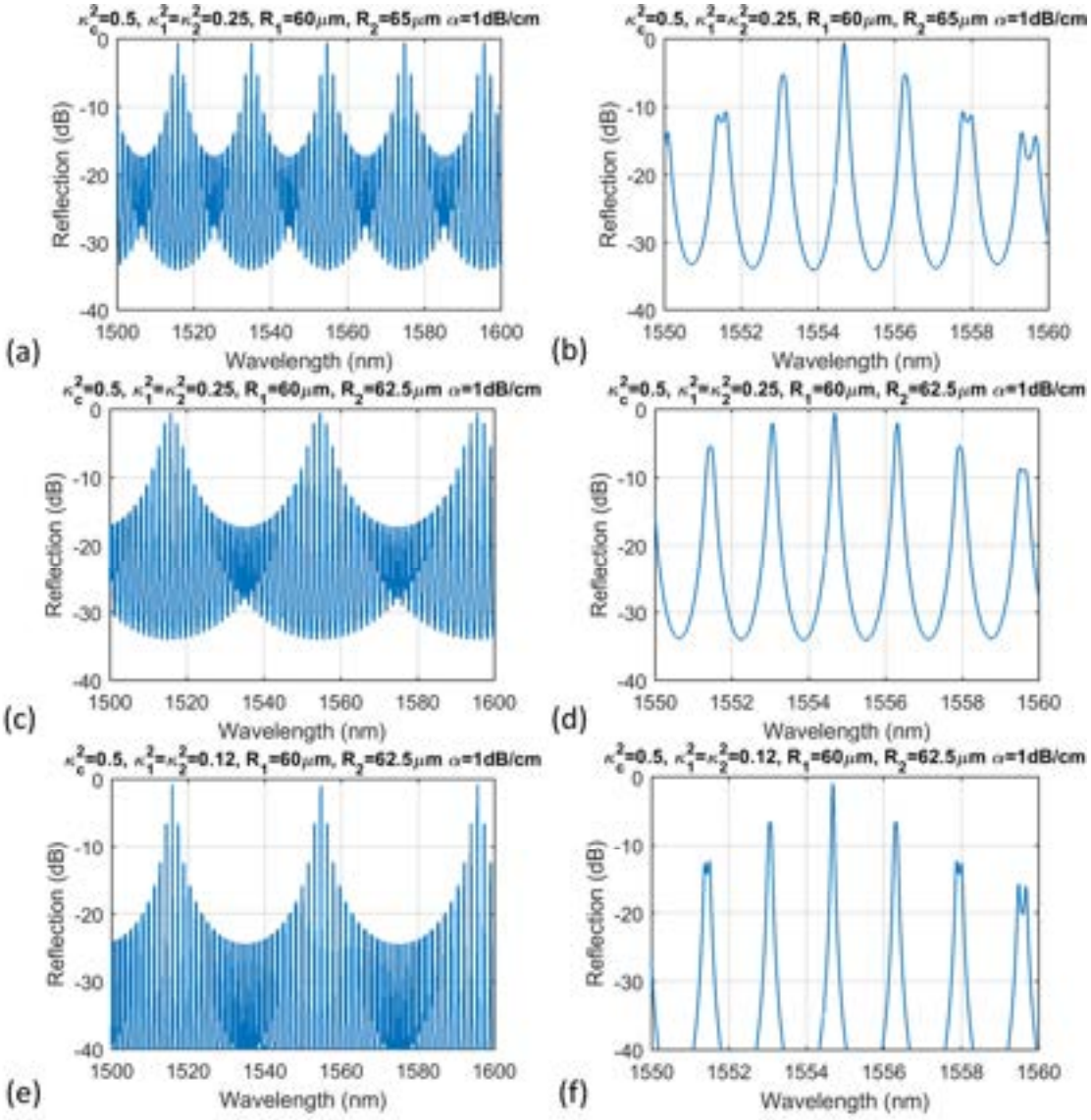

Figure A1.8 Reflection spectra of dual-ring mirror structures with various values of bend radii and coupling ratios. Plot (b), (d) and (f) are the close-up of (a), (c) and (e), respectively. These bend radii and waveguide loss are representative for the standard Silicon 231 nm etched waveguides.

Side mode suppression becomes a serious detriment when the bend radius of the ring increases. At the minimum bend radius (~600 μm) of single mode ultralow loss Si waveguide,

the FSR of individual rings becomes tiny and results in very dense comb lines in the dual ring mirror spectrum as shown in Figure A1.9. When the coupling ratio is 0.12, the SMSR is not visible (Figure A1.9 (a) and (b)). Even when the coupling is lowered 3 times to 0.04, the SMSR improves but still lower than 1 dB, as shown in Figure A1.9 (c) and (d). It is clear that more filtering is necessary to obtain sufficient selectivity of one mode with in the laser. This can be achieved with the addition of the third ring or more into the mirror structures.

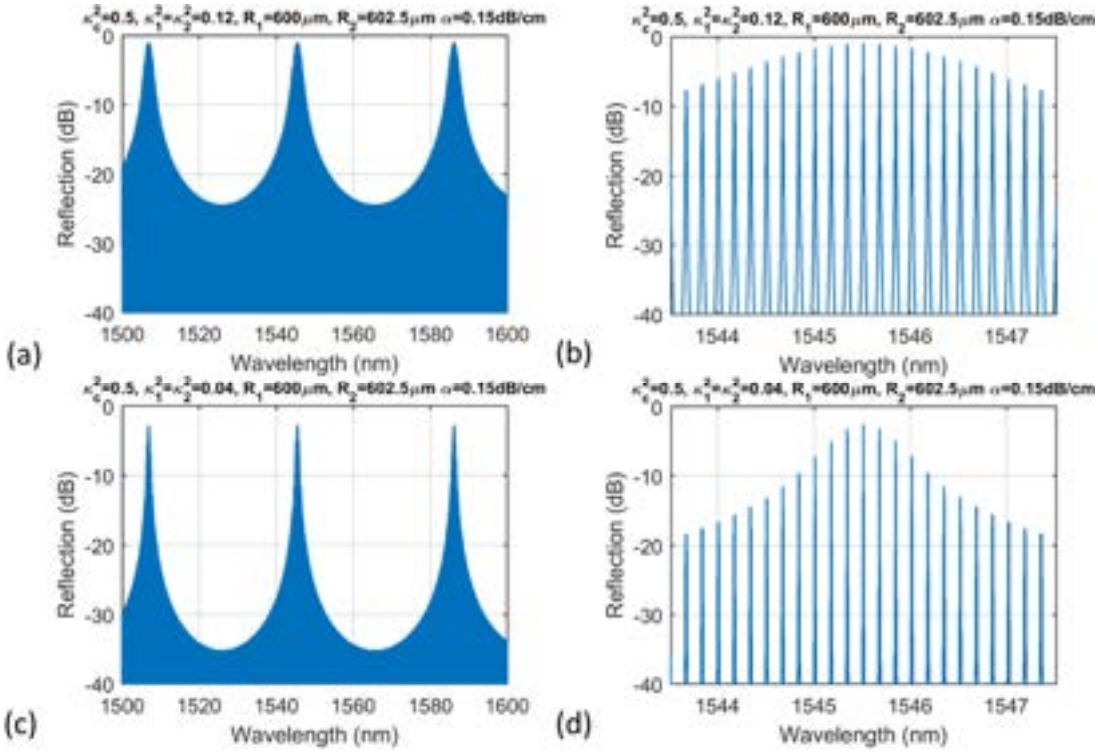

Figure A1.9 Reflection spectra of dual-ring mirror structures with large bend radii (~600 μm) shows low side mode suppression ratio. Plot (b) and (d) are the close-up of (a) and (c) respectively.

1.4 Multiring mirror frequency response analysis

The transfer function for the reflection wave can be generalized for the case of multiring mirrors:

$$Reflection\left(\kappa_c,\{\kappa_{n1},\kappa_{n2},R_n,\alpha_n\}_{n=\overline{1,\#ring}}\right)=LoopMirror\left(\kappa_c\right)\cdot\prod_{n=1}^{\#ring}Drop\left(\kappa_{n1},\kappa_{n2},R_n,\alpha_n\right)$$

(1.39)

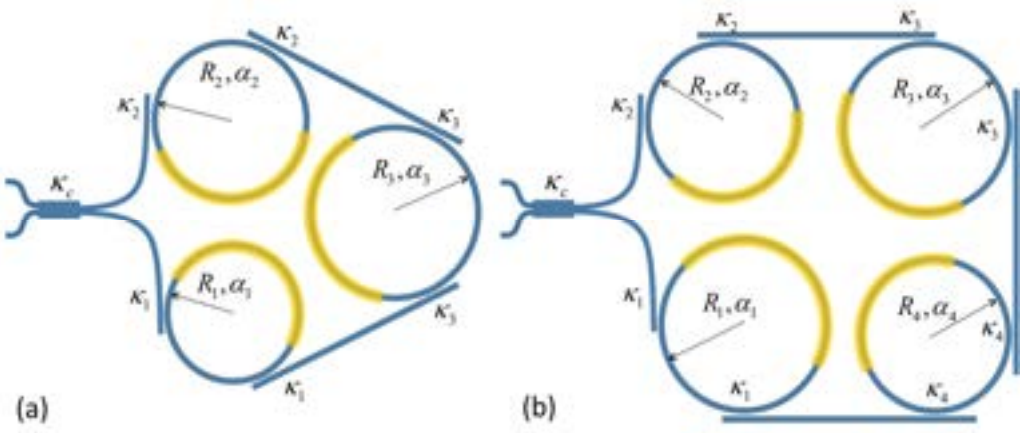

Figure A1.10 Triple-ring (3R) and Quad-ring (4R) mirror schematics.

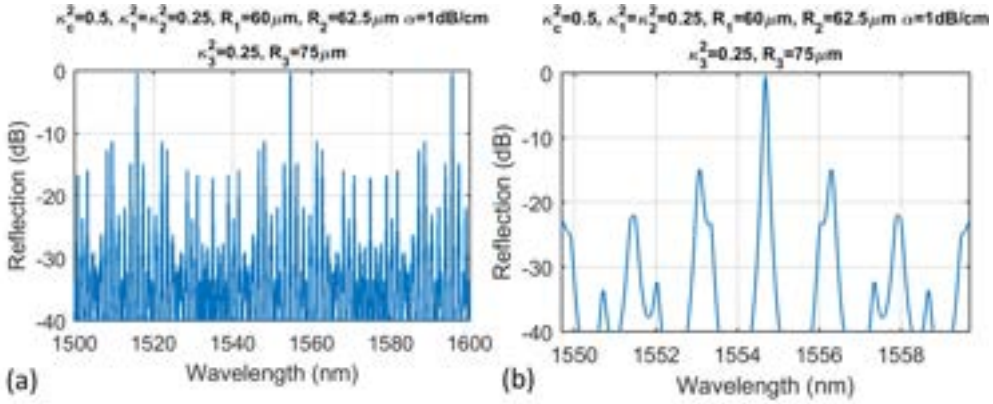

Figure A1.11 Reflection spectra of triple-ring mirror structure (a, b) with ~60 μm bend radii shows significantly improved SMSR compared to that of the dual-ring mirror shown in Figure A1.8 (c) and (d).

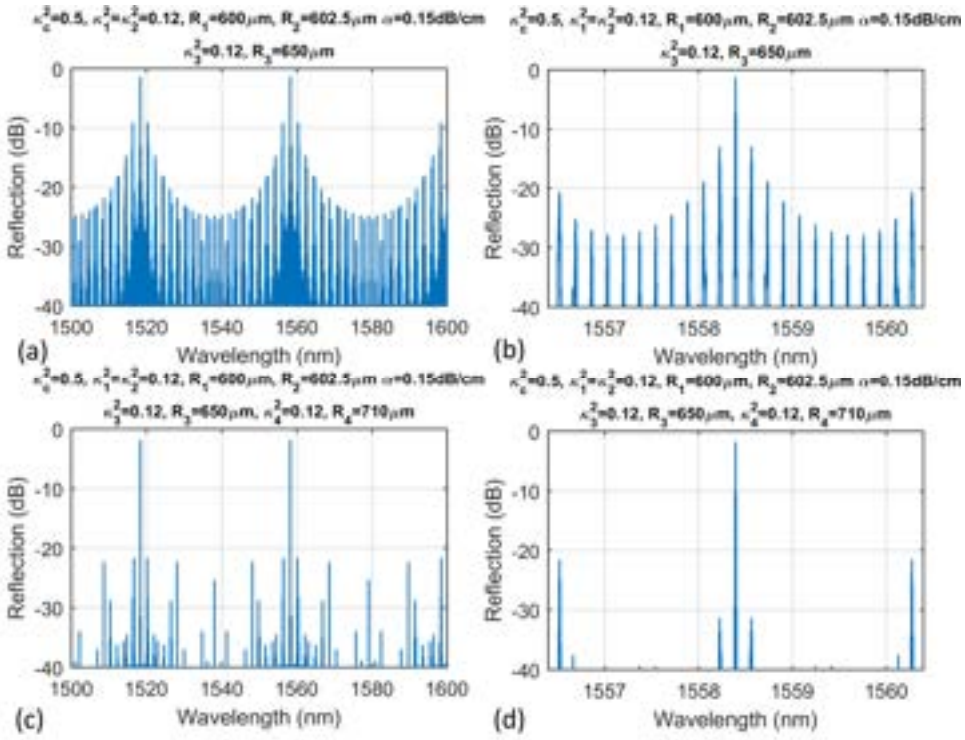

Figure A1.12 Reflection spectra of triple-ring mirror structure (a, b) with large bend radii (~600 μm) shows significantly improved SMSR compared to that of the dual-ring mirror shown in Figure A1.9. Quad-ring mirror structure (c, d) further improves the performance. Plots (b) and (d) are the close-up of (a) and (c), respectively.

1.5 Summary

In this appendix, we have carried out rigorous derivations for the multiring mirror structures, using Mason rules and the transfer matrix method. This is necessary to accurately model and analyze the multiring mirror structures for laser simulation, which has been essential for us in achieving an ultrawide tuning range and ultralow noise performance with triple-ring and quad-mirrors in this thesis.

References

1. Nise, N. S. Control systems engineering; ISBN 9781118170519

Appendix 2. Waveguide and Couplers Characterization

Waveguides and couplers are among the most essential building blocks for any photonic integrated circuits (PIC). In the literature, various methods for measuring waveguide propagation loss have been reported. However, most of them require either multiple structures with different lengths (variation of the cut-back method) [1] or a known reflectivity (Fabry-Perot based methods) [2, 3]. A disadvantage of cut-back based methods lies in their sensitivity to coupling efficiency variation among multiple devices, resulting in a relatively large uncertainty or a need to test a larger number of devices. Fabry-Perot loss modulation methods are, as was already pointed out, sensitive to facet reflectivity. The measurement of the coupling ratios of waveguide couplers in general also suffers from the input coupling loss issue, where the unequal losses of the coupling between fibers to waveguides directly leads to inaccuracy of the results.

The aforementioned issues may be eliminated by analyzing optical spectral transmission of micro-ring or Mach-Zehnder Interferometer (MZI) structure [4]–[8]. For ring-based structures, curve fitting generally must be used. This requires several device splits to discern the coupling and the waveguide loss or to obtain the coupling regimes of interest [5, 6]. With MZI based structures, methods using an unbalanced MZI (UMZI) formed by a directional coupler and a multi-mode interference coupler [7] or two Y-branches [8] have been proposed. However, existing analysis techniques for these structures can only extract the coupling coefficient of the coupler [7] or still require multiple test structures to extract the waveguide loss [8].

In the scope of this dissertation, we have implemented a new method for simultaneously extracting both the waveguide propagation loss and the power coupling ratios of the couplers

with the use of only one single test structure and without any fitting processes [9] . The test structure is a UMZI formed by two (not necessarily identical) 2×2 couplers. By simply extracting the extinction ratios of the UMZI output transmission spectra, it is possible to calculate the coupling ratios of each coupler and the waveguide loss. This measurement method is insensitive to the fiber-waveguide coupling losses; thus, it can achieve precise results without the need for fiber-waveguide coupling repeatability.

In this appendix, we explain the theory behind the characterization method and derive formulas that describe the responses of a general unbalanced MZI. In the second section, two different test cases are demonstrated to illustrate the characterization method in practice.

2.1 Theory

Our test structure comprises an unbalanced MZI. The UMZI is formed by two 2×2 couplers connected to each other by two waveguide arms with different path lengths, as shown in *Figure 4.2(a)*. Said 2×2 couplers can but do not have to be identical. Typical optical spectra of transmissions are shown in *Figure 4.2(b)*. At a wavelength window of interest (1550±1.5 nm in this example), extinction ratios (ERs) are defined as the ratio between the neighboring maxima and minima of the optical spectra. The goal of this section is to establish explicit formulae for the waveguide propagation loss constant and the coupling coefficients of the two 2×2 couplers as a function of said ERs.

Let the power coupling and power transmission coefficients of a waveguide directional coupler be denoted by $\kappa^2 = \sin^2\theta_i$ and $\tau^2 = \cos^2\theta_i$ respectively (where $0 \le \theta_i \le \frac{\pi}{2}$). Then, the scattering matrix of the coupler can be written as $C_i = \begin{bmatrix} \cos\theta_i & -j\sin\theta_i \\ -j\sin\theta_i & \cos\theta_i \end{bmatrix}$.

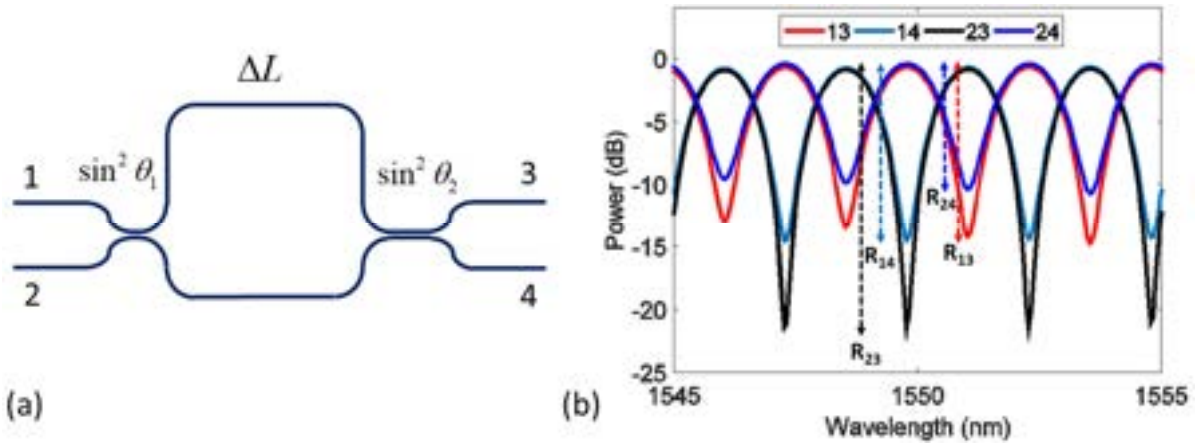

Figure A2.1 (a) Schematic of an UMZI. b) Optical spectra of transmissions through a UMZI structure. The spectra were simulated with the coupling ratios of the two couplers being 0.3 and 0.4, path length difference ΔL *= 500 μm and a propagation loss 10 dB/cm. Extinction ratios are denoted by* R_{13}*,* R_{14}*,* R_{23} *and* R_{24}*.* ©IEEE 2016

The path length difference between the two arms is ΔL, thus the transfer matrix of the delay path in between the two couplers is $T_i = \begin{bmatrix} \exp(-j\phi - \alpha\Delta L) & 0 \\ 0 & 1 \end{bmatrix}$ where $\phi = \frac{2\pi n_{eff}(\lambda)}{\lambda}\Delta L$ expresses the accumulated phase shift difference between the two arms and α (cm^{-1}) is the field propagation loss constant of the waveguide. Notice that the power propagation loss of the waveguide in dB/cm can be converted from this constant by the formula $\alpha_{dB} = \frac{20}{\ln 10}\alpha$ (dB/cm).

We will first establish the analytical expression for the transmission powers through the UMZI using these parameters. The transfer matrix of the whole MZI structure is given by $S = C_1 T C_2 = \begin{bmatrix} S_{11} & S_{12} \\ S_{21} & S_{22} \end{bmatrix}$ where

$$S_{11} = \exp(-j\phi - \alpha\Delta L)\cos\theta_1\cos\theta_2 - \sin\theta_1\sin\theta_2 \qquad (1.a)$$

$$S_{12} = -j\sin\theta_1\cos\theta_2 - j\exp(-j\phi - \alpha\Delta L)\cos\theta_1\sin\theta_2 \qquad (1.b)$$

$$S_{21} = -j\exp(-j\phi - \alpha\Delta L)\sin\theta_1\cos\theta_2 - j\cos\theta_1\sin\theta_2 \qquad (1.c)$$

$$S_{22} = \cos\theta_1 \cos\theta_2 - \exp(-j\phi - \alpha\Delta L)\sin\theta_1 \sin\theta_2 \qquad (1.d)$$

Now we can calculate the coupling powers between ports. For instance, the power coupling from port 1 to port 3 of the UMZI is given by $P_{13} = |S_{11}^{\ 2}|$. The full equation is

$$P_{13} = \exp(-2\alpha\Delta L)\cos^2\theta_1 \cos^2\theta_2 + \sin^2\theta_1 \sin^2\theta_2 + \\ -2\cos\phi \exp(-\alpha\Delta L)\cos\theta_1 \cos\theta_2 \sin\theta_1 \sin\theta_2 \qquad (2)$$

Similarly, one can obtain the equations for the coupling powers between all other ports. Due to space considerations we will follow the full notation for P_{13} only, but all other power couplings (P_{14}, P_{23}, P_{24}) are straightforward to derive.

In the scope of this paper, we only consider the regime where the path length difference ΔL is at least two orders of magnitude larger than the wavelength λ. The wavelength period for $\phi = \frac{2\pi n_{eff}(\lambda)}{\lambda}\Delta L$ to complete a full 2π cycle is $\Delta\lambda = \frac{\lambda^2}{\Delta L n_g(\lambda)}$ where $n_g(\lambda) = n_{eff}(\lambda) - \lambda\frac{dn_{eff}(\lambda)}{d\lambda}$. In the considered regime, the wavelength period $\Delta\lambda$ is small enough to allow us to assume that all the terms except $\cos\phi$ in eq. (1) and eq. (2) are approximately constant within the wavelength interval $[\lambda - \Delta\lambda/2,\ \lambda + \Delta\lambda/2]$. Certainly, the longer ΔL is, the more valid the assumption becomes and the more accurate the measurement is.

With that assumption, we will next establish the equations for the extrema of the coupling power within the wavelength interval $[\lambda - \Delta\lambda/2,\ \lambda + \Delta\lambda/2]$. In eq. 2, it is clear that the coupling power reaches the extrema when $\cos\phi$ reaches its extrema.

$$P_{13}^{\max,\min} = \left(\exp(-\alpha\Delta L)\cos\theta_1 \cos\theta_2 \pm \sin\theta_1 \sin\theta_2\right)^2 \qquad (3)$$

From the equation above and defining the ER to be the ratio between the maxima and minima, we have the following equation for the ER of the power transmission spectrum from port 1 to 3:

$$R_{13} = \frac{P_{13}^{\max}}{P_{13}^{\min}} = \left(\frac{\exp(-\alpha \Delta L) + \tan\theta_1 \tan\theta_2}{\exp(-\alpha \Delta L) - \tan\theta_1 \tan\theta_2} \right)^2 \qquad (4)$$

These equations relate the ERs, which we can directly measure experimentally, with the propagation loss $\exp(-\alpha \Delta L)$ and the characteristic parameters $\tan\theta_1$ and $\tan\theta_2$ of the two couplers, which are what we want to calculate. In the next step, we will derive the values of α, θ_1 and θ_2 from the directly measurable values of R_{13}, R_{14}, R_{23} and R_{24}.

From the full equation set (derived R_{13}, R_{14}, R_{23} and R_{24}), we obtain the following equations:

$$\frac{\exp(-\alpha \Delta L) + \tan\theta_1 \tan\theta_2}{\exp(-\alpha \Delta L) - \tan\theta_1 \tan\theta_2} = \pm\sqrt{R_{13}} \qquad (5.a)$$

$$\frac{\exp(-\alpha \Delta L)\tan\theta_1 + \tan\theta_2}{\exp(-\alpha \Delta L)\tan\theta_1 - \tan\theta_2} = \pm\sqrt{R_{14}} \qquad (5.b)$$

$$\frac{\tan\theta_1 + \exp(-\alpha \Delta L)\tan\theta_2}{\tan\theta_1 - \exp(-\alpha \Delta L)\tan\theta_2} = \pm\sqrt{R_{23}} \qquad (5.c)$$

$$\frac{1 + \exp(-\alpha \Delta L)\tan\theta_1 \tan\theta_2}{1 - \exp(-\alpha \Delta L)\tan\theta_1 \tan\theta_2} = \pm\sqrt{R_{24}} \qquad (5.d)$$

Based on the pair (5.a, 5.d), we can solve for $\exp(-\alpha \Delta L)$ and $\tan\theta_1 \tan\theta_2$.

$$\exp(-2\alpha \Delta L) = \frac{\sqrt{R_{13}} + (-1)^l}{\sqrt{R_{13}} - (-1)^l} \cdot \frac{\sqrt{R_{24}} + (-1)^m}{\sqrt{R_{24}} - (-1)^m} \qquad (6.a)$$

$$\tan\theta_1 \tan\theta_2 = \frac{\sqrt{R_{13}} - (-1)^l}{\sqrt{R_{13}} + (-1)^l} \cdot \frac{\sqrt{R_{24}} + (-1)^m}{\sqrt{R_{24}} - (-1)^m} \qquad (6.b)$$

Similarly, we have the following solutions for $\exp(-\alpha \Delta L)$ and $\tan\theta_2 / \tan\theta_1$ based on the pair (5.b, 5.c):

$$\exp(-2\alpha \Delta L) = \frac{\sqrt{R_{14}} + (-1)^n}{\sqrt{R_{14}} - (-1)^n} \cdot \frac{\sqrt{R_{23}} + (-1)^p}{\sqrt{R_{23}} - (-1)^p} \qquad (6.c)$$

$$\frac{\tan\theta_2}{\tan\theta_1}=\frac{\sqrt{R_{14}}-(-1)^n}{\sqrt{R_{14}}+(-1)^n}\cdot\frac{\sqrt{R_{23}}+(-1)^p}{\sqrt{R_{23}}-(-1)^p} \qquad (6.d)$$

Here, the parameters *l, m, n, p* can be either 0 or 1. However, this set of parameters are constrained by the condition that (6.a) and (6.c) must be equivalent and the value of $\exp(-\alpha\Delta L)$ must be smaller than 1, as written in (7) below.

$$\frac{\sqrt{R_{13}}+(-1)^l}{\sqrt{R_{13}}-(-1)^l}\cdot\frac{\sqrt{R_{24}}+(-1)^m}{\sqrt{R_{24}}-(-1)^m}=\frac{\sqrt{R_{14}}+(-1)^n}{\sqrt{R_{14}}-(-1)^n}\cdot\frac{\sqrt{R_{23}}+(-1)^p}{\sqrt{R_{23}}-(-1)^p}<1 \quad (7)$$

This condition will eliminate all the unsatisfying values of *l, m, n, p* and leave out only one relevant set. Finally, based on equations (6) with the set of *l, m, n, p* determined, the parameters α, κ_1 and κ_2 can be explicitly expressed:

$$\begin{aligned}\alpha&=-\frac{1}{2\Delta L}\ln\left(\frac{\sqrt{R_{14}}+(-1)^n}{\sqrt{R_{14}}-(-1)^n}\frac{\sqrt{R_{23}}+(-1)^p}{\sqrt{R_{23}}-(-1)^p}\right)\\&=-\frac{1}{2\Delta L}\ln\left(\frac{\sqrt{R_{13}}+(-1)^l}{\sqrt{R_{13}}-(-1)^l}\frac{\sqrt{R_{24}}+(-1)^m}{\sqrt{R_{24}}-(-1)^m}\right)\end{aligned} \qquad (8.a)$$

$$\kappa_1^2=\sin^2\theta_1=\frac{\left(\frac{\sqrt{R_{13}}-(-1)^l}{\sqrt{R_{13}}+(-1)^l}\frac{\sqrt{R_{24}}+(-1)^m}{\sqrt{R_{24}}-(-1)^m}\frac{\sqrt{R_{14}}-(-1)^n}{\sqrt{R_{14}}+(-1)^n}\frac{\sqrt{R_{23}}+(-1)^p}{\sqrt{R_{23}}-(-1)^p}\right)^{1/2}}{1+\left(\frac{\sqrt{R_{13}}-(-1)^l}{\sqrt{R_{13}}+(-1)^l}\frac{\sqrt{R_{24}}+(-1)^m}{\sqrt{R_{24}}-(-1)^m}\frac{\sqrt{R_{14}}-(-1)^n}{\sqrt{R_{14}}+(-1)^n}\frac{\sqrt{R_{23}}+(-1)^p}{\sqrt{R_{23}}-(-1)^p}\right)^{1/2}} \quad (8.b)$$

$$\kappa_2^2=\sin^2\theta_2=\frac{\left(\frac{\sqrt{R_{13}}-(-1)^l}{\sqrt{R_{13}}+(-1)^l}\frac{\sqrt{R_{24}}+(-1)^m}{\sqrt{R_{24}}-(-1)^m}\frac{\sqrt{R_{14}}+(-1)^n}{\sqrt{R_{14}}-(-1)^n}\frac{\sqrt{R_{23}}-(-1)^p}{\sqrt{R_{23}}+(-1)^p}\right)^{1/2}}{1+\left(\frac{\sqrt{R_{13}}-(-1)^l}{\sqrt{R_{13}}+(-1)^l}\frac{\sqrt{R_{24}}+(-1)^m}{\sqrt{R_{24}}-(-1)^m}\frac{\sqrt{R_{14}}+(-1)^n}{\sqrt{R_{14}}-(-1)^n}\frac{\sqrt{R_{23}}-(-1)^p}{\sqrt{R_{23}}+(-1)^p}\right)^{1/2}} \quad (8.c)$$

In a particular case where the two couplers are identical, the equations become much simpler. Indeed, with $\theta_1=\theta_2=\theta$ and $\exp(-\alpha\Delta L)<1$ condition, equations (6.c) and (6.d) can hold true if and only if $R_{14}=R_{23}$ and $n=p=1$. Therefore, equations (8) become:

$$\alpha=-\frac{1}{\Delta L}\ln\left(\frac{\sqrt{R_{14}}-1}{\sqrt{R_{14}}+1}\right)=-\frac{1}{2\Delta L}\ln\left(\frac{\sqrt{R_{13}}+(-1)^l}{\sqrt{R_{13}}-(-1)^l}\cdot\frac{\sqrt{R_{24}}+(-1)^m}{\sqrt{R_{24}}-(-1)^m}\right) \quad (9.a)$$

$$\kappa^2=\sin^2\theta=\frac{\left(\frac{\sqrt{R_{13}}-(-1)^l\sqrt{R_{24}}+(-1)^m}{\sqrt{R_{13}}+(-1)^l\sqrt{R_{24}}-(-1)^m}\right)^{1/2}}{1+\left(\frac{\sqrt{R_{13}}-(-1)^l\sqrt{R_{24}}+(-1)^m}{\sqrt{R_{13}}+(-1)^l\sqrt{R_{24}}-(-1)^m}\right)^{1/2}} \quad (9.b)$$

In short, we have shown that it is possible to extract the values of the propagation loss constant α of the waveguide as well as the power coupling coefficients of the two couplers (κ_1 and κ_2) based on the four directly measurable extinction ratios R_{13}, R_{14}, R_{23} and R_{24}.

2.2 Experimental demonstrations

In this section, we describe the experiment implementation to carry out our measurement method and show several measured results based on the theory developed above.

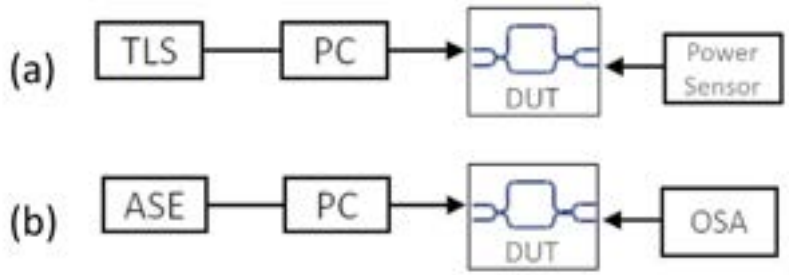

Figure A2.2 a) The measurement setup using a tunable laser source (TLS), a single mode fiber polarization controller (PC) and a power sensor. b) An alternative configuration using a broadband source (e.g. ASE) with an optical spectrum analyzer (OSA). ©IEEE 2016

As shown in *Figure A2.2*, two experimental configurations can be used to record the optical spectra of transmissions through the UMZI structure. In our work, we used the configuration shown in *Figure A2.2(a)* with the Agilent tunable laser source (81640A) and power sensor (81635A) which can resolve a 0.1 pm step size in the optical spectrum. We will demonstrate the proposed method with the two following test cases:

a) A UMZI on Si_3N_4 waveguides with a 62.1 cm path length difference and two different directional couplers with unknown coupling ratios (illustrated in *Figure A2.3(a)*): We will use the general equation set (8) to calculate the waveguide propagation loss as well as the coupling ratios of the two couplers.

b) A UMZI on Si waveguides with 150 μm path length difference and two identical directional couplers (shown in *Figure A2.3(b)*):): We will characterize the relation between the coupling ratio and the coupler length by applying simplified equation set (9) to multiple UMZIs with varying directional coupler lengths.

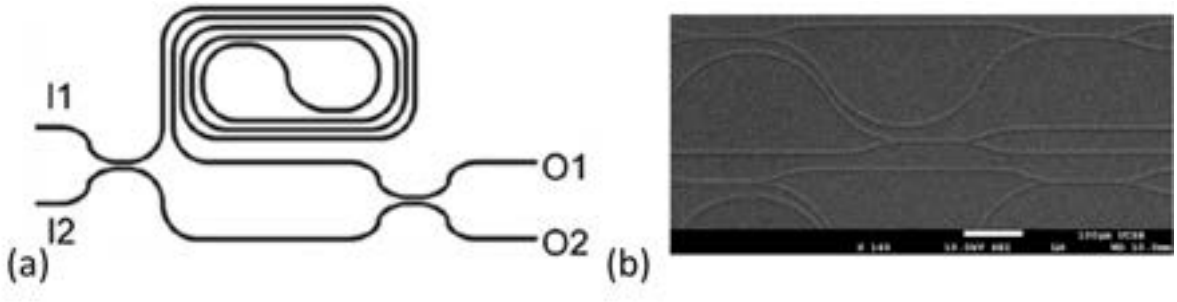

Figure A2.3 (a) Schematic of the Si_3N_4 waveguide UMZI with 62.1 cm length difference (b) An SEM image of a set of silicon waveguide UMZI structures for coupling ratio characterization. ©IEEE 2016

2.2.1 *UMZI formed by two different directional couplers*

This is the most general case where all of the criteria are unknown and independent. The transmitted optical spectra around 1550 nm wavelength are shown in *Figure A2.4*. Values of the extinction ratios are extracted and tabulated in *Table A2.1*. The extinction ratios are converted to linear scale before we apply condition (7) to find out the relevant set of (*l, m, n, p*), which turns out to be (1, 1, 1, 1). With all of these parameters determined, by using eq. (8), the propagation loss constant is calculated to be $\alpha = 0.0283 \pm 0.003\ \mathrm{cm}^{-1}$. This translates to a

waveguide propagation loss rate of $\alpha_{dB} = 0.2458 \pm 0.0026$ dB/cm. The coupling ratios of the first and the second couplers are $\kappa_1 = 0.608 \pm 0.012$ and $\kappa_2 = 0.801 \pm 0.008$ respectively.

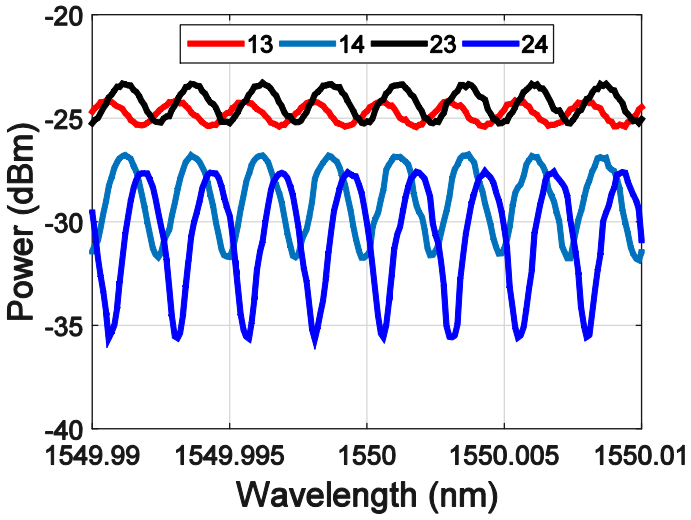

Figure A2.4 Optical spectra of the transmissions through the UMZI fabricated on Si3N4 waveguide platform. The path length difference is 62.1 cm. The peaks and valleys do not line-up due to the limited ±1 pm of swept wavelength repeatability. ©IEEE 2016

Table A2.1 Extinction ratios and values of parameters l, m, n, p

R_{13} *(dB)*	R_{14} *(dB)*	R_{23} *(dB)*	R_{24} *(dB)*	l	m	n	p
1.20	4.93	1.86	8.00	1	1	1	1

The propagation loss result by our method is in good agreement with the other method using optical frequency domain reflectometry (OBR 4400), which measured the loss to be 0.24 dB/cm.

2.2.2 UMZI formed by two identical directional couplers

In this particular test, we focus only on characterization of the coupling coefficients of the couplers. An array of the UMZI with varying coupler lengths (from 10 μm to 160 μm) are needed to characterize the coupler length dependence of the coupling coefficient. Therefore,

a relatively short path length difference of 150 μm is made to save the space. This gives us a negligible propagation loss.

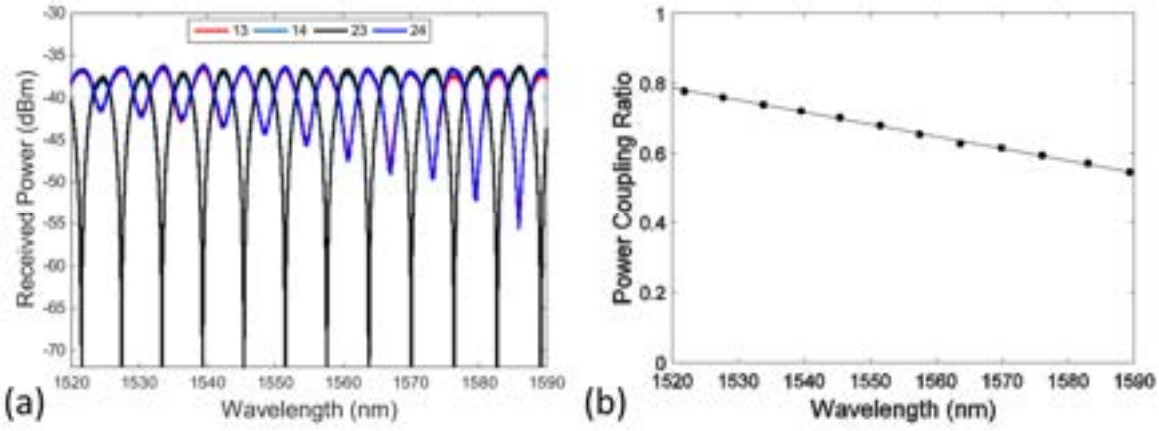

Figure A2.5 Optical spectra of the transmissions through the UMZI fabricated on Si3N4 waveguide platform. ©IEEE 2016

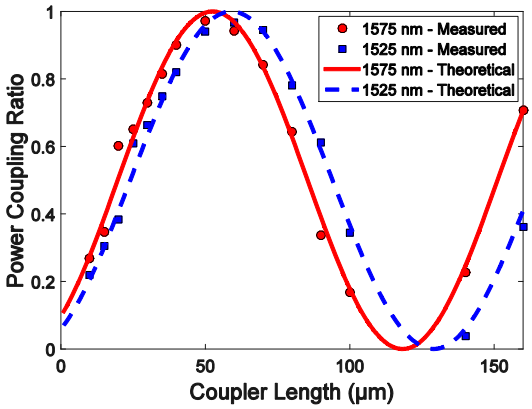

Figure A2.6 The coupling ratio versus coupler length of the Si directional couplers at two wavelengths 1525 nm and 1575 nm. The measured data are plotted together with theoretical fitting curves. ©IEEE 2016

The transmission spectra of a UMZI with a coupler length of 80 μm is shown in *Figure A2.5(a)*. Using the simplified equations (9), we extracted the coupling coefficient over the broad wavelength range as shown in *Figure A2.5(b)*. Repeating the process for other UMZIs with different coupler lengths, we can obtain the coupler length dependency of the coupling

coefficients as shown in *Figure A2.6*. The excellent agreement between the experimental results with theoretical calculation shows that this method is highly accurate.

2.3 Summary

We have analyzed the responses of unbalanced MZI structures formed by two 2×2 couplers. Based on this analysis, we have proposed and demonstrated a new method to simultaneously characterize the waveguide and the couplers using only a single test structure. The method is inherently robust to variations that can occur during sample preparation and testing, such as coupling loss, waveguide facet quality, and fiber-to-chip alignment. Precise results can be achieved in the presence of coupling variations.

References

[1] D. B. Keck and A. R. Tynes, "Spectral Response of Low-Loss Optical Waveguides," *Appl. Opt.*, 2008.

[2] S. Taebi, M. Khorasaninejad, and S. S. Saini, "Modified Fabry-Perot interferometric method for waveguide loss measurement," *Appl. Opt.*, 2008.

[3] P. Dumon *et al.*, "Low-loss SOI photonic wires and ring resonators fabricated with deep UV lithography," *IEEE Photonics Technol. Lett.*, 2004.

[4] T. R. Bourk, M. M. Z. Kharadly, and J. E. Lewis, "Measurement of waveguide attenuation by resonance methods," *Electron. Lett.*, vol. 4, no. 13, p. 267, 1968.

[5] R. Adar, Y. Shani, C. H. Henry, R. C. Kistler, G. E. Blonder, and N. A. Olsson, "Measurement of very low - loss silica on silicon waveguides with a ring resonator Measurement resonator of very low-loss silica on silicon waveguides with a ring," vol. 444, no. 1991, pp. 3–5, 2011.

[6] M. Moresco *et al.*, "Method for characterization of Si waveguide propagation loss.," *Opt. Express*, vol. 21, no. 5, pp. 5391–400, 2013.

[7] A. M. Gutierrez, A. Brimont, M. Aamer, and P. Sanchis, "Method for measuring waveguide propagation losses by means of a Mach-Zehnder Interferometer structure," *Opt. Commun.*, 2012.

[8] W. Bogaerts *et al.*, "Silicon microring resonators," *Laser Photonics Rev.*, vol. 6, no. 1, pp. 47–73, 2012.

[9] M. Tran, T. Komljenovic, J. Hulme, M. Davenport, and J. Bowers, "A Robust Method for Characterization of Optical Waveguides and Couplers," *IEEE Photonics Technol. Lett.*, vol. PP, no. 99, pp. 1–1, 2016.

Appendix 3. Si/III-V Device Fabrication Process

The laser fabrication is depicted in *Figure A2.6* . It consists of silicon patterning and etching, III-V bonding and processing, followed by metal deposition for the contacts and heaters. The entire process is performed using a 248 nm DUV stepper for lithography, except for the gratings, which are defined using electron beam lithography due to their small feature size (238nm period). However, state of the art lithography systems in silicon foundries can resolve these features. The entire fabrication takes place at a wafer scale (4" SOI wafer), which demonstrates the potential scalability of the process.

Due to the multiple silicon etches with different etch depths, a SiO_2 hard-mask is used to define the waveguides. The etches are then carried out with the shallowest etch (56 nm) first, followed by the intermediate (231 nm) and full etch (500 nm) with photoresist masking in between each step. Since the hard-mask was used to define the waveguides during the entire process, it ensures that the transitions between waveguides with different etch depths are self-aligned and not subject to lithographic misalignment in the stepper. The ultralow loss Si waveguide areas containing the gratings and rings are clad with SiO_2 to protect them from the ensuing III-V bonding and processing and preserve the low waveguide loss.

The III-V die is bonded using an O_2 plasma activated direct bonding procedure, and the InP substrate is removed using a combination of lapping and wet etching. The laser mesas are etched using a series of $CH_4/H_2/Ar$ dry etches as well as wet etches containing HCl or H_3PO_4. After the III-V processing is complete, SiO_2 is sputtered, and vias are opened to expose the n- and p-contacts. The last part of the fabrication is deposition of the various metals for n- (Pd/Ge/Pd/Au/Ti) and p-contacts (Pd/Ti/Pd/Au), heaters (Pt), and probe pads (Au/Ti). The

current channels are formed using proton implantation. Further details on the fabrication of heterogeneous silicon/III-V lasers can be found in [1].

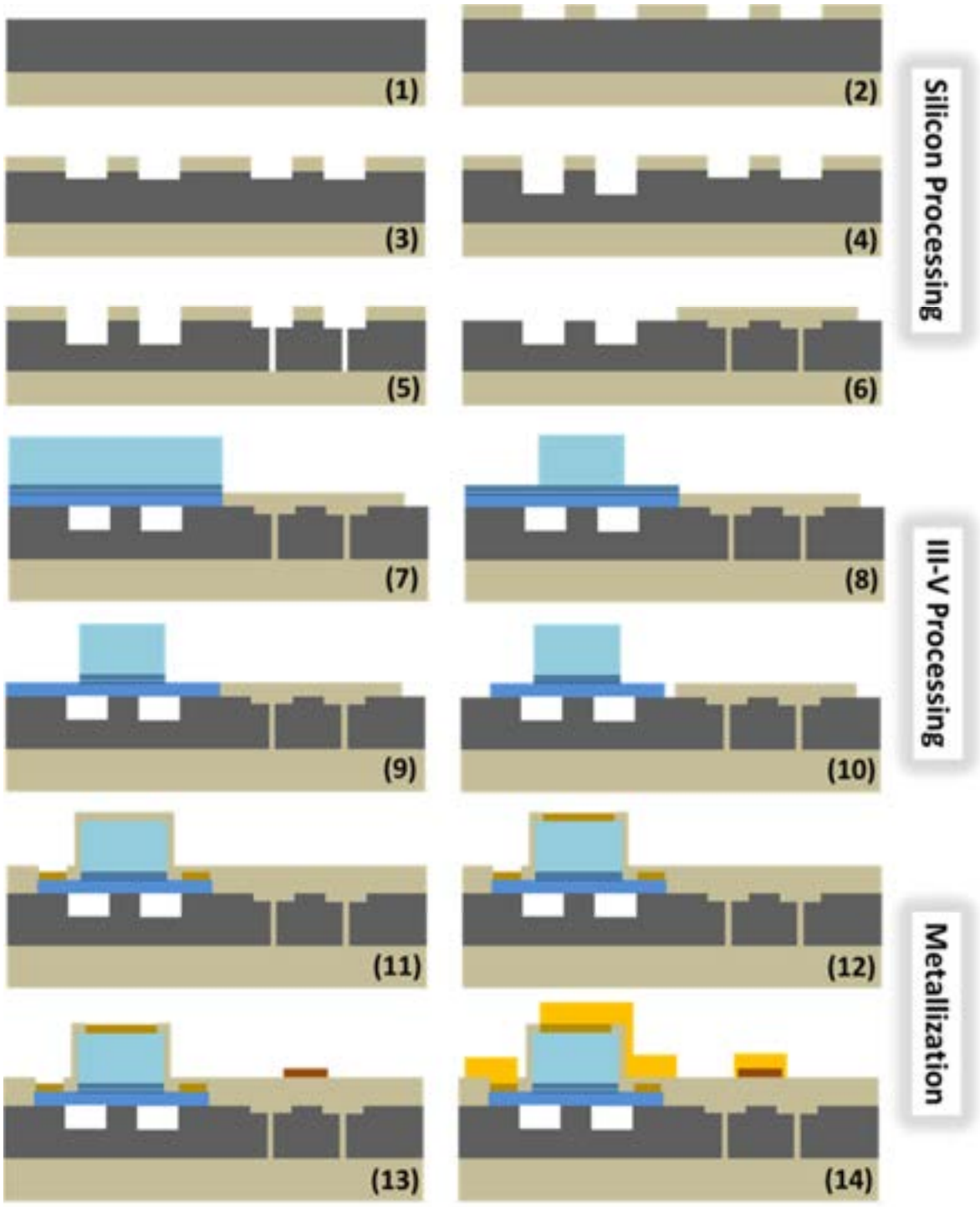

Figure A3.1 Modified fabrication procedure for the Si/III-V lasers. The process begins with silicon processing (1-6) with patterning of waveguides and gratings. The III-V epi is bonded (7), followed by patterning of the mesa (8-10), etching of the p-InP, MQW, and n-InP layers. The mesas are passivated, followed by metallization of the n-contact (11), p-contacts (12), heaters (13) and probe metal (14).

References

[1] M. L. Davenport, "Heterogeneous Silicon III-V Mode-Locked Lasers," UCSB, 2017.